Chem Soc Rev

ROYAL SOCIETY OF CHEMISTRY

REVIEW ARTICLE

View Article Online
View Journal | View Issue

Check for updates

Cite this: *Chem. Soc. Rev.*, 2025, **54**, 11266

Received 30th June 2025

DOI: 10.1039/d5cs00748h

rsc.li/chem-soc-rev

Emerging applications of stimulated Raman scattering microscopy for medicinal chemistry and drug discovery

Henry J. Braddick, †[a] William J. Tipping, †[b] Emma K. Grant,[c] Nicholas C. O. Tomkinson, *[a] Karen Faulds *[b] and Duncan Graham *[b]

This review article provides a summary of the progress that has been made in the field of stimulated Raman scattering (SRS) microscopy with direct relevance to drug discovery and medicinal chemistry. SRS microscopy is emerging as a powerful technique to visualise drugs and bioactive small molecules in cellular and tissue samples, and recent technological advances coupled with the commercial availability of SRS imaging systems means it has much to offer within preclinical drug evaluation. Attrition rates throughout all stages of the drug discovery pipeline are high and innovative analytical tools have the potential to enhance preclinical evaluation studies. SRS microscopy provides significant capability in pharmaceutical development by providing a label-free and minimally invasive method to determine intracellular drug localisation and metabolism, together with high-resolution images of drug–cell interactions and the ability to visualise any phenotypic cellular response. We summarise the technical developments in hyperspectral SRS microscopy, together with detailing recent applications of machine learning and chemometrics that can be used to extricate underlying biochemical features from imaging data. We outline the developments and applications of SRS imaging for the label-free visualisation of drugs and bioactive small molecules in cellular models, together with an overview of the technique for identifying features of metabolism with relevance to cancer and antimicrobial therapy. Lastly, we cover the application of SRS imaging for transdermal drug delivery and development, before covering pharmaceutical formulation analysis.

1. Introduction

1.1. The need for innovative technologies in drug discovery

Reducing the rate of drug attrition remains a key goal in the pharmaceutical industry.[1] For example, in the development of oncology drugs, it has been reported that this rate is persistently greater than 95%,[2] imposing significant financial implications on the provision of new medicines and highlighting a primary challenge in delivering therapeutics for clinical use.[3] Key reasons which have been attributed to the clinical failure of drug candidates include, the lack of clinical efficacy, toxicological burden and poor drug–like properties (*e.g.* absorption, bioavailability, transportation and excretion).[4] The parity between the number of molecules which have positive indications within pre-clinical drug development, and the number which subsequently fail in clinical trials, also serves to highlight the need for innovative methods to assess drug developability at an early stage.

The paucity of reliable predictive preclinical models is considered to be a key reason for the high drug attrition rates in oncology.[5] The generation of model systems which can better recapitulate the natural biological environment to assess the patterns of drug diffusion, cell–cell signalling and drug activity in complex tissue architecture have been examined.[6] For example, the development of three-dimensional (3D) cell cultures and organoid models can be a valuable approach for investigating drug targeting because the complex macrostructure of the tissue-like architecture is more reflective of the *in vivo* setting. As such, 3D cell culture can better predict the *in vivo* activity of a drug, with the potential to reduce failure in the later, more expensive stages of development.[7] Underscoring the development of preclinical models is the requirement for analytical methods to monitor drug activity *in situ*.[8] In this regard, image-based profiling is an emerging strategy, by which cellular

---

[a] *Department of Pure and Applied Chemistry, University of Strathclyde, Glasgow, G1 1XL, UK. E-mail: nicholas.tomkinson@strath.ac.uk*

[b] *Centre for Molecular Nanometrology, Department of Pure and Applied Chemistry, Technology and Innovation Centre, University of Strathclyde, Glasgow, G1 1RD, UK. E-mail: karen.faulds@strath.ac.uk, duncan.graham@strath.ac.uk*

[c] *GlaxoSmithKline Medicines Research Centre, Gunnels Wood Road, Stevenage, SG1 2NY, UK*

† Equal contribution.

features can be used to represent the effect of a given treatment within a population of cells.[9] Cell painting is a relevant example, whereby multicolour fluorescent labelling of cellular components, such as the nucleus, mitochondria and

Henry J. Braddick

Henry Braddick received his MChem in Chemistry from the University of Manchester in 2020. He then obtained his PhD in 2024 under the supervision of Prof. Nicholas Tomkinson at the University of Strathclyde. His project focused on the development of intracellular sensors for detection by spontaneous Raman spectroscopy and stimulated Raman scattering.

William J. Tipping

William Tipping obtained his PhD in Chemistry from the University of Edinburgh in 2017 under the guidance of Prof Alison Hulme and Prof Valerie Brunton. After a brief postdoctoral position in the same group, he joined the University of Strathclyde in 2019 to work with Prof Duncan Graham and Prof Karen Faulds. His research interests include the development of imaging probes for Raman microscopy, and the development of stimulated Raman scattering microscopy for biomedical imaging applications.

Emma K. Grant

Emma Grant is a Principal Scientist at GSK, based in the Chemical Biology department. She is focused on tool development and characterisation and has significant experience in covalent drug discovery. She holds a PhD in Chemical Biology from the University of Strathclyde, under the supervision of Professor Nicholas Tomkinson and Jacob Bush (GSK).

Nicholas C. O. Tomkinson

Nick Tomkinson studied Chemistry at The University of Sheffield and received his BSc in 1992 and his PhD in 1995 under the supervision of Dr D. Neville Jones and Professor Jim Anderson. Postdoctoral studies with Dr. Tim Willson at GlaxoSmithKline, Research Triangle Park, North Carolina (1996–1998) followed. Nick was appointed to the staff at Cardiff University in 1999 and was an EPSRC Advanced Research Fellowship (2004–2009). He moved to his current position at the University of Strathclyde in June 2011 where he is Head of Chemical Biology and Medicinal Chemistry.

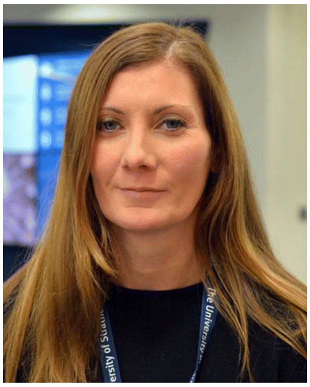

Karen Faulds

Karen Faulds is an expert in analytical spectroscopy, in particular Raman spectroscopy. She has developed several new assays for use in the life sciences based on Raman spectroscopy. She holds the post of Distinguished Professor at the University of Strathclyde and is the Head of Bionanotechnology and Analytical Chemistry. She holds a PhD from the University of Strathclyde and is an elected member of the Royal Society of Chemistry's Analytical Community Council.

Duncan Graham

Duncan Graham is an expert in bioanalytical measurements with interests in Raman and advanced Raman spectroscopy techniques to provide new capability to life scientists. He graduated with a PhD in bioorganic chemistry from the University of Edinburgh and is an Associate Principal and Dean of the Faculty of Science at the University of Strathclyde. He is the current Editor in Chief of Chemical Society Reviews and was previously chair of the publishing board and an appointed trustee for the Royal Society of Chemistry.

endoplasmic reticulum, is used to visualise the drug-induced effects on different and varied cellular features.[10] As a result, an image-based profile can be generated for individual drug treatments in a high-throughput manner. The resulting multidimensional profile of biological images can be mined for relevant patterns to reveal unexpected biological activity, which can prove advantageous in preclinical drug development. Whilst fluorescence microscopy is the frontrunner in high-throughput image-based screening,[11] advances in Raman microscopy, and in particular stimulated Raman scattering (SRS), hold significant potential in this area.

This review is focussed on highlighting the development and applications of SRS microscopy in the preclinical stages of the drug development process. It begins with a focus on the technique describing advances in SRS microscopy that have been applied to cellular imaging. It highlights recent progress in hyperspectral SRS imaging and the application of machine learning techniques for data processing, together with the implementation of super-resolution SRS microscopy. These advances are contextualised through case studies that are pertinent to drug discovery. The application of SRS microscopy in the visualisation of drug uptake and distribution in biological models, together with an assessment of drug metabolism is also described, with a focus on cancer and antimicrobial resistance. We also highlight the potential of SRS microscopy in skin imaging and dermal drug delivery, together with its use in visualising pharmaceutical dosage forms and formulation analysis. Overall, the emerging breadth and unique insights provided by SRS microscopy through image-based analysis across multiple facets of the drug discovery and development process is presented.

2. Stimulated Raman scattering microscopy

2.1. Overview of stimulated Raman scattering microscopy

Vibrational spectroscopy techniques are uniquely positioned for biological imaging applications because of their ability to assess molecular composition in a non-destructive manner. In general, vibrational spectroscopy refers to infrared (IR) spectroscopy and Raman scattering. SRS microscopy is an advanced form of Raman scattering which employs dual laser irradiation. In comparison to spontaneous Raman scattering, which uses a single monochromatic laser source to determine inelastic scattering from a sample, SRS uses ultrashort laser pulses from a pump (ω_p) and Stokes (ω_S) beam. By matching the frequency difference ($\Delta\omega = \omega_\text{p} - \omega_\text{S}$) between the two laser beams to a vibrational energy level within the sample (Ω), coherent excitation of the molecular vibration results (Fig. 1A). As such, the molecules are transferred from the ground vibrational state through a virtual state to a vibrationally excited state. This process results in a stimulated vibrational excitation of the molecular transition through the dual action of the two laser frequencies, which is significantly enhanced compared to spontaneous Raman scattering and is known as coherent Raman scattering. During coherent Raman scattering, a pump photon is destroyed (stimulated Raman loss, SRL) and a Stokes photon (of lower energy than the pump photon) is created (stimulated Raman gain, SRG). Experimentally, SRL is detected as an intensity reduction in the pump laser beam, whilst SRG is detected as an intensity gain in the Stokes laser beam (Fig. 1B). For SRS to occur, the pump and Stokes beams are spatially and temporally overlapped prior to focussing onto the sample using a microscope objective. In most SRS systems, the SRL and SRG signals are collected by a condenser lens, before passing through a filter, usually to remove the Stokes beam wavelength, as this is usually a fixed wavelength source. The SRL signal is then detected in the pump beam laser intensity using a photodiode.[12]

The SRL (or SRG signal) is represented as an intensity change in the incident laser, which is typically small ($\Delta I_\text{P}/I_\text{P}$ or $\Delta I_\text{s}/I_\text{s}$, $\approx 10^{-3}$–10^{-7}) and, therefore can be lost in the laser noise.[13] In order to detect the SRS signal, a modulation transfer scheme has proven most effective. In most cases, the Stokes laser beam is modulated at high frequency by an electro-optic modulator (EOM) or acousto-optic modulator (AOM). Therefore, the SRL/SRG signals, which are buried in the laser noise, occur at the same frequency as the modulation frequency of the Stokes laser beam. Thus, the SRL (or SRG) signal can be

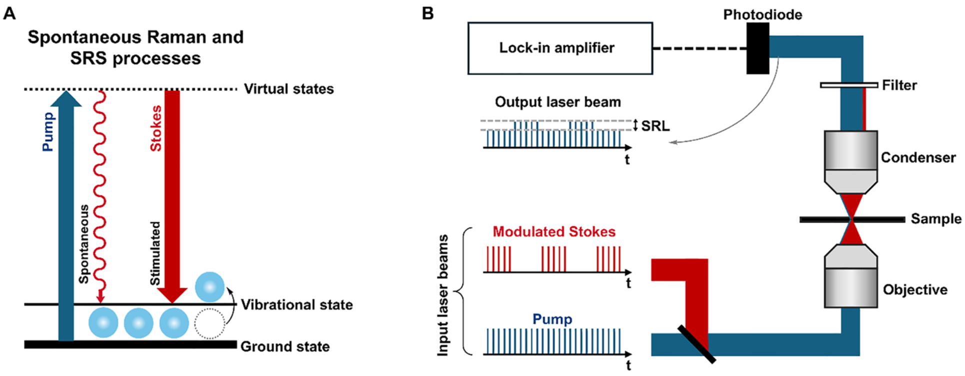

Fig. 1 Principles of biological SRS microscopy. (A) Energy level diagram for spontaneous Raman and SRS. SRS is a two-photon process requiring a spatially and temporally overlapped pump and Stokes beam. (B) Schematic diagram of an SRS microscope.

demodulated from the laser noise using a lock-in amplifier. It is noteworthy that SRS is termed a *nonlinear optical process*, which refers to the observation that upon interaction of an incident light source with a sample, a nonlinear amplitude response of the applied field is produced.

2.2. Advancements in SRS microscopy for bioimaging applications

Since the first report of SRS applied to biological imaging in 2008,[14] numerous advances have been realised for the successful deployment of the technique for spatial biology, microscopy and pharmaceutical applications. A summary of the major advances in the field of biological SRS microscopy are highlighted in Fig. 2A. A key advantage of SRS relative to spontaneous Raman scattering is that the technique is considerably faster, and has been shown to enable video-rate image acquisition in biological specimens (100 ns per pixel, 512 × 512 frame, 25 frames per second).[15] When performing SRS imaging on biological samples, it is useful to first consider the spontaneous Raman spectrum of cells. Fig. 2B presents the Raman spectrum acquired from a single HeLa cell. The Raman spectrum is comprised of three distinct regions: (i) fingerprint region (0–1800 cm^{-1}), (ii) bioorthogonal Raman window (1800–2800 cm^{-1}) and (iii) C–H region (2800–3100 cm^{-1}). The region >3100 cm^{-1} is dominated by O–H stretching vibrations (*e.g.* water at $\sim$3400 cm^{-1}) in aqueous samples. In each of the key regions of the cellular Raman spectrum, we have highlighted some of the main functional groups pertinent to biological Raman microscopy. The predominant species detected in the fingerprint region include phenylalanine ($\sim$1000 cm^{-1}), nucleic acids ($\sim$1340 cm^{-1}), lipids ($\sim$1440 cm^{-1}) and proteins (amide-I, $\sim$1655 cm^{-1}) amongst others. In the C–H region, biomolecules including, lipids, proteins and nucleic acids are especially prevalent. For in depth spectral assignments, a comprehensive overview is provided by Movasaghi *et al.*[16] In the bioorthogonal Raman window (1800–2800 cm^{-1}), a number of spectral bands are detected including those of alkyne (including polyynes), nitriles, C–D groups and

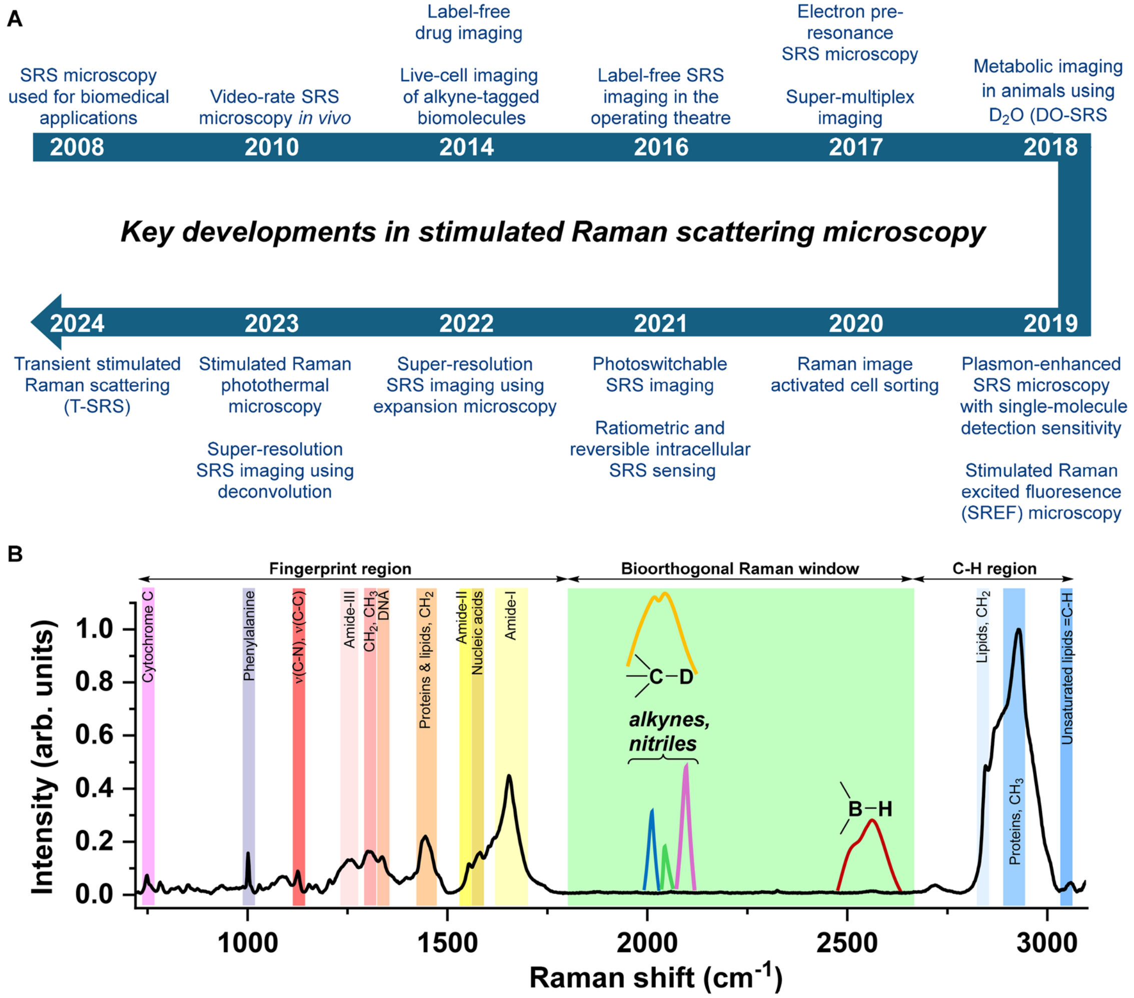

Fig. 2 Advances in biological SRS microscopy together with a cellular Raman spectrum. (A) A timeline of key events and discoveries in the history of stimulated Raman scattering. We have omitted the development of alkyne-tag Raman imaging by spontaneous Raman scattering in 2011 (see ref. 25 and 19) which paved the way for the development of equivalent imaging and sensing applications by SRS in 2014. (B) A cellular Raman spectrum of a single HeLa cell acquired using a 532 nm laser and a 60× objective lens (36 mW) for 10 s.

(metalla)carboranes (B–H) each of which can be used for bioorthogonal Raman labelling.

An important aspect of Raman imaging is that vibrations are narrower in wavelength than fluorescence emission bands which facilitates the detection of multiple targets, so called multiplex imaging. This is an attractive characteristic for labelling studies of biological samples, particularly through the incorporation of bioorthogonal Raman groups, which result in vibrational modes in the bioorthogonal Raman window (1800–2800 cm^{-1}).[17] Fluorescence microscopy faces an intrinsic colour barrier as a consequence of the broad ($\sim$1500 cm^{-1}) and featureless nature of spectra. The vibrational resonances of Raman probes are much narrower ($\sim$10 cm^{-1}) and as such, offer greater opportunities for multiplex detection (up to 26 spectral colours) in a simultaneous fashion.[18]

It is important to note that the Raman scattering cross section is unique to the compound of interest. A comprehensive assessment of Raman scattering cross section in the bioorthogonal Raman window has been achieved by determining the stretching intensity of a chemical bond relative to EdU (RIE).[19] As a general rule, alkynes have a higher Raman scattering cross section than nitrile and C–D bonds. Equally, the B–H stretch is relatively weak, although the formation of carborane clusters of multiple B–H stretching groups can help to offset this feature.[20] The use of isotopic editing – where an atom in the bond of interest is replaced by another natural isotope (*e.g.* ^{12}C and ^{13}C, and ^{1}H and ^{2}H) has been used to great effect to fine-tune the Raman shift of the resulting bond. This has also enabled the creation of multiplex palettes where the simultaneous detection of multiple different Raman labels is achieved at discrete spectral frequencies.[21] Additionally, molecular engineering of the alkyne bond through aryl end capping and the incorporation of electron donating or electron withdrawing groups has been shown to enable the fine tuning of the alkyne stretching frequency, enabling the creation of new spectral 'colours' for multiplex detection.[22]

SRS microscopy also produces high spatial resolution images when compared to spontaneous Raman scattering owing to the coherent nature of sample detection. Given that SRS is a multiphoton process, whereby the pump and Stokes lasers are tightly focussed onto the sample, the effective resolution of SRS imaging is generally higher. Under diffraction-limited optical conditions, SRS can achieve $\sim$400 nm lateral resolution, and $\sim$1–2 μm axial resolution using near infrared (NIR) light sources. As the spatial resolution is defined by the Abbe limit which is wavelength dependent,[23] an innovative method to improve the spatial resolution has been realised through the use of visible wavelength light for SRS imaging, with a lateral resolution down to 130 nm, for high resolution SRS imaging of cells (Fig. 3A).[24]

An additional advantage of NIR imaging is the improved tissue penetration depth in live samples when compared to ultraviolet (UV) and visible wavelength imaging.[26] In highly scattering tissue, the imaging depth using NIR light sources is around 100 μm, and in low-scattering tissue samples, volumetric SRS imaging can achieve a depth of 300–500 μm.[27] As such, there is a significant opportunity for spectral histopathology following surgical resection.[28] Several recent reports have developed tissue clearing methods to improve the penetration depth to >1 mm.[29] These methods preserve the tissue architecture for chemical analysis yet enable an insight to be obtained at depth. The biocompatibility of SRS imaging has enabled imaging applications in live cells (Fig. 3B) and microrganisms,[30,31] alongside whole organisms including *Caenorhabditis elegans* (Fig. 3C),[32] zebrafish (*Danio rerio)*,[33] and mice.[34]

As the SRL and SRG signals are detected at the pump and Stokes wavelengths respectively, SRS imaging is not greatly affected by fluorescence interference. This is a particular advantage compared to Raman scattering which can be overwhelmed by Stokes emission processes. Therefore, SRS imaging is compatible with multimodal imaging experiments, in particular, one- and two-photon fluorescence,[35] second harmonic generation,[36] along with photoacoustic[37] and photothermal imaging[38] modalities. Emergent, orthogonal approaches for chemical imaging such as SRS microscopy and mass spectrometry imaging (MSI) have been proposed, and may have the advantage of high spatial resolution combined with high chemical specificity.[39] The future development of these synergistic approaches is keenly anticipated.

Hyperspectral SRS imaging is emerging as a high-content imaging platform for biological imaging applications (discussed further in Section 2.3). First, the rapid image acquisition associated with SRS microscopy enables up to video-rate imaging of live samples, and second, by acquiring a series of images across a range of frequencies, it is possible to create an SRS spectrum *i.e.* hyperspectral SRS image stack. This three-dimensional dataset, with spatial coordinates of x and y and a spectral coordinate (frequency, λ or cm^{-1}) at each pixel location can be used to identify the precise molecular composition. In combination with hyperspectral SRS imaging, many chemometric analysis techniques have been developed and applied to identify spectral features within the 3D dataset. A popular method for analysing hyperspectral SRS imaging is spectral phasor analysis which uses a Fourier transform to project every pixel in the 3D hyperspectral scan onto a 2D phasor plane.[40] In doing so, the spatial closeness of two phasors indicates their similarity which has enabled applications in the segmentation of single cells (Fig. 3D)[40] and tissue samples (Fig. 3E)[41] based directly on their respective SRS spectra. Phasor analysis has also been applied to studying drug-cell interactions,[42] cytometry applications[43–45] and intracellular enzyme sensing.[46]

Deep learning is a subset of machine learning that is capable of uncovering effective data representation across multiple spectral elements and is beginning to make an impact in modelling hyperspectral SRS imaging data. Neural networks are trained to learn prior information (*e.g.* peak shape, and peak position) from a training data series, thereby generating a high-quality output from an input of lower quality.[47] An application of deep learning was the use of a U-NET architecture for super-resolution SRS imaging enabled by expansion microscopy enabling multicomponent imaging of brain hippocampal

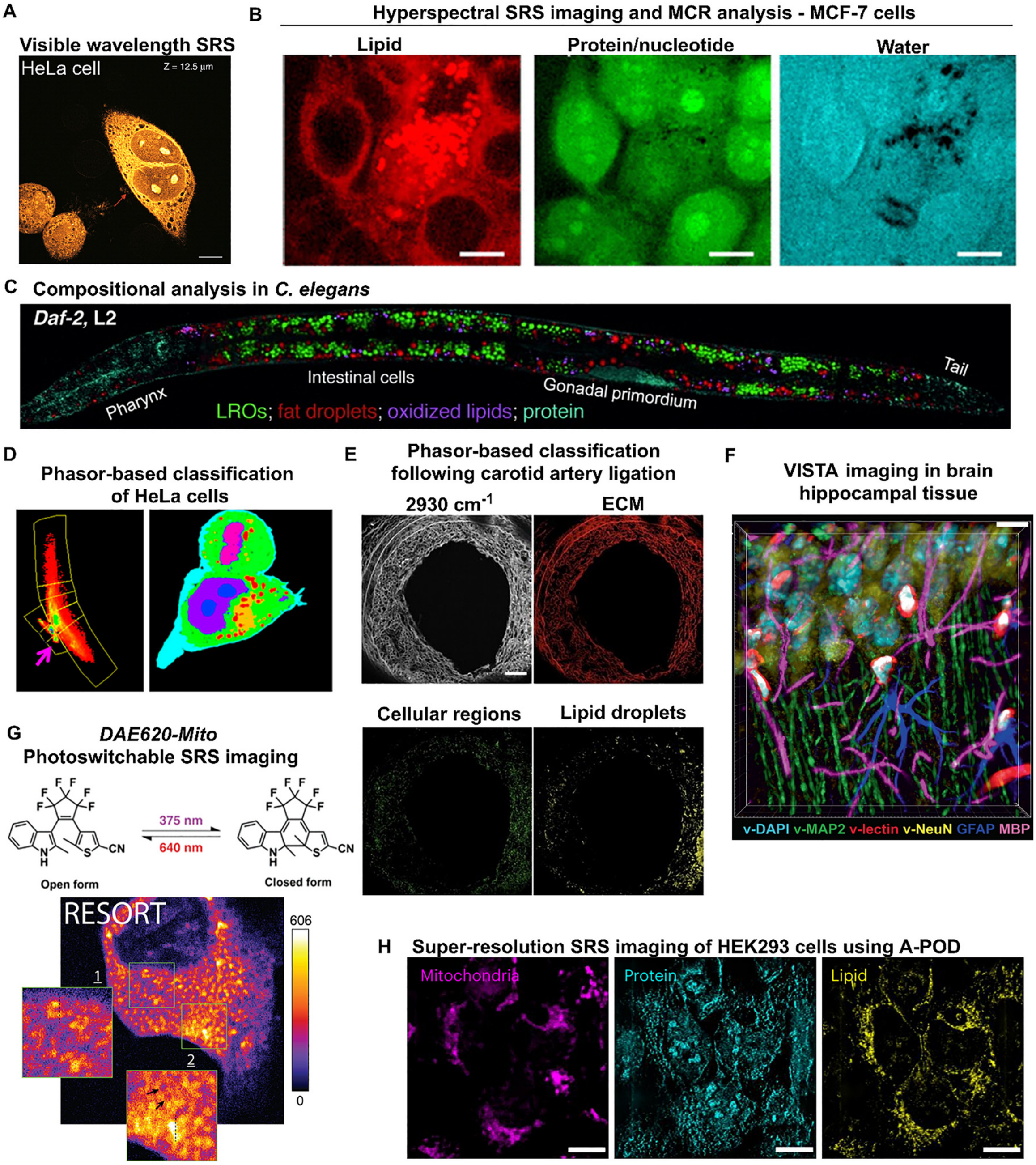

Fig. 3 Biological applications of SRS microscopy. (A) Label-free SRS imaging of a HeLa cell using visible excitation wavelength. The pump laser was 449.5 nm (1.7 mW) and the Stokes lasers was 520 nm (1.6 mW), respectively. Scale bars: 10 μm. Image reproduced from ref. 24 with permission from Nature Publishing Group.[24] Copyright 2018. (B) Hyperspectral SRL imaging and MCR analysis of breast cancer MCF-7 cells. Retrieved images of the lipid (red), protein/nucleotide (green), and water (blue) by MCR analysis. Scale bars: 10 μm. Images reproduced from ref. 52 with permission from American Chemical Society.[52] Copyright 2012. (C) Hyperspectral SRS imaging of a whole daf-2 mutant worm using MCR analysis. Scale bar: 50 μm. Image reproduced from ref. 32 with permission from Wiley.[32] Copyright 2014. (D) Hyperspectral SRS imaging across the range 2810–3090 cm^{-1} in HeLa cells with segmentation *via* spectral phasor analysis. The spectral phasor has been segmented into regions of interest (yellow boxes). A colour-coded cell image is provided alongside the segmented phasor plots. Image reproduced from ref. 40 with permission from American Chemical Society.[40] Copyright 2014. (E) Hyperspectral SRS was performed on tissue sections after carotid artery ligation (LGT). Example images and segmentation of ECM, cellular regions and lipid droplets following phasor analysis across the range 2800–3050 cm^{-1}. Images reproduced from ref. 41 with permission from Wiley.[41] Copyright 2023. (F) Multicolour imaging based on VISTA prediction and immuno-fluorescence imaging (GFAP (blue) and MBP (magenta)) in mouse hippocampal section. Scale bars: 40 μm. Image reproduced from ref. 48 with permission from Nature Publishing Group.[48] Copyright 2021. (G) Photoswitchable SRS imaging using DAE620-Mito. Structures of the open and closed forms of DAE620-Mito together with a super-resolution RESORT image of fixed HeLa cells at 1503 cm^{-1} (Raman on-resonance for DAE620-Mito). Image reproduced from ref. 50 with permission from American Association for the Advancement of Science.[50] Copyright 2023. (H) Super-resolution SRS imaging in HEK293 cells using A-PoD. Images reproduced from ref. 51 with permission Nature Publishing Group.[51] Copyright 2023.

sections (Fig. 3F).[48] Super-resolution SRS imaging has also been an area of active development.[49] For example, using photoswitchable reporters for SRS microscopy,[50] which are capable of alternating between an open and closed form, thus modulating their spectral features, can be used for super-resolution imaging. In a seminal work, Shou *et al.* developed a multiwavelength imaging scheme comprising of a pump and Stokes beam for SRS imaging, whilst the photoswitch was activated using a UV laser and a doughnut-shaped depletion laser to improve the point-spread-function (PSF) in a process referred to reversible saturable optical Raman transitions (RESORT) microscopy. The effective spatial resolution was 151 nm (Fig. 3G). Other methods to improving the spatial resolution in SRS microscopy have been achieved using deconvolution image analysis. Adam-based pointillism deconvolution (A-PoD) was developed to computationally improve the spatial resolution of SRS images to below 60 nm.[51] In this ground-breaking work, Jang *et al.* demonstrated that A-PoD could be applied to SRS imaging of cells, tissue and retinal sections for label-free super-resolution SRS imaging (Fig. 3H).

In summary, label-free SRS imaging has significant potential for studying cellular processes in real-time in a minimally invasive manner. A vast array of sample types and biological models have already been investigated using SRS which highlights the biocompatibility of the approach for imaging. We highlight the recent applications of SRS imaging related to drug discovery including, visualising drug uptake and localisation, imaging drug metabolism and cellular response to therapy, monitoring drug and excipient delivery to skin and lastly, the use of SRS imaging for analysing formulated drug products.

2.3. Hyperspectral SRS imaging

Single-frequency SRS microscopy has enabled the imaging of many discrete molecules of interest, although in many cases, the acquired signals can contain contributions from multiple endogenous species. This is particularly evident in the high wavenumber region of the spectrum which contains C–H stretching vibrations from multiple species, amongst others. The superimposed nature of these overlapping spectral features represents a challenge for identifying discrete biomolecular features using a single frequency Raman band. Hyperspectral imaging (*i.e.* analysing over a range of frequencies) with spectral unmixing methods is one method which can be applied to untangle the contribution of individual components of interest from overlapping signals in the spectrum.[52] In the case of hyperspectral SRS imaging, the spectral profile that results matches closely to the corresponding spontaneous Raman spectrum for straightforward sample characterisation.[53]

Techniques based on multispectral and hyperspectral imaging enable the visualisation of multiple components in the field-of-view, such that each pixel location in the image stack contains a spectral profile indicative of the components contained within it. Traditionally, multispectral imaging refers to Red-Green-Blue (RGB) imaging, where each pixel intensity value is denoted by an individual RGB intensity value. Because the SRS spectrum of biological samples may contain vibrational modes from a wide variety of different species (for example, lipids, proteins, and DNA), machine learning techniques can be applied to identify and segment a specific region-of-interest by comparison to hyperspectral imaging datasets with similar SRS spectral profiles. As such, chemometric analysis and machine learning techniques have been used to perform tasks such as classifying diseases, segmenting subcellular spatial features, improving image quality and/or resolution from hyperspectral SRS imaging datasets.

A convenient method to perform hyperspectral SRS imaging is through wavelength scanning of the pump beam to acquire SRS images across a range of values. Using picosecond (ps) laser sources, it is possible to acquire hyperspectral SRS images with a spectral resolution of $\sim 10\ \text{cm}^{-1}$.[54] Huang *et al.* developed a spectral compressor methodology which was shown to produce an effective spectral resolution of $5.4\ \text{cm}^{-1}$.[55] Using this approach, the group were able to differentiate eight types of saturated lipids with carbon chain lengths from C8:0 to C22:0 using the fingerprint SRS spectra. Heuke *et al.* developed a two-colour simultaneous SRS imaging system which produced two narrow-band Stokes laser beams (1–2 nm & 1–2 ps, separated by $\sim 100\ \text{cm}^{-1}$).[56] This method enabled the simultaneous acquisition of the following image pairs: CH_3 ($2940\ \text{cm}^{-1}$) & CH_2 ($2840\ \text{cm}^{-1}$) and CD_2 ($2149\ \text{cm}^{-1}$) along with an off-resonance/bioorthogonal Raman window ($2054\ \text{cm}^{-1}$). The advantage here was that where the signal-to-noise ratio was low, an off-resonance image could be simultaneously acquired with the desired on-resonance frequency to improve the image contrast. With simultaneous dual-colour imaging, motion artefacts and focal drift were avoided, which is particularly advantageous for recording on-resonance and off-resonance images pairs from Raman tags *e.g.* alkynes and nitriles.

In the case of hyperspectral SRS imaging based on ps laser sources, a sequential re-tuning of the pump laser is required in between image frames. A disadvantage of this technique is that the pump laser is susceptible to power and wavelength drift over the course of the spectral acquisition, resulting in spectral distortion. Conversely, the use of femtosecond (fs) laser sources for SRS has been widely reported,[57] however, these lasers have a broad spectral bandwidth resulting in poor spectral resolution ($\sim 25\ \text{cm}^{-1}$) in comparison to ps SRS imaging.[58] Spectral focussing techniques have been developed to recover the spectral resolution of fs SRS imaging, which use spectrally chirped laser pulses to narrow the Raman excitation bandwidth.[59] In practice, spectral focussing of fs laser sources using a dispersive element, typically a grating or glass rod, stretches out the broad range of frequencies contained within the temporally short fs pulse. By scanning the time delay between pulses, it is possible to ''focus'' on different vibrational transitions with high spectral resolution. This enables rapid hyperspectral imaging across a broad range of Raman frequencies by scanning the temporal delay. A further advantage of spectral focussing is that it offers better reproducibility, because there is no wavelength retuning, eliminating issues around laser stability and wavelength (and to a lesser extent, intensity) fluctuation over time. Recent examples of spectral focussing for fs SRS imaging have enabled applications in cellular segmentation[60] and chemical analysis in latent fingerprints.[61] Spectral focussing has also been applied to two ps laser sources enabling hyperspectral imaging with a spectral resolution down to 2 cm^{-1} with lower peak power amplitude for reduced phototoxicity.[62]

Hyperspectral SRS imaging has found broad applicability in biological microscopy by virtue of the combination of high spatial visualisation and chemically specific information which combines live-cell imaging and label-free detection. As such, applications in cellular segmentation have been widely reported which demonstrates the relative ease of these methods, especially when compared to methods that use cryo-EM,[63] which are particularly time consuming. In summary, hyperspectral SRS imaging couples the high spatial resolution of SRS with the spectral characterisation that is common within spontaneous Raman scattering. Hyperspectral SRS imaging has therefore, become a high-content imaging methodology for the analysis of a wide variety of sample matrices.

2.4. Quantitative SRS imaging for drug discovery applications

By combining high spatial resolution and vibrational chemical information, hyperspectral SRS has provided qualitative insight across a broad range of complex biological samples. An area which is much less developed is quantitative SRS imaging, where the absolute concentration of an analyte is determined with high spatial precision. Two of the main challenges which have hampered quantitative imaging are scattering at the laser focus and the non-Raman background signals which generally have a non-uniform intensity across the SRS spectrum.[64]

There are five main categories into which quantitative measurements from SRS imaging have been assigned. These include:

(i) Morphological measurements (*i.e.* feature number, feature size, feature shape *etc.*).

(ii) Semi-quantitative concentration measurements and relative concentration measurements, where the relative SRS signal intensity is used as substitute for concentration.

(iii) Absolute concentration measurement, where the SRS signal intensity is calibrated with respect to a concentration curve to enable a spatially resolved concentration map to be reported.

(iv) Ratiometric SRS measurements of two different peaks (*e.g.* CH_2/CH_3, lipids/proteins) are compared to provide a compositional insight.

(v) Ratiometric Raman sensing of a vibrational peak that shifts in wavenumber in response to dynamic changes in the surrounding microenvironment.

With direct relevance to this review, there are several applications highlighted in Section 3 where quantitative drug imaging has been achieved. In such studies, conversion of the grey scale SRS intensity values into absolute concentration has been performed. This is extremely challenging because of the requirement for calibration standards to be imaged under equivalent conditions (*e.g.* laser power and focus) and with optical properties that are consistent with the target sample (*e.g.* sample thickness and density). In creating a calibration curve for a series of stock concentrations, it is possible to convert the grey scale values for an SRS image of an unknown sample into a local concentration map. As a useful resource, a recent review outlines the practical considerations and standardisation of SRS imaging for quantitative analysis.[65]

3. Applications of SRS microscopy for imaging drug uptake, localisation and retention

3.1. Label-free SRS imaging of drug localisation

Of the drug classes imaged using SRS microscopy (select examples in Fig. 4), tyrosine kinase inhibitors (TKIs) have been the most extensively studied. In a seminal demonstration of SRS as a means to monitor the intracellular behaviour of therapeutic agents, Fu *et al.* visualised imatinib (Gleevec, **1**), nilotinib (Tasigna, **2**), and the inhibitors GNF-2 and GNF-5 within BaF3/BCR-ABL1 cells in a label-free manner through detection of Raman bands characteristic to each TKI.[66]

A principal advantage of SRS microscopes is their compatibility with other imaging modalities, which enabled the consecutive visualisation of imatinib (**1**) and nilotinib (**2**) and the fluorescent organelle stain, LysoTracker Red, in an approach that has become customary for studying the localisation of drugs and probe molecules (Fig. 5A).[66] Further, the linear dependence of observed Raman signal intensity on analyte concentration facilitated the determination of subcellular drug concentrations, with **1** and **2** found to be enriched within the lysosomes of BaF3/BCR-ABL1 cells by over 1000-fold when compared to the extracellular concentration. Tandem treatment of cells with **2** and the known lysomotropic agent, chloroquine (CQ), resulted in reduced lysosomal trapping of the drug and demonstrated the first example of the label-free quantification of drug-drug interactions using SRS microscopy.[66]

More recently, Wong *et al.* used SRS to investigate the role of organic cation transporters (OCTs) on the uptake and retention of the TKIs lapatinib (**3**) and afatinib (**4**) within A549 cells.[67] Peaks within the fingerprint region of the Raman spectra of the TKIs facilitated detection of the drugs within the cellular environment, and the authors used a spectral unmixing approach to deduce the lysosomal concentration of these compounds from hyperspectral SRS image stacks. The prior treatment of cells with OCT inhibitors resulted in varying levels of accumulation of the drugs within A459 cells, indicating that facilitated diffusion is vital to the uptake of the TKIs studied.

The rapid image acquisition time and high spectral resolution offered by SRS make it a powerful technology for the imaging of analytes within the intracellular environment. However, the slow retuning process and narrow spectral bandwidth of SRS lasers restricts the reliable detection of multiple analytes from different vibrational bands within dynamic biological systems, reducing the accuracy of ratiometric analyses or compound localisation assessment. Xu *et al.* developed an enhanced SRS system that employs three beams, generated by a femtosecond oscillator, which enabled the simultaneous

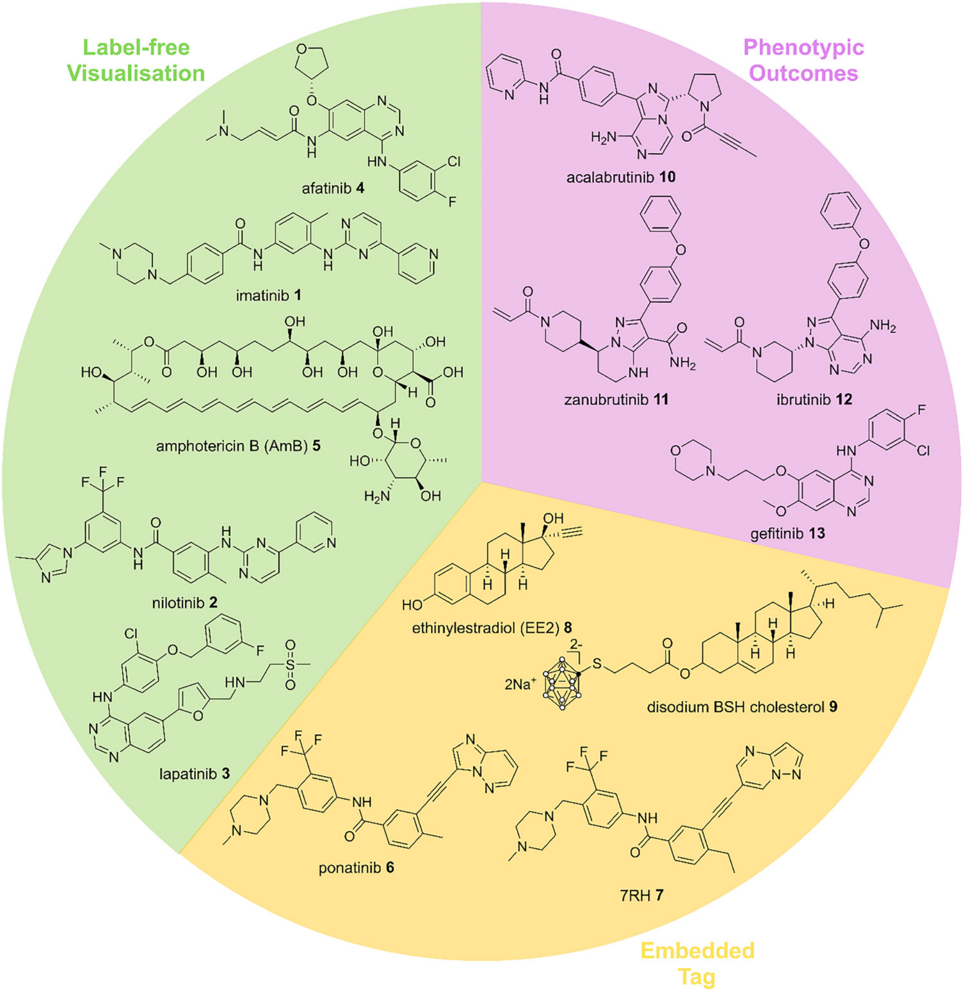

Fig. 4 Chemical structures of example small molecules that have been studied using label-free SRS microscopy.

acquisition of hyperspectral image stacks within distinct vibrational frequency ranges.[68] The authors simultaneously visualised lapatinib **3**, which possesses a characteristic Raman peak at 1368 cm^{-1} within the fingerprint region, and endogenous protein, at 2930 cm^{-1}, in A549 cells (Fig. 5B). Ratiometric analysis of the intensities of these two peaks across the field of view facilitated the visualisation of lapatinib **3** localisation, in a novel approach for the study of TKIs.

SRS has also been applied to the label-free intracellular visualisation of other drug classes. Amphotericin B (AmB, **5**) is a polyene containing lactone that targets ergosterol and is employed clinically against a number of fungal infections. Dong *et al.* used the C=C stretching mode, detected at 1556 cm^{-1}, as a handle for the visualisation of **5** within CASC5314 and CAC15 fungal cells using label-free SRS imaging.[71] In both cell types, AmB **5** was found to localise around the cell membrane, and Dong and co-workers then used polarisation-sensitive SRS to determine the orientation of the drug relative to the fungal membranes. In this approach, the SRS signal of analytes is known to be maximal when the pump and Stokes beams are polarised along the backbone of the molecule, and minimal when the laser fields are polarised perpendicular to this backbone. It was shown that AmB **5** molecules orientate parallel to the cell membrane phospholipid backbone, in agreement with traditional binding models for this drug.[72]

3.2. Drug imaging in the bioorthogonal region using embedded tags

Whilst SRS microscopy is a powerful technique for the label-free visualisation of drug molecules, the effectiveness can be enhanced by the incorporation of vibrational tags, such as alkynes, nitriles, C–D bonds and B–H bonds to the analyte of interest. This enables their straightforward detection from within the bioorthogonal Raman window of a Raman spectrum (1800–2800 cm^{-1}). Typically, analytes are furnished with vibrational tags, which may perturb the natural uptake, localisation, and metabolic fate of therapeutic agents. However, vibrational tags may be intrinsic to the drug molecule's architecture and thereby facilitate reliable imaging without disruption of their normal intracellular behaviours. A sizable fraction of the FDA approved library of drug molecules contain an alkyne group,[73] and significant opportunities exist for detecting the uptake and metabolism of different alkyne-containing drugs.[73] Sepp *et al.*

visualised the lysosomal localisation of ponatinib (**6**) within KCL22 and ponatinib resistant KCL22 (KCL22$^{\text{Pon-Res}}$) cells in a label-free manner using SRS microscopy through detection of the intrinsic alkyne bond within the drug at 2221 cm^{-1}.[69] The lysosomal concentration of **6** in the resistant cell line was ~1.9 times higher than in non-resistant cells and it was postulated that lysosomal trapping may facilitate drug resistance. To reduce the lysosomal accumulation of the drug, cells were tandem treated with CQ and **6**, which reduced the lysosomal concentration of **6** by 2.7 and 3.8-fold in KCL22 and KCL22$^{\text{Pon-Res}}$ cells, respectively (Fig. 5C), a result which was consistent with the observations made with imatinib and nilotinib (Fig. 5A). This study demonstrates the potential of SRS for informing treatment strategies in resistant cell lines.

The highly potent inhibitor of discoidin domain receptor tyrosine kinase 1 (DDR1), the experimental compound, 7RH (**7**), is structurally related to **6** and contains an intrinsic alkyne bond. Tipping *et al.* detected this alkyne at 2217 cm^{-1} using SRS to study the uptake of the drug in a variety of cell lines at different treatment concentrations.[70] In cell lines which express moderate levels of DDR1 (MCF-7, HCT 116, and A549 cells), and

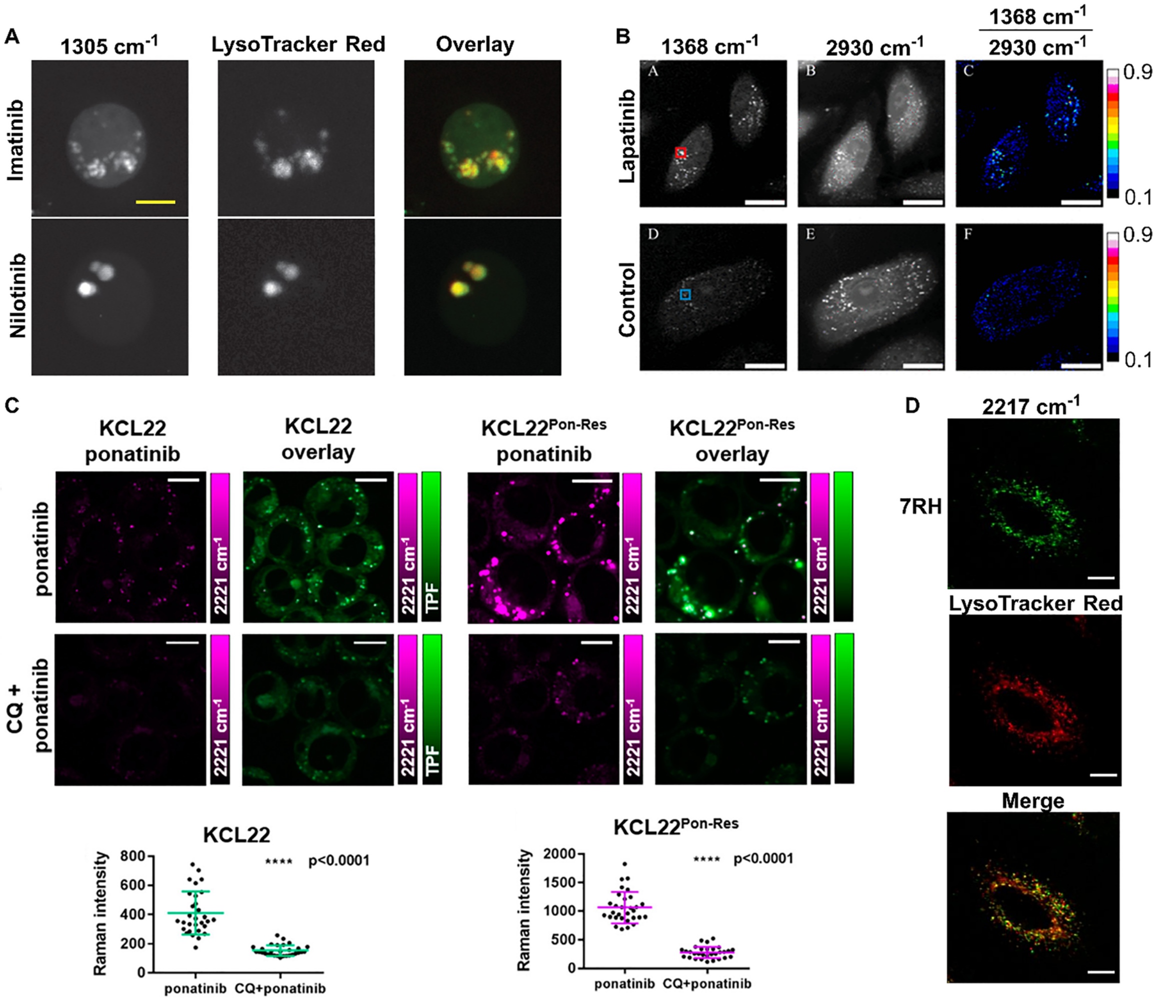

Fig. 5 Visualisation of TKIs within the intracellular environment using SRS. (A) Determination of the localisation of imatinib **1** and nilotinib **2** within BaF3/BCR-ABL1 cells. Tandem SRS-fluorescence images of BaF3/BCR-ABL1 cells treated with LysoTracker Red and either imatinib **1** (20 μM) or nilotinib **2** (20 μM). SRS image at 1305 cm^{-1} (imatinib **1** or nilotinib **2** signal). Images reproduced from ref. 66 with permission from Springer Nature.[66] Copyright 2014. (B) Simultaneous dual-band SRS imaging of lapatinib **3** and protein within A549 cells. A549 cells treated with lapatinib **3** (2 μM) or DMSO-d_6 control. SRS image at 1368 cm^{-1} (lapatinib **3**); SRS image at 2930 cm^{-1} (protein). Images reproduced from ref. 68 with permission from American Chemical Society.[68] Copyright 2023. (C) Effect of chloroquine (CQ) treatment on the vesicular uptake of ponatinib **6** within KCL22 and KCL22$^{\text{Pon-Res}}$ cells. (C) Top row: Tandem SRS-fluorescence imaging of KCL22 and KCL22$^{\text{Pon-Res}}$ cells treated with ponatinib **6** (5 μM) and LysoTracker Green. TPF = Two photon fluorescence signal. Bottom Row: Tandem SRS-fluorescence imaging of KCL22 and KCL22$^{\text{Pon-Res}}$ cells treated with CQ (20 μM) and then combination treatment of CQ (20 μM), ponatinib **6** (5 μM) and LysoTracker Green. SRS image at 2221 cm^{-1} (ponatinib **6**). A Comparison of ponatinib **6** Raman intensity within the vesicles of KCL22 and KCL22$^{\text{Pon-Res}}$ cells with and without CQ treatment. Images and charts reproduced from ref. 69 with permission from American Chemical Society.[69] Copyright 2019. (D) Multimodal imaging of 7RH localisation in A549 cells. Live cells were cultured in the presence of 7RH (500 nM, 2 h) and LysoTracker red (75 nM, 30 min) before imaging. Scale bars 10 μm. Image reproduced from ref. 70 with permission from Royal Society of Chemistry.[70] Copyright 2022.

a cell line that expresses low levels of DDR1 (MDA-MB-231 cells), similar uptake of **7** after two hours of treatment at both 5 μM and 500 nM concentrations was observed, suggesting that the uptake of the drug at these concentrations was independent of DDR1 expression. In A549 cells, tandem SRS and fluorescence microscopy revealed that 7RH was concentrated in lysosomes of the cells (Fig. 5D). A further technical development was realised by using a perfusion chamber approach which enabled the real-time monitoring of the uptake of **7** into MCF-7 cells. The rapid uptake of the drug molecule at a treatment concentration of 5 μM, and a slower accumulation at 1 μM was observed. Finally, the effect of tandem treatment with cisplatin and **7** on the viability of A549 cells was investigated. Multimodal SRS/fluorescence imaging of A549 cells treated with **7**, cisplatin and the commercially available live/dead fluorescent stains calcein-AM and ethidium homodimer (EthD-1) confirmed that the combination of the two drugs induced a greater reduction in cell viability than treatment with **7** alone.

Alternative therapeutic agents imaged using intrinsic alkyne groups as vibrational handles include ethinylestradiol (EE2, **8**), an alkyne containing estrogen receptor ligand employed in contraceptives and menopausal hormone therapies.[74] In contrast to the alkyne present in ponatinib **6** and 7RH **7**, the terminal alkyne of **8** is not capped with an aromatic ring system and therefore, displays a lower Raman signal intensity.[19] However, Mizguchi *et al.* employed surface-enhanced SRS (SESRS) to improve the Raman alkyne signal intensity of **8** through use of cetyltrimethylammonium bromide (CTAB) coated gold nanorods. The CTAB coating prevented terminal alkyne coordination to the metal surface and promoted the localisation of the lipophilic drug molecules to the vicinity of the gold nanorod, allowing the analytes to undergo the Raman signal intensity enhancement afforded by SESRS. The SESRS method resulted in an improved detection limit of **8** in solution by one order of magnitude when compared to traditional SRS and demonstrated how the combination of SRS with other Raman methods enables the detection of analytes with a weak Raman signal. However, the use of cumbersome metal nanorods, that may perturb normal biological function, hinders the utility of SESRS for the study of the native intracellular environment.

Boron neutron capture therapy (BNCT) is an emerging anticancer radiotherapy technique which enables localised ionisation damage to malignant cells through the irradiation of boron-containing drugs delivered to the tumour. Currently, sodium borocaptate (BSH) is one of two BNCT therapeutics undergoing clinical trials.[75] Asai *et al.* synthesised a cholesterol tagged analogue of BSH, disodium BSH-cholesterol (**9**), and visualised the compound within HeLa cells using SRS.[76] Through detection of the B–H stretching mode, which possesses a Raman shift of 2505 cm^{-1}, **9** was seen to localise at the cell membrane with an enrichment factor of >35-fold when compared to the extracellular treatment concentration. This study represents the first example of the visualisation of BNCT drugs using SRS, but the high treatment concentrations, owing to the inherently weak Raman signal intensity of B–H bonds, demonstrates a challenge in the use of B–H bonds as spectroscopic handles.

3.3. Visualising drug localisation through bioorthogonal tagging

Alternatively, analytes that do not contain intrinsic vibrational tags may be artificially furnished with C–D bonds, nitrile groups or alkyne bonds, to facilitate their detection by SRS (Fig. 6A). Propofol is a routinely administered general anaesthetic, but its small size has hindered the use of traditional methods, such as fluorescence microscopy, in the study of the intracellular behaviour of the drug. Oda *et al.* used SRS to visualise a deuterium labelled analogue of propofol (propofol-d_{17}, **14**), which was still efficacious for the suppression of cellular action potentials, within cultured hippocampal neurons.[77] Through SRS detection of the distinct C–D bond stretch at 2055 cm^{-1} within the cell-silent region, the compound was seen to primarily localise at the plasma membrane with an estimated enrichment factor of 1.3 compared to the extracellular treatment concentration of 100 μM. This high treatment concentration highlights one of the shortfalls of the use of C–D bonds as vibrational tags, which generate a reduced Raman signal intensity compared to alkyne groups.

Alkynes are significantly more effective than C–D bonds as vibrational tags. The conjugation of multiple alkynes further increases their Raman signature, affording high sensitivity labels for SRS microscopy which have been applied to the visualisation of several natural products and drug classes. Tipping *et al.* sought to investigate the intracellular behaviour of anisomycin, an inhibitor of protein synthesis known to be effective against a number of cancer cell lines, using a bisarylbutadiyne tagged analogue (**BADY-ANS**, **15**) and SRS.[78] After showing that **BADY-ANS 15** maintained efficacy as an inhibitor of the phosphorylation of JNK1/2 in SKBR3 cells, the compound was visualised intracellularly through detection of the distinct alkyne peak at 2219 cm^{-1}. Treatment of cells with a 10 μM solution of the drug, a relatively low treatment concentration, facilitated by the strong Raman intensity of the BADY scaffold, revealed the cytoplasmic concentration of the compound to be 50-fold enriched when compared to the extracellular concentration. The rapid imaging speed of SRS enabled the timelapse monitoring of **BADY-ANS 15** uptake by SKBR3 cells at one-minute intervals over a one-hour period, which demonstrated the high photostability profile of Raman vibrational tags when compared to fluorescent labels, which frequently show photobleaching of the signal upon repeated imaging. The authors then exploited the intrinsically narrow linewidths of Raman signals to simultaneously visualise **BADY-ANS 15** and EdU, an alkyne-tagged deoxyribonucleoside that is incorporated into the DNA of cells, in a dual-colour imaging experiment (Fig. 6B). SKBR3 cells were tandem treated with the two compounds and imaged at 2219 cm^{-1} to visualise **BADY-ANS 15** within the endoplasmic reticulum of cells, and at 2120 cm^{-1} to visualise EdU within the nuclear region. This approach holds potential

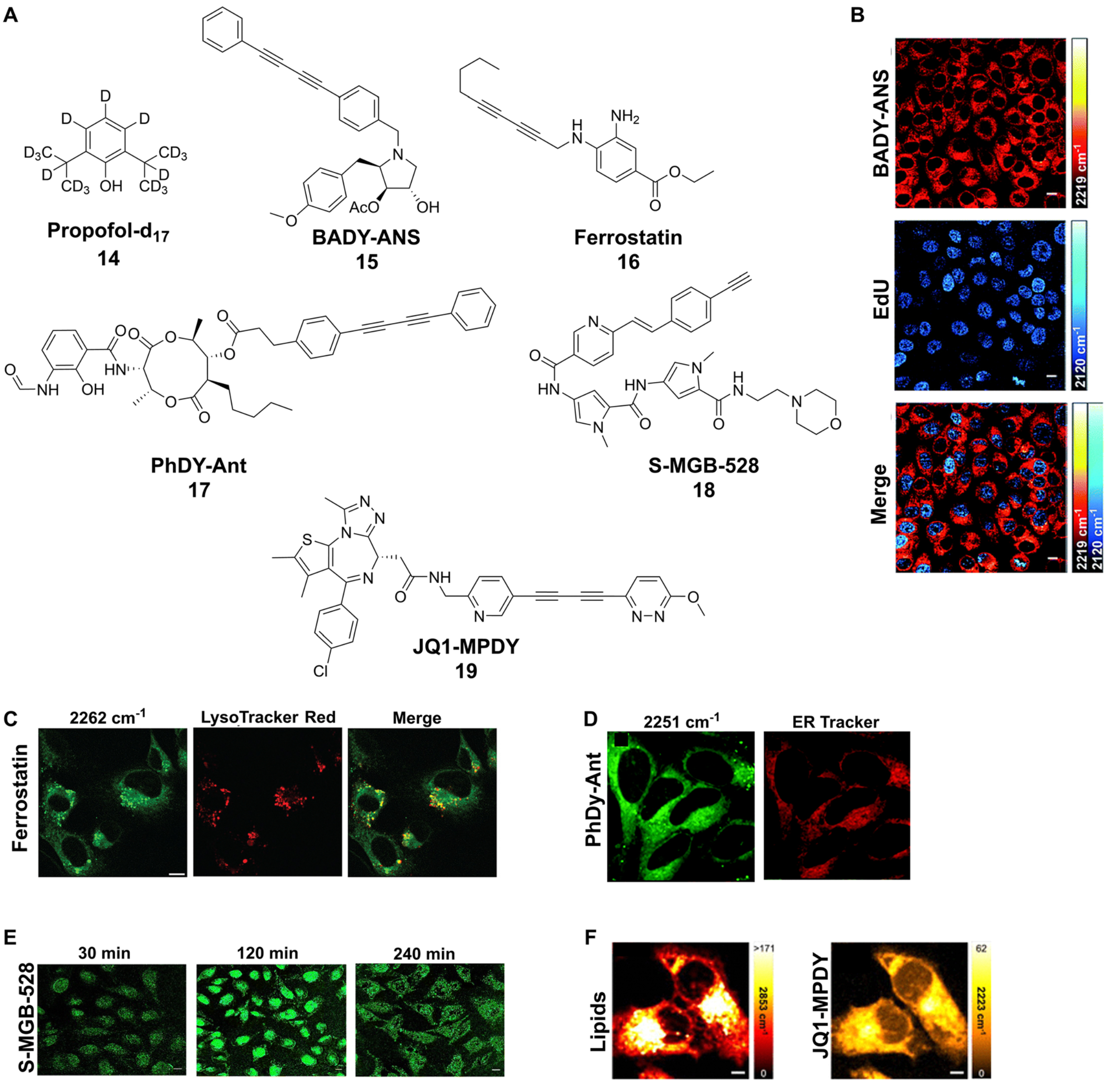

Fig. 6 Vibrationally-tagged drug molecules visualised using SRS microscopy. (A) Structures of artificially labelled drugs for visualisation using SRS. (B) Visualisation of EdU and **BADY-ANS 15** within SKBR3 cells. Cells were treated with EdU (100 μM, 18 h) and **15** (10 μM, 30 min). SRS image at 2219 cm^{-1} (**15**), SRS image at 2120 cm^{-1} (EdU). Images reproduced from ref. 78 with permission from Royal Society of Chemistry.[78] Copyright 2017. (C) Determination of the localisation of ferrostatin **16** within HT-1080 cells. Tandem SRS-fluorescence images of HT-1080 cells treated with LysoTracker Red (100 nM) and **16** (10 μM) 30 min. SRS image at 2262 cm^{-1} (16). Images reproduced from ref. 79 with permission from American Chemical Society.[79] Copyright 2018. (D) Determination of the localisation of antimycin analogue **17** within HeLa cells. Tandem SRS-fluorescence images of HeLa cells treated with ER Tracker and **17**. SRS image at 2251 cm^{-1} (**17**). Images reproduced from ref. 80 with permission from Royal Chemical Society.[80] Copyright 2019. (E) Lysosomal accumulation of **S-MGB-528 18** over time. SRS image at 2106 cm^{-1} (**18**). Images reproduced from ref. 81 with permission from Royal Society of Chemistry.[81] Copyright 2022. (F) Representative SRS images HeLa cells treated with **JQ1-MPDY 19** (6 μM) at 2853 cm^{-1} (lipids) and 2223 cm^{-1} (**JQ1-MPDY**). Scale bars: 5 μm. Images reproduced from ref. 82 with permission from American Chemical Society.[82] Copyright 2024.

for the future assessment of drug-induced effects on cell cycle progression using SRS.

The conjugation of multiple conjugated alkynes to form a polyyne further increases their Raman signature. For labelling purposes, diynes (occasionally referred to as bis-alkynes or 2-ynes) containing two conjugated alkynes have been used to visualise several natural products and drug classes due to the increased Raman scattering cross section that is afforded by conjugation. Hu *et al.* demonstrated the power of polyyne molecular engineering to enable multiplex detection based on conjugation length (1-yne to 6-yne), bond-selective isotope editing (^{12}C and ^{13}C) and end-capping substitution of polyynes.[18] Gashler *et al.* incorporated a bis-alkyne into the design of ferrostatin-1 analogues to investigate their intracellular localisation and mechanism of action during ferroptosis.[79] The authors observed the localisation of the alkyne-tagged ferrostatin analogue **16** between the lysosomes, mitochondria and endoplasmic reticulum (Fig. 6C). Interestingly, the localisation of **16** to the lysosome was shown to decrease the potency of ferrostatins, whilst no functional role of mitochondria in ferroptosis suppression by ferrostatins was also identified.

Seidel *et al.* visualised the cellular uptake and localisation of antimycin-type depsipeptides, a family of complex natural products of note for their potential as therapeutic agents, through incorporation of a phenyl-capped bis-alkyne moiety onto the structure of antimycin (PhDy-Ant, **17**).[80] After confirming that the alkyne-tagged analogue possessed similar activity to its parent compound, **17** was imaged within HeLa cells through detection of the alkyne peak at 2251 cm^{-1}. The intracellular concentration of the compound was determined to be 1.74 mM, indicating a 35-fold intracellular enrichment when compared to the extracellular concentration of the compound. SRS revealed that the uptake of the compound at 4 °C and 37 °C occurred at similar rates which suggested that the compound enters cells by passive diffusion. Further, multimodal SRS/fluorescence imaging of the alkyne-tagged analogue **17**, ER-Tracker Green and MitoTracker Deep Red confirmed that the compound accumulated within the endoplasmic reticulum (ER) of cells (Fig. 6D), and it was postulated that this was due to one of the drug targets, Bcl2, which is primarily located in the ER.

Recently, the bis-alkyne group has also been exploited in the design of peptidomimetics. A novel type of diyne-girder peptide stapling strategy was reported by Morgan *et al.* to create stable, α-helical peptidomimetics by incorporating a bis-alkyne linkage which resulted in a Raman-active conformational constraint. The alkyne staple was amenable to Raman imaging at 2255 cm^{-1}.[83] A similar diyne-girder stapling strategy has been applied to the p53 peptide for visualisation in ES-2 cells using SRS microscopy.[84] Considering the importance of peptide stapling in chemical biology, the diyne-girder approach offers a dual combination of conformational constraint and intracellular visualisation using Raman-based methods.

Minor groove binders (MGBs) are a class of therapeutic agent that bind the minor groove of DNA through a variety of mechanisms and hold great promise as drugs against bacterial and viral infections and cancer. Tentellino *et al.* used SRS to visualise an alkyne tagged Strathclyde-MGB (**S-MGB-528**, **18**) within HeLa cells after confirming that the addition of an alkyne group to the S-MGB did not induce a reduction in the DNA binding using thermal melt analysis.[81] Time course SRS visualisation of the uptake of **18** indicated that the compound initially localised to the nuclei of HeLa cells, but prolonged drug treatment resulted in nuclear saturation and cytoplasmic accumulation of the compound (Fig. 6E). Multimodal SRS/fluorescence imaging determined that the morpholine-containing **18** localised within the lysosomes of HeLa cells after nuclear localisation, consistent with other weakly basic drugs described in this review.

Kawaguchi *et al.* developed a methoxypyridazyl pyrimidyl butadiyne (MPDY) tag, a modified version of the popular bisarylbutadiyne (BADY) tag widely reported for SRS imaging of drugs.[82] The group visualised **JQ1-MDPY 19**, an MPDY-tagged analogue of JQ1, a bromodomain and extra-terminal motif (BET) inhibitor, in living HeLa cells by SRS microscopy. The tagged JQ1 analogues showed a pan-cellular distribution with enrichment in the nucleus which was consistent with the known localisation of the BET family proteins, which act as epigenetic readers in the cell nucleus (Fig. 6F). This article acknowledges some interesting features for the design of future Raman labels for drug tagging and imaging. Notably, the development of Raman tags with reduced lipophilicity and membrane permeability, to more closely match those of the parent molecule reducing tag-dependent, off-target accumulation, leading to an enhanced visualisation at target organelles. Secondly, the optimisation of Raman tag pK_a and solubility were highlighted as additional design indicators for tagged analogues that exhibit distributions similar to the original drug. Early work in this area showed that it is possible to fine-tune the Raman scattering properties by heteroatom substitution in the aromatic rings of the butadiyne scaffold. Ravindra *et al.* showed that varying the electronics of the end capping aromatic rings extended the spectral range of the BADY scaffold.[85] In addition, Steven *et al.* showed that through careful design, the stretching frequency of the butadiyne group could be varied through substitution of the phenyl end capping group with sp^3 hybridised motifs.[86] In addition, the $\log P$ and fraction sp^3 could be tuned, and ultimately, optimised based on the end capping groups to enable multiplex bioorthogonal detection with a potential reduction in off-target labelling by virtue of reduced $\log P$ characteristics.

In summary, SRS microscopy has enabled the imaging of a diverse selection of small molecules in cellular models. The ability to perform label-free detection of drug uptake, distribution and metabolism with high spatial and temporal resolution renders the technique suitable for preclinical drug evaluation. A neat extension of label-free SRS imaging of drug localisation has been through the detection of molecules which contain spectroscopically bioorthogonal Raman functional groups, including alkynes and nitriles which have been used as isosteres in medicinal chemistry across multiple drug classes. A future direction for bioorthogonal drug tagging is companion imaging diagnostics,[87] whereby SRS microscopy could be used to better understand druggable targets and identify molecules that reach their intended target. Lastly, the review also showcases the early promise of hyperspectral SRS imaging for spatial profiling following drug treatment. Combined, these applications indicate potential for hyperspectral SRS imaging in assessing the localisation and key functional outcomes in models of disease.

4. Visualising drug-cell interactions and metabolic outcome

Metabolism refers to the biochemical processes in living organisms that either produce or consume energy.[88] As such, metabolism represents the biochemical transformations that are tightly regulated towards the maintenance of cellular homeostasis. Chemical transformations are organised into metabolic pathways by which key functional biomolecules such as amino acids, nucleic acids and lipid species are synthesised or degraded. The dysfunction of certain metabolic pathways are strongly correlated to diseases including cancer,[89] cardiovascular diseases[90] and neurodegenerative diseases[91] amongst others.

Traditional bioanalytical methods including mass spectrometry, NMR spectroscopy and chromatography have been widely applied to study cellular metabolism, but in each case the biomolecular content is not assessed *in situ*, rather, extracted cell isolates or tissue homogenates are prepared. In these cases, population averaging is unavoidable and some key target molecules with low intracellular concentrations or transient lifetimes may become buried in the background of the predominant biomolecular content. Given that single-cell heterogeneity is becoming recognised as an important factor in understanding metabolism at the whole organism level,[92] techniques which offer *in situ*, subcellular detection of biomolecular interactions hold great promise. Whilst fluorescence microscopy is the front runner in subcellular imaging, largely due to the non-invasive nature of analyte detection and super-resolution imaging capability, fluorescence microscopy is largely reliant upon chemical probes and stains to generate image contrast. Consequently, the size and physiochemical properties of fluorescent probes will likely impact cellular metabolic pathways with unavoidable and unpredictable outcomes. Whilst the miniaturisation of optical reagents for fluorescence is an active area of research,[93] off-target imaging artefacts may well be unavoidable. To that end, metabolic imaging based on hyperspectral SRS microscopy is gaining traction to overcome these limitations by providing *in situ* metabolite detection with label-free or minimal perturbation through isotope profiling.

In the following sections, we first review the developments of hyperspectral SRS microscopy for probing cellular metabolism in cancer with a focus on lipid, protein and nucleic acid metabolism. In each of these areas, SRS microscopy has been shown to be a powerful method for investigating the metabolic outcome across a range of drug classes. We highlight the impact of hyperspectral SRS imaging for understanding drug-cell interactions and the potential for visualising therapeutic outcomes on whole cells. In addition, we review the development of SRS imaging for antimicrobial metabolism, by highlighting recent advances relevant to the drug discovery and medicinal chemistry landscape.

4.1. Imaging aberrant cholesterol metabolism in cancer

Lipid metabolism in cancer cells has been widely studied for therapeutic intervention because many tumour types have prominent lipid droplets which may be associated with enhanced cell viability, aggressive phenotypes and resistance mechanisms. The link between drug treatment and lipid metabolism is therefore an area of active investigation across many cancer subtypes.[94] SRS microscopy has been widely used for deciphering aberrant lipid metabolism in cancerous cells and tissues, together with investigating therapeutic strategies in the treatment of various cancers. Cholesterol metabolism is amongst the most widely studied using SRS microscopy. In an early investigation by Yue *et al.* the unexpected accumulation of cholesteryl esters (CEs) in high-grade and metastatic prostate tissues was demonstrated.[95] In a panel of prostate cell lines, CE accumulation was caused by the loss of tumour suppressor PTEN and the subsequent upregulation of PI3K/AKT/mTOR pathway. To determine the role of the PI3K/AKT/mTOR pathway in regulating CE accumulation, the authors used small molecule inhibitors LY294002 (a selective PI3K inhibitor), MK2206 (a selective AKT inhibitor) and rapamycin (a selective mTOR inhibitor). SRS microscopy at 2845 cm^{-1} (CH_2 symmetric stretch) revealed that the total lipid droplet amount was not reduced in CE-rich prostate cancer cell lines (PC-3 and LNCaP-HP), although Raman spectroscopy revealed CE levels as measured by the peak at 702 cm^{-1} (attributed to cholesterol rings) were reduced in PC-3 cells. In this combined SRS and Raman microscopy study, the authors concluded that CE accumulation is driven by the loss of PTEN and upregulation of the PI3K/AKT pathway. In a related study, Lee *et al.* demonstrated that inhibiting cholesterol esterification suppressed prostate cancer metastasis *via* impaired Wnt/β-catenin signaling.[96] Using a dual SRS microscopy and Raman spectroscopy approach, the inhibition of cholesterol esterification by avasimibe, an acyl-coenzyme A: cholesterol acyltransferase 1 (ACAT-1) inhibitor, reduced the CE content of cells and subsequently the metastatic potential of prostate cancer (Fig. 7A). From these early studies, the potential for targeting cholesteryl esterification in treating metastatic prostate cancer was demonstrated.

Aberrant accumulation of CEs mediated by ACAT-1 have been demonstrated in several other cancer models including pancreatic,[97,98] leukaemia[99] and renal cancers.[100] In each of these studies, Raman and SRS microscopy have been used to characterise CE metabolism and storage using a combination of the Raman modes at 702 cm^{-1} and 2845 cm^{-1}. The depletion of CEs was observed across the different cell lines used in these studies following treatment with ACAT-1 inhibitor, avasimibe. However, a major challenge associated with the intratumoural delivery of avasimibe is the hydrophobic nature of the drug, resulting in poor blood bioavailability. To address this issue, Lee *et al.* developed a nanoformulation called avasimin for intravenous delivery of avasimibe.[101] The group encapsulated avasimibe in human serum albumin to overcome the inherent low water solubility of the compound in order to deliver an effective dose to the tumour site. The formulation showed a highly effective reduction in the CE content across a variety of cancer cell lines using SRS microscopy at 2845 cm^{-1}. Together these studies demonstrate the versatility of hyperspectral SRS microscopy for investigating cholesterol metabolism in cancer cell models, particularly during therapy and treatment. A remaining challenge in this area would be the detection of the 702 cm^{-1} cholesterol ring mode which has been primarily detected using Raman scattering. The detection of low frequency modes in the SRS spectrum is not routinely conducted, in part due to a restriction on the tuneable range of some ps laser sources.

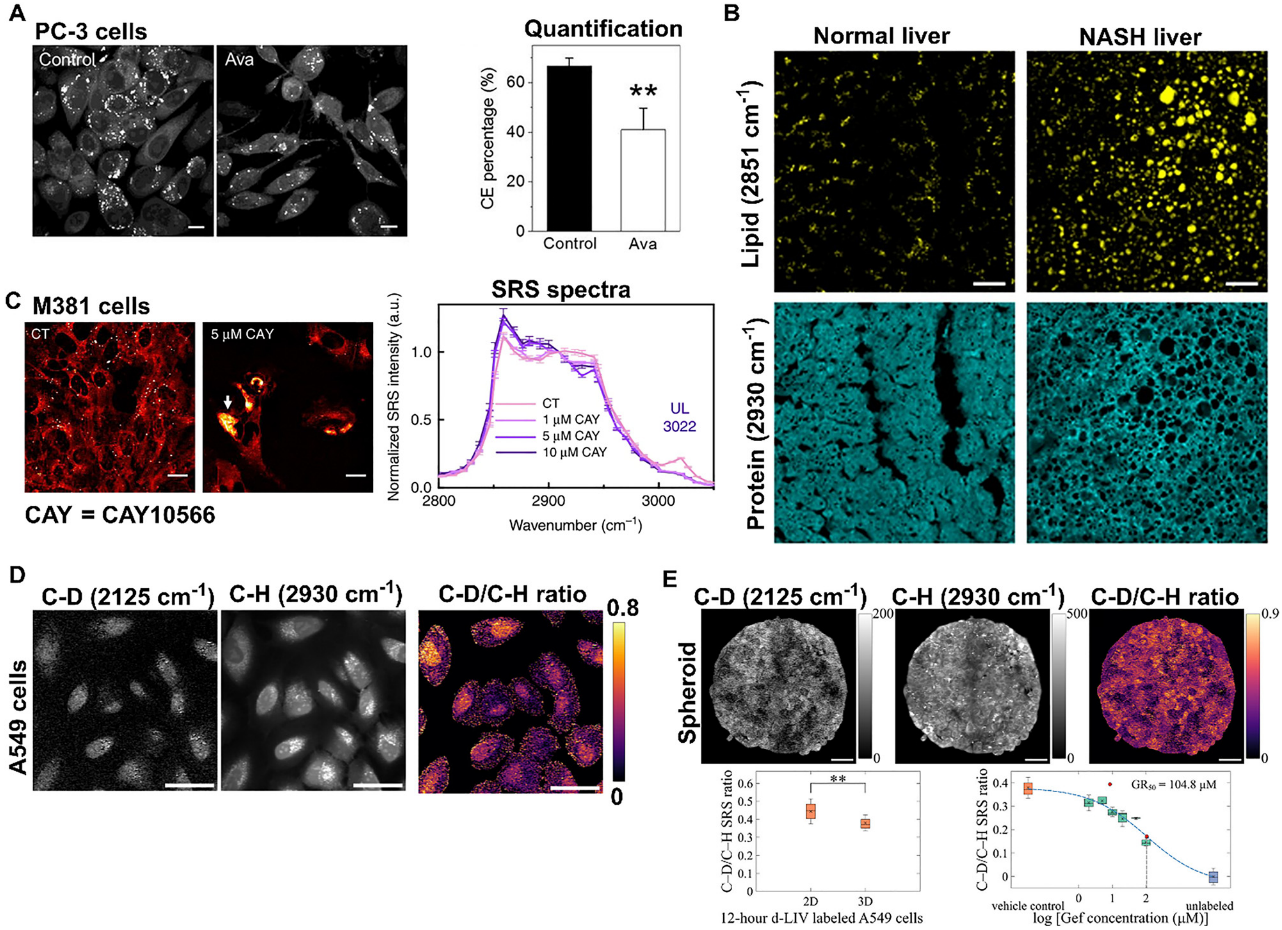

Fig. 7 Visualising drug-cell interactions and phenotypic outcomes using SRS microscopy. (A) SRS images of PC-3 cells treated with avasimibe (5 μmol L^{-1}, 3 days) *vs.* control cells. Scale bar: 10 μm. Quantification of the cholesterol ester (CE) percentage is also presented. Images reproduced from ref. 96 with permission from American Association for Cancer Research.[96] Copyright 2018. (B) Decomposed images of lipid (2850 cm^{-1}), and protein (2930 cm^{-1}) of a normal liver (HH1142) and a non-alcoholic steatohepatitis (NASH) liver (UMN1249). Scale bars: 50 μm. Images reproduced from ref. 105 with permission from Nature Publishing Group.[105] Copyright 2018. (C) SRS imaging of melanoma cell line exposed to DMSO (control, CTL) or CAY10566 (a SCD1 (Δ9-desaturase inhibitor)). Hyperspectral SRS imaging shows a decrease in unsaturated lipid (UL) content at 3022 cm^{-1} with increasing [CAY10566]. Images reproduced from ref. 113 with permission from Nature Publishing Group.[113] Copyright 2020. (D) Live A549 cells were treated with lapatinib (5 μM, 24 h) before d-LIV (6 h). SRS images were acquired at 2125 cm^{-1} (C–D region) and 2930 cm^{-1} (C–H region). Ratiometric imaging was used to demonstrate the response to lapatinib treatment. Images reproduced from ref. 117 with permission from American Chemical Society.[117] Copyright 2024. (E) Representative SRS images of the C–D and C–H region together with a ratiometric SRS image formed from A549 spheroids following a 12 h d-LIV labelling method. A comparison of the growth rate in the 2D and 3D cultures is also provided. Significance: **: $p \leq 0.01$. Lastly, a comparison of the SRS ratio of C–D/C–H in an A549 spheroid following treatment with varying concentrations of gefitinib for 12 h using this method is provided. Scale bar: 50 μm. Image reproduced from ref. 118 with permission from American Chemical Society.[118] Copyright 2023.

4.2. Investigating lipid saturation in cancer and other diseases

Using hyperspectral SRS microscopy across the high wavenumber region (2800–3050 cm^{-1}) of the SRS spectrum, Li *et al.* identified a significant increase in unsaturated lipid content in ovarian cancer stem cells (CSCs) compared to non-CSCs.[102] The detection of unsaturated lipid content was achieved using the ratio, 3002/2900 cm^{-1} (=C–H/C–H total lipids), which revealed the differences in lipid unsaturation across a panel of ovarian cancer cell lines. This ratio was also elevated in the lipid droplets associated with spheroids compared to monolayer cultured cells. The authors corroborated their hyperspectral results using Raman spectroscopy in the fingerprint region, specifically using the peaks at 1264 cm^{-1} (in plane bending =C–H), 1450 cm^{-1} (CH$_2$ bending) and 1660 cm^{-1} (C=C stretching). In a combined Raman and SRS imaging approach, Wang *et al.* showed that increased lipid efflux and oxidation, along with decreased lipid synthesis, were potential contributors to the reduced lipid levels in glioblastoma tissues with low O6-methylguanine-DNA methyltransferase (MGMT) methylation.[103]

More recently, Rensonnet *et al.* showed that fingerprint SRS microscopy could be used to probe lipid unsaturation in hepatocellular carcinoma cells exposed to cyclosporin A.[54] In this work, the authors applied spectral phasor analysis for segmentation of the cellular lipid droplets before SRS imaging across the fingerprint region (1200–1780 cm^{-1}). Spectral phasor analysis is a Fourier transform-based technique that projects the pixels from a 3D hyperspectral scan onto a 2D phasor representation, whereby the spatial closeness of pixels on the phasor plot indicates their spectral similarity. Their results identified lipid desaturation as a signature of the lipid droplet accumulation following cyclosporin A treatment as a model to study drug-induced steatosis. Tipping *et al.* extended this approach to investigate the nature of accumulated lipids following exposure to cationic amphiphilic cations (CADs) to probe drug-induced phospholipidosis.[104] The use of spectral phasor analysis was shown to be a convenient method to differentiate aberrant lipid accumulation profiles based on drug-induced phospholipidosis (DIPL) and drug-induced steatosis (DIS). Using hyperspectral SRS imaging together with spectral phasor analysis, the authors showed that the lipid accumulation profiles were different between the drug treatments resulting in DIPL and DIS which are two mechanisms associated with drug-induced liver injury. DIS refers to the accumulation of lipids in the form of diacyl and triacylglycerols together with cholesterol esters within intracellular lipid droplets (LDs), which are coated by a phospholipid monolayer. DIS is typically associated with off-target effects of a drug. DIPL refers to the accumulation of phospholipid membranes within a multilayered/multilamellar structure, typically associated with the exposure to CADs. Interestingly, the method was also able to screen molecules of unknown DIPL status, indicating a potential application of this methodology for the evaluation of candidate small molecules in the early stages of clinical evaluation. In a similar approach, Urasaki *et al.* demonstrated that hyperspectral SRS imaging with spectral phasor analysis was capable of quantifying liver steatosis in patient tissue samples (Fig. 7B),[105] whilst other studies have demonstrated the application of multimodal SRS imaging for investigating liver fibrosis.[106] Combined, these reports show clear potential for investigating drug-induced liver injury without the use of fluorescent stains or dyes to do so.

Towards a similar aim, Zhuge *et al.* developed visible pre-resonance SRS microscopy to probe retinoid storage in mammalian cancer cell lines.[107] Electronic pre-resonance SRS imaging[108] significantly enhances the detection sensitivity of an analyte by applying a pump wavelength that is close to the electronic absorption wavelength of the molecule. In this work, the pump and Stokes wavelengths were frequency doubled to 482 and 522.5 nm, respectively, which approaches the retinoid absorption at 325 nm, thereby resulting in pre-resonance enhancement of the SRS signal. By probing the fingerprint region of the SRS spectrum, the authors identified two types of lipid droplet within the pancreatic cancer cell line, MIA PaCa2 and ovarian cancer cell line, OVCAR. The detection of the Raman peak at 1655 cm^{-1} was attributed to lipid droplets composed primarily of triglycerides, whilst the detection of the retinoid peak at 1580 cm^{-1} was localised to some, but not all, lipid-rich areas. By applying spectral phasor analysis to delineate the two types of lipid droplets, the authors observed an increase in the retinoid-containing lipid droplets in drug resistant pancreatic cells and drug-resistant ovarian cells when compared to the drug-sensitive counterparts. The method demonstrated that lipid storage is a potential feature of chemoresistance in cancer. Yan *et al.* expanded the use of hyperspectral SRS microscopy across the region 2800–3050 cm^{-1} to characterise lipid unsaturation in human liver cancer samples.[109] In this work, the detection of saturated lipid content was detected in the cancerous regions of tissue but not in adjacent normal tissue, suggesting that the accumulation of saturated lipid content could be a spectroscopic and metabolic marker for human liver cancer. Collectively, these studies highlight the potential for hyperspectral SRS microscopy in identifying features of chemoresistance at the cellular level together with tissue analysis.

Yuan *et al.* investigated the uptake of fatty acids with varying degrees of unsaturation into U937 glioblastoma cells.[110] In this study, the uptake of saturated palmitic acid, monounsaturated oleic acid and polyunsaturated eicosapentaenoic acid resulted in accumulation of the lipids into lipid droplets as evidenced by increases in the SRS signal at 2854 cm^{-1} (CH_2 symmetric stretch) and 3015 cm^{-1} ($=$C–H). The authors demonstrated that inhibition of TAG synthesis using the inhibitors T863 and PF-06424439 resulted in a depletion of LDs with an enhanced lipotoxicity profile, particularly when used in combination. In a therapeutic context, Allen *et al.* investigated the impact of X-ray radiation on lipid droplet size and distribution in MCF-7 breast cancer cells.[111] In this study, exposure to X-rays resulted in an increase in the lipid intensity as detected by the SRS signal and an overall increase in cell size as a result of cell damage *via* multinucleation (a process whereby a cell has more than one nucleus).

4.3. Isotopic labelling for investigating lipid metabolism in cancer

Tan *et al.* used SRS microscopy to study cisplatin resistance in ovarian cancer cells.[112] The group showed that increased fatty acid uptake accompanied by decreased glucose uptake and lipogenesis is a feature of cisplatin resistance. Using deuterated palmitic acid-d_{31} and oleic acid-d_{34} as probes for exogenous fatty acid uptake, and glucose-d_7 as a probe for glycolysis, SRS imaging revealed a significant decrease in glucose-derived C–D signals and an increase in deuterated FA signals in the resistant cell lines compared to the parental cell lines. In a related study, the metabolic reprogramming of melanoma cancer cells towards FA synthesis was probed by Du *et al.*[113] Within this study they combined hyperspectral SRS imaging with transcriptomic analysis to identify the relationship between cellular differentiation and metabolic reprogramming amongst melanoma cancer cell phenotypes. The authors identified the fatty acid synthesis pathway as a druggable target for differentiated melanocytic cells and by using hyperspectral SRS imaging of intracellular lipid droplets, identified lipid mono-unsaturation as a susceptibility within de-differentiated mesenchymal cells with innate resistance to BRAF inhibition (Fig. 7C). Lastly, Zhu *et al.* demonstrated SRS imaging of deuterium labelled palmitic acid-d_{31} and arachidonic acid-d_{11} which were incorporated into lamellar and punctate structures representing incorporated fatty acid metabolites in endoplasmic reticulum membranes and lipid droplets in HeLa cells, respectively.[114]

4.4. Imaging protein metabolism

Two main strategies have been developed concurrently to investigate protein metabolism in single cells using hyperspectral SRS microscopy. First, isotopically edited amino acid precursors have been added to the relevant culture medium, such that metabolic incorporation during protein synthesis labels the proteome with deuterated monomers. Second, D_2O has been used to replace the water content in the cell culture medium for global metabolic turnover studies. Where D_2O is included in mammalian cell culture, the result is metabolic labelling of proteins together with lipid, nucleic acids and other metabolic products, which necessitates the development of spectral unmixing to identify the nascent protein signals.

In an early study, Wei *et al.* incorporated a deuterium labelled set of all 20 amino acids to leucine-, lysine-, and arginine-deficient DMEM.[115] In doing so, the incorporation of C–D Raman signals within the nascent proteome were visualised at 2133 cm^{-1} throughout HeLa cells and, in particular, within the nucleoli, which was consistent with their known activity as the site of ribosomal biogenesis. The authors showed that protein synthesis was effectively inhibited by the natural product, anisomycin, together with the visualisation of a cell undergoing mitosis following a 20 h incubation with deuterated amino acid medium. This method was extended to visualise complex protein metabolism in animals including mouse brain tissue and zebrafish embryo.[116] Recent innovation in this area has surrounded the development of novel cocktails of deuterated amino acids to probe nascent protein metabolism. A recent report demonstrated the use of three branched-chain essential amino acids, leucine, isoleucine and valine (d-LIV) for deuterium labelling of protein synthesis (Fig. 7D).[117] As the cells grow in culture medium supplemented with d-LIV, the cells uptake and metabolise the C–D bonds into their nascent protein content. This enabled the authors to probe the growth rate of 2D and 3D cell models in response to drug treatment, where the deuterium labelled protein signals (2125 cm^{-1}) for the new proteome, and the C–H SRS signals (2930 cm^{-1}) were used to identify the unlabelled protein content. Further, Xi Xu *et al.* used deuterated analogues of valine, leucine, and isoleucine as spectroscopic markers to assess the growth of A549 cells following treatment with the TKIs gefitinib (**13**) and lapatinib **3**.[118] Through simultaneous dual-band SRS detection, the deuterated amino acids and endogenous proteins could be visualised by imaging at 2125 cm^{-1} (C–D) and 2930 cm^{-1} (C–H), respectively. The C–D/C–H intensity ratio, a reflection of the incorporation of the vibrationally tagged amino acids into cellular protein structures by protein synthesis, was used as a metric for quantifying cell growth. Treatment with **13** or **3** resulted in a decrease in the C–D/C–H ratio, indicating a reduced rate of cell growth as a result of TK inhibition. The authors correlated the ratio of C–D/C–H to identify the growth rate of 2D cells and 3D spheroid models against a panel of drugs including kinase inhibitors (*e.g.* gefitinib), mitotic inhibitors, and topoisomerase II inhibitors (Fig. 7E). This approach offered a faster turnaround time for assessing drug-cell interactions in a high-content image screening approach. An alternative method to probe protein synthesis dynamics was reported by Shen *et al.* who applied ^{12}C-phenylalanine and ^{13}C-phenylalanine ring-breathing modes at 1004 cm^{-1} and 968 cm^{-1}, to visualise the old and new proteomes, respectively.[119] The group demonstrated a reduction in protein metabolism under oxidative stress conditions using this approach. In summary, a variety of isotopic labelling strategies have been developed resulting in significant success for investigating protein metabolism in the cellular environment.

In addition to direct phenotypic imaging of protein metabolism, SRS can also be applied to the study of cellular phenotypic outcomes in response to treatment with therapeutic agents. Liu *et al.* visualised the effect of the TKIs, acalabrutinib (**10**), zanubrutinib (**11**) and ibrutinib (**12**) on lipid droplet formation within mantle cell lymphoma (MCL) cells in a label-free manner.[120] Through imaging at 2845 cm^{-1} (C–H), the total protein and lipid content was detected, and by using an intensity threshold, the authors were able to quantify the significant reduction in LD formation as a result of treatment with each of the TKIs.

4.5. Antibiotic susceptibility testing using hsSRS

Antimicrobial resistance (AMR) is a major threat to human health worldwide. The detection and quantification of resistance is key to preventing the emergence and spread of AMR.[121] Antimicrobial susceptibility testing (AST) uses diagnostic techniques to phenotype and genotype AMR.[122] A major limitation of AST methods is their respective speed: in many cases, overnight incubation is required for bacterial identification and an additional 24–48 h to perform AST. As such, rapid bacterial identification and AST are prerequisites in the pursuit of novel methodologies in this area. Techniques based on vibrational spectroscopy are emerging as promising new AST detection systems,[123] with significant research effort directed towards SRS microscopy as a high throughput method for detecting spectral biomarkers of AMR. SRS was first applied to AST development through the quantitative detection of bacterial metabolism in the presence of glucose-d_7. Using hyperspectral SRS imaging, Hong *et al.* showed that bacterial susceptibility and minimum inhibitory concentration (MIC) can be determined within 0.5 h in vancomycin-susceptible enterococci (VSE) and vancomycin-resistant enterococci (VRE) (Fig. 8A).[124] This approach elected to use glucose-d_7 which is the predominant carbon source for most bacterial growth.[125] To maximise the C–D signal level, a custom-made culture medium, in which glucose-d_7 is the only carbon source, was prepared. In the antibiotic-resistant population, the detection of C–D vibrational modes at $\sim$2178 cm^{-1} was performed, and by contrast, in the susceptible populations, a significant reduction in C–D signal was observed in the presence of vancomycin (20 μg mL^{-1}). This type of AST, sometimes referred to as 'phenotypic resistomics',[121] is an attractive methodology because no prior information regarding the bacterial strain is required, and the technique was shown to be highly effective across different

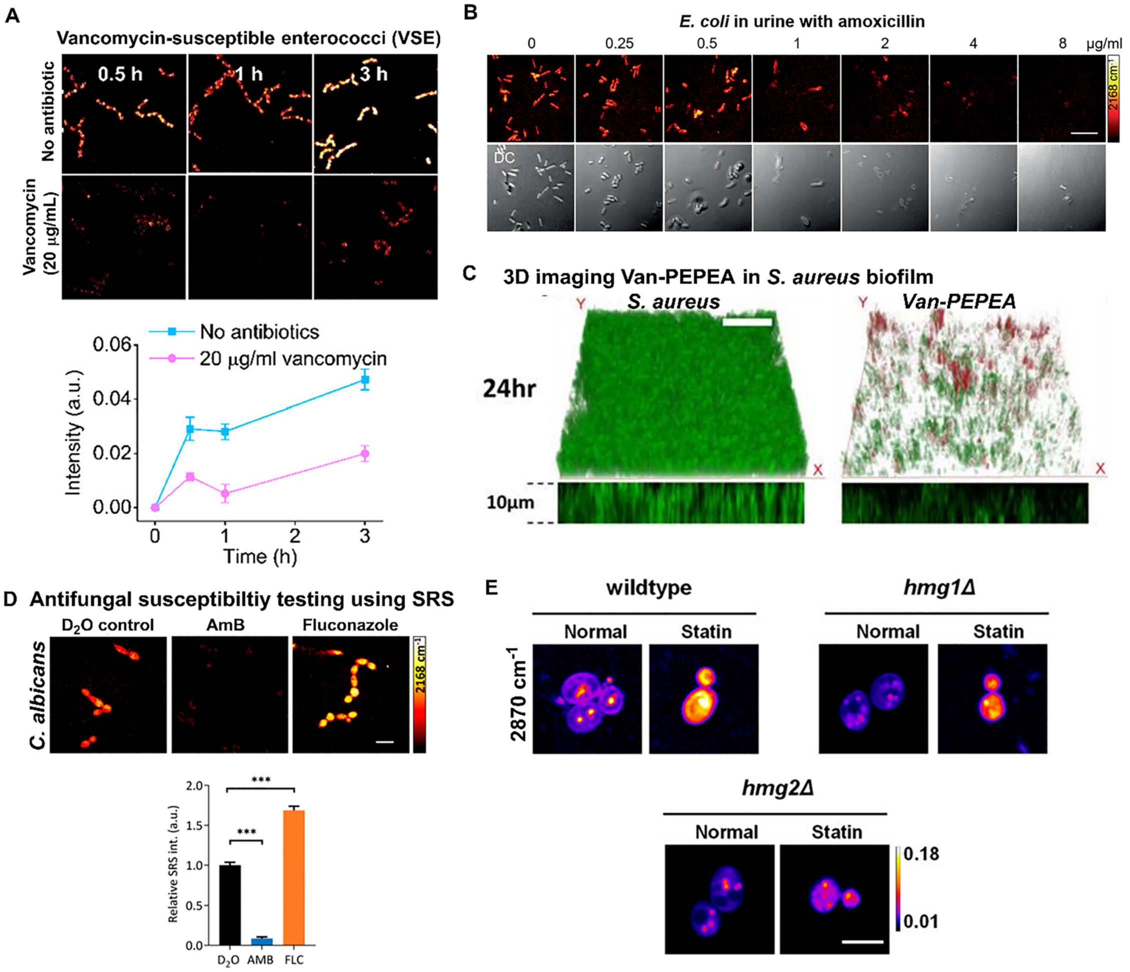

Fig. 8 Antimicrobial activity screening using SRS microscopy. (A) Time-lapse SRS imaging of vancomycin susceptible enterococci (VSE) metabolism using glucose-d_7 in the presence of vancomycin. Quantitation of C–D component intensity changes with time in the presence and absence of vancomycin. Error bars indicate standard deviation (number of cells > 30). Images reproduced from ref. 124 with permission from American Chemical Society.[124] Copyright 2018. (B) SRS imaging and transmission imaging of *E. coli* in urine samples following 1 h culture in D_2O-containing medium containing amoxicillin. Image reproduced from ref. 126 with permission from Wiley.[126] Copyright 2020. (C) 3D visualization of *S. aureus* (green) and van-PEPEA (red) following incubation with van-PEPEA for 24 h. Images reproduced from ref. 134 with permission from IvySpring Publishing.[134] Copyright 2019. (D) SRS imaging of *C. albicans* incubated in D_2O containing amphotericin B (AmB) or fluconazole at a concentration of 8 μg mL^{-1}. Scale bar: 20 μm. Quantification of the relative C–D intensity in the *C. albicans* cells under each condition shows sensitivity to AmB, and resistance to fluconazole treatment. Number of cells ≥10 per group with error bars representing the SEM. Images reproduced from ref. 139 with permission from American Chemical Society.[139] Copyright 2023. (E) The effect of two HMGR isozymes of *S. cerevisiae* yeast in response to statin treatment. Representative SRS images at 2870 cm^{-1} display the ergosterol distribution (normal) and following simvastatin treatment (statin, 100 μM, 6 h). Images reproduced from ref. 141 under CC BY license and copyright (2023, the authors).[141]

bacterial species including *Escherichia coli*, *Klebsiella pneumoniae*, and *Staphylococcus aureus*. For example, the authors demonstrated that *E. coli* was susceptible, and *K. pneumoniae* was resistant to gentamicin, cefotaxime, and amikacin when treated with 20 μg mL^{-1} of each compound.

Building on this early work, most SRS-based metabolic imaging studies have opted to use D_2O as a deuterium source in bacterial AST culture, in much the same way as previous studies investigating protein metabolism in mammalian cells (Section 4.4). In doing so, several key developments have been realised. Zhang *et al.* demonstrated the detection of D_2O metabolism in a variety of bacteria-antibiotic combinations in clinically relevant substrates including urine and whole blood samples.[126] Using 70% D_2O enriched medium, the rapid detection of bacterial metabolism was observed. An advantage of using D_2O in AST is that the resulting C–D vibrations (typically 2100–2300 cm^{-1}) are spectrally isolated compared to the O–D vibrations (typically 2300–2750 cm^{-1}),[127] thereby resulting in background-free SRS measurements. In addition, D_2O can be incorporated into standard culture media and broth, thus simplifying the experimental workflow and enabling access to a wider variety of bacterial strains to be evaluated using this method compared to glucose-d_7 labelling. Using 14 clinically relevant antibiotics against a panel of 37 bacterial isolates, the authors compared the results to broth microdilution data. This method achieved a 94.6% categorical agreement between the two readouts. The authors also showed that the single-cell metabolism inactivation concentration (SC-MIC) of bacteria upon exposure to antibiotics in clinical samples, including in whole blood and urine, can be obtained after a total of 2.5 h of sample preparation and detection (Fig. 8B).[126,128]

A hybrid analytical approach was developed by Sun *et al.* to investigate AST in positive blood culture.[129] Here, the authors used a semi-automatic centrifugation step to isolate and concentrate the bacterial component of positive blood culture bottle samples. Subsequently, the use of MALDI-TOF mass spectrometry was applied to bacterial identification, whilst the remainder of the bacterial samples were cultured in 70% D_2O enriched medium for 2.5 h. The SC-MIC values were determined across a panel of 105 samples with a correct identification rate of 92.3%. In a related study, Zhang *et al.* capitalised on the high spatial resolution of SRS microscopy to improve the accuracy of AST by morphological assessment together with D_2O labelling intensity.[130] Since β-lactam antibiotics result in the deformation of Gram-negative bacteria, the authors demonstrated that the accuracy and reliability of AST could be improved by determining the ratio CD + CD/area. A sample size of 103 *E. coli* strains were tested against the β-lactam antibiotic, cefotaxime. With the two quantifiable markers of CD incorporation and bacterial cell area, the new method achieved a 93.2% categorical agreement with the standard reference method.

Although the SRS imaging assays described show considerable improvements in the detection time for AST compared to conventional culture-based methods, the calculation of SC-MIC value is typically performed manually. To address this issue, Sun *et al.* have recently developed a U-net convolutional neural network (CNN) to automatically segment single bacteria from SRS images as part of an AST screening progamme.[131] The automated method was shown to perform equally to manual processing methods albeit with a significant improvement in the time taken (approximately 1 min *vs.* 40 min).

The universality of SRS-based AST methods using deuterium labelling is a significant advantage when compared to existing clinical methods. As such, a wide variety of bacterial species can be processed against virtually all antibiotic classes in a rapid analysis timeframe. In addition, the biocompatibility of SRS microscopy enables live cultures to be visualised with minimal phototoxicity observed, whilst the technique is also compatible with clinical sample matrices including whole blood and urine. The development of further automated processing of hyperspectral imaging data are expected to facilitate the clinical translation of the methodologies described.

4.6. Molecular profiling of bacterial biofilms using hsSRS microscopy

Bacterial biofilms pose a significant challenge to both human health and medical devices. There is an urgent requirement for temporal aspects of biofilm development and maturation to provide a fundamental understanding of the underlying mechanisms which govern biofilm formation and response to antibiotic therapy.[132] Currently, it is challenging to study the chemical composition, the penetration depth of novel therapies, the structural components of the biofilm, the molecular interactions of administered drugs or inter-bacterial communications at depth, and within different morphological regions within the biofilm, revealing significant opportunities for further research and investigation.

The application of SRS microscopy to studying bacterial biofilms is emerging. Early progress has been made in the characterisation of bacterial biofilm metabolism and in visualising antibiotic diffusion through this complex biological matrix. Schiessl *et al.* previously used SRS microscopy to map the metabolic activity across *Pseudomonas aeruginosa* biofilm depth.[133] This study represented the first visualisation of the heterogeneous nature of biofilm metabolism using *in situ* SRS metabolic imaging *via* D_2O labelling. As a general technique for studying microbial metabolism in combination with antibiotic treatment, there exists significant potential for this approach in understanding biofilm response to antibiotic therapy. In an alternative strategy, Bae *et al.* developed the companion imaging diagnostic agent, *Van-PEPEA* as a model system to monitor antibiotic diffusion through *Staphlococcus aureus* biofilm (Fig. 8C).[134] First, hyperspectral SRS imaging was used to characterise the biofilm, with multivariate curve resolution analysis used to generate 3D label-free images of bacteria and extracellular polymetric matrix (EPS) components. Next, the authors demonstrated the conjugation of a 2-(4-(phenylethynyl)phenyl)ethan-1-amine (PEPEA) Raman tag onto the antibiotic vancomycin (creating *Van-PEPEA*), which was detected at 2218 cm^{-1} in subsequent SRS imaging experiments. Time-lapse SRS imaging was used to monitor the diffusion and penetration of the Van-PEPEA construct into the biofilm, which was shown to be non-uniform and limited to the upper layer of the biofilm (<15 μm). As such, the authors showed that in the outer layers of the biofilm, the binding and subsequent eradication of bacteria was achieved, whilst the bacteria at deeper regions within the biofilm (>15 μm) remained viable and eventually regrew to the extent of the untreated control sample. This study demonstrated the potential of SRS imaging in tandem with Raman tagging to investigate biofilm therapy which could be used as a method for longitudinal monitoring of biofilm maturation during antibiotic drug development. Together, these studies highlight an emerging application of SRS microscopy for biofilm characterisation, and for monitoring the outcome of antibiotic therapy in the complex environment of a biofilm. With label-free biomolecular detection, SRS microscopy could be applied to the study of mixed population biofilms which better recapitulate those encountered in the clinical environment.

4.7. Antifungal susceptibility testing using hsSRS microscopy

Although antifungal susceptibility testing (AFST) is not as commonplace as antibacterial susceptibility testing, it is becoming increasingly recognised as an important methodology in the management and treatment of fungal infections.[135] The aim of AFST is to reliably produce MIC values that may be used to guide patient therapy, monitor the incidence of antifungal drug resistance and inform epidemiological studies.[136] The application of SRS microscopy for AFST has been gaining traction in recent years. In an early study, the detection of azole resistance in *Candida albicans* was investigated using SRS microscopy and isotope labelling.[137] The authors demonstrated that increased lipid accumulation was a hallmark of fluconazole resistant *C. albicans* through the visualisation of lipid droplets using 2850 cm^{-1} (CH_2 symmetric stretch). To identify the nature of the lipid accumulation, the authors used two isotopically edited probes: glucose-d_7 was used as a metabolic precursor for *de novo* lipid synthesis whilst deuterated oleic acid was used to measure exogeneous fatty acid uptake. In doing so, the origin of lipid accumulation in fluconazole resistant *C. albicans* was identified as *de novo* lipid synthesis. In a related study, the same group identified that the detection limit for glucose-d_7 using SRS microscopy was in the mM range in mammalian cell lines,[138] which was sufficient for the detection of the susceptible and resistant fungal strains *via* quantification of the C–D signal. Unlike traditional molecular techniques, SRS microscopy did not require extraction of metabolites or any *a priori* knowledge of the strain in question. Furthermore, by directly imaging lipogenesis activity, their method was shown to be capable of discriminating between susceptible and resistant strains in 5 h, representing a 5-fold improvement in turnaround time compared to conventional culture-based methods which require around 24–48 h.

A similar approach was adopted by Chen *et al.* who developed a rapid and direct AFST method using D_2O as an alternative deuterium source to probe metabolic flux during antifungal treatment.[139] This method relied upon the incubation of pathogenic fungal species with D_2O and the subsequent detection of deuterated species in the fungal biomass as an indicator of metabolic activity. SRS microscopy was performed on *C. albicans* which was incubated in medium containing 50% D_2O v/v together with the antifungal agents, amphotericin B or fluconazole. The detection of metabolically active fungal cells was demonstrated through the detection of C–D signals at 2168 cm^{-1}. The method was shown to be highly sensitive and specific across different antifungal drug classes: amphotericin B was shown to inhibit fungal cell metabolism, whilst drugs of the azole class were shown to stimulate fungal metabolism (Fig. 8D). These results were consistent with the observation that increased *de novo* lipid synthesis is a hallmark of fluconazole resistant *C. albicans* as identified in the previous study. The method was validated against 14 blood bottle culture samples which were tested against amphotericin B, fluconazole and micafungin to demonstrate the clinical application of the approach. The results were in good agreement with those obtained using the current '*gold standard*' method of broth microdilution.

Recently, Zhang *et al.* demonstrated the potential of fingerprint region hyperspectral SRS imaging as a label-free method of investigating the metabolic reprogramming of azole resistant *C. albicans*.[140] Esterified ergosterol (EE) was identified by the sterol C=C peak at 1603 cm^{-1} and the acyl C=C peak at 1655 cm^{-1} in the SRS imaging, and was shown to be detected in azole-resistant, but not in azole-sensitive, fungal species. The authors also identified that *de novo* lipid synthesis was the driver behind EE accumulation in azole resistant *C. albicans*, which reinforces the observations made in the previous studies that noted increased glycolysis is responsible for fluconazole resistance in *C. albicans*. This report demonstrated the power of hyperspectral SRS imaging for probing lipid metabolism and aberrant esterified ergosterol accumulation in azole-resistant *C. albicans* in a label-free manner. In a related study, the spatiotemporal dynamics of ergosterol synthesis and localisation were visualised in yeast using SRS microscopy.[141] Specifically, isozymes of 3-hydroxy-3-methylglutaryl coenzyme A reductase (HMGR) in engineered strains of *saccharomyces cerevisiae* were shown to promote ergosterol distribution to distinct subcellular locations. The localisation and distribution of ergosterol was detected using SRS microscopy at 2870 cm^{-1} and was shown to be dependent on isozyme expression; HMG1 primarily drives ergosterol distribution to lipid droplets, whilst HMG2 mainly drives ergosterol distribution to the plasma membrane (Fig. 8E). In addition, the HMGR inhibitor, simvastatin was shown to directly reduce yeast cell viability and overall cell size. Dong *et al.* developed polarisation-sensitive SRS microscopy as an alternative approach to investigate antifungal localisation. The authors examined the distribution and orientation of amphotericin B, together with studying lipid storage in single fungal cells.[71] Amphotericin B resulted in a Raman signal at 1556 cm^{-1} indicative of the seven conjugated C=C bonds in its structure, whilst ergosterol was detected at 1602 cm^{-1}, and was shown to redistribute to the membrane upon amphotericin B treatment in *C. albicans*. Using customised parallel-polarised pump and Stokes beams, the authors predicted that the SRS would be maximised when the incident laser fields were polarised along the molecular backbone, and minimised when the laser polarisation was rotated in a perpendicular orientation to it. With the symmetric CH_2 stretching vibration (2850 cm^{-1}) from the acyl chains of phospholipids as a reference, the group showed that amphotericin B molecules are orientated parallel to the acyl chains.

4.8. Rapid hyperspectral SRS microscopy for fungal cell analysis

Technical developments in hyperspectral SRS imaging have also yielded improved methodologies for investigating the temporal aspects of lipid storage and metabolism in single fungal cells. The primary challenges for hyperspectral SRS imaging are the range and resolution of spectral tuning together with the relatively slow wavelength tuning speed of some laser systems. These issues manifest in drifting intensity, focus and alignment of the laser, thereby directly impacting the resulting SRS spectra. Several unique approaches have been taken to address these issues with applications in fungal cell imaging. First, Lin *et al.* developed a sparse sampling SRS imaging platform for hyperspectral visualisation of lipid droplets in live fungal cells.[142] Using random sampling of a small portion of pixels throughout the hyperspectral image stack, the researchers applied a matrix factorisation algorithm to decompose the sub-sampled image stack into spectral signatures and concentration maps corresponding to the nucleus, cytoplasm, lipid droplets and buffer. Consequently, sparse sampling SRS microscopy using a pixel dwell time of 2 μs, enabled the acquisition of 50-frame hyperspectral stack within 0.8 s. Under these conditions, the detection of lipid droplets in live *C. albicans* was achieved, which has been shown to be challenging under slower hyperspectral SRS imaging regimes, where motion artefacts distort the resulting imaging data in live yeast.[143] In an alternative approach, Ni *et al.* developed a fibre-based laser system that enabled rapid tuning of the pump output to access Raman bands across the range 1050–3150 cm^{-1} within 5 ms.[144] In doing so, their system was shown to enable the ratiometric detection of live fungal cell metabolism using a D_2O source. The ratio $I_{C-D}/(I_{C-D} + I_{C-H})$ was used to determine metabolically active *C. albicans* by rapidly switching between the C–D (2150 cm^{-1}) and C–H (2912 cm^{-1}) vibrational modes.

Collectively, these studies demonstrate the feasibility of hyperspectral SRS microscopy for probing the metabolic features that drive antifungal resistance in susceptibility monitoring assays using isotopically edited metabolic precursors. In addition, SRS microscopy has also provided novel insight into lipid localisation and drug accumulation during antifungal treatment. With further development of miniaturised laser sources to perform faster hyperspectral SRS imaging, the clinical translation of these methods can be expected.[137]

5. Visualising drug delivery to skin

Current approaches to assessing transdermal drug delivery and penetration are typically reliant upon excised tissue specimens from animal or human skin. Cutaneous bioavailability studies are routinely performed using adhesive tape stripping, whereby the outermost region of the skin is sequentially removed, and the concentration profile of the administered drug is determined through the tissue depth, typically using chromatography-based techniques.[145] Challenges associated with this approach include poor reproducibility of the skin removal method over time, irregular thickness of SC that is removed at each timepoint, and the tape stripping method is intrinsically low throughput providing no spatial information about the drug penetration route. SRS microscopy is beginning to have real impact in this area because of the minimally invasive nature of its detection, the fact that it can reveal chemically specific information throughout the depth of the skin *in situ*, and the ability to study living models rather than examine excised tissue samples.

SRS microscopy has enabled the label-free imaging of tissue morphology, and the visualisation of drug uptake and distribution in tissue, skin, and nail samples (Fig. 9A and B). Freudiger *et al.* provided an important example of the use of SRS for the study of 3D samples in a label-free manner.[14] The authors visualised neuron bundles within mouse brain samples by the detection of endogenous lipids through imaging at 2845 cm^{-1} and were able to map individual neurons within a thick brain tissue sample using epi SRS detection. SRS imaging of the lipids within a mouse ear sample at depths of 4 μm, 42 μm and 105 μm facilitated the visualisation of the stratum corneum, sebaceous gland, and subcutaneous fat, respectively, in a novel approach for the study of 3D structures (Fig. 9C). Further, the authors were able to monitor the uptake of DMSO, a skin penetration enhancer, and retinoic acid, which is employed as a treatment for acne, within mouse skin samples. Imaging at 670 cm^{-1} enabled the detection of DMSO, which was shown to penetrate the skin through protein channels due to its hydrophilicity. SRS imaging at 1570 cm^{-1} revealed that retinoic acid, a hydrophobic molecule, entered the skin through the lipid rich epidermis. This study demonstrated the suitability of SRS for label-free investigations into tissue structure and morphology, and showed that the technique holds vast potential for the visualisation of drug permeation into skin and other tissues.

Subsequently, SRS has been applied to study the uptake of numerous classes of therapeutic agents into skin. Saar *et al.* used SRS for the video-rate imaging of drug uptake by live subjects through enhancement of traditional SRS setups, which are limited in their ability to investigate rapidly dynamic live systems.[15] Thick tissue samples, in which the majority of input laser light is back-scattered by the sample, hinder the image acquisition time of standard SRS microscopes. To circumvent this, the authors used a custom SRS imaging setup involving a lock-in amplifier with a response time of ~100 ns to improve imaging speeds by three orders of magnitude when compared to conventional SRS methods. The loss in detectable back-scattering was further negated by positioning the photodetector directly in front of the objective lens, which enabled greater volumes of the laser light to be detected. Using this setup, the protein, lipid, and water content within the viable epidermis of live mice was visualised through scanning at 2950 cm^{-1}, 2845 cm^{-1} and 3250 cm^{-1}, respectively. The authors then went on to visualise the uptake of *trans*-retinol (vitamin A) into the skin of live mice. After the prior imaging of proteins and lipids to map the morphology of the stratum corneum, detection of the polyene band of *trans*-retinol at 1596 cm^{-1} allowed for visualisation of the compound. It was observed that the drug penetrated the stratum corneum *via* hair shafts and entered the sebaceous gland. These results contrast with the previous work from the same group, which had been performed on excised tissue, and therefore highlighting the importance of *in vivo* studies for monitoring drug uptake that may be affected by factors such as skin temperature. Finally, through imaging at different depths, the authors visualised the protein content of the stratum corneum, viable epidermis and a hair on the skin surface, within the arm of a human volunteer. After applying DMSO-d_6 to the arm, imaging at 2120 cm^{-1} revealed the pooling of the compound in the area surrounding the hair. The authors successful visualisation of pharmaceutically relevant molecules within the tissues of live samples using SRS, albeit through technological modification, presents the technique as a powerful method for the study of real-time drug uptake in an *in vivo* setting.

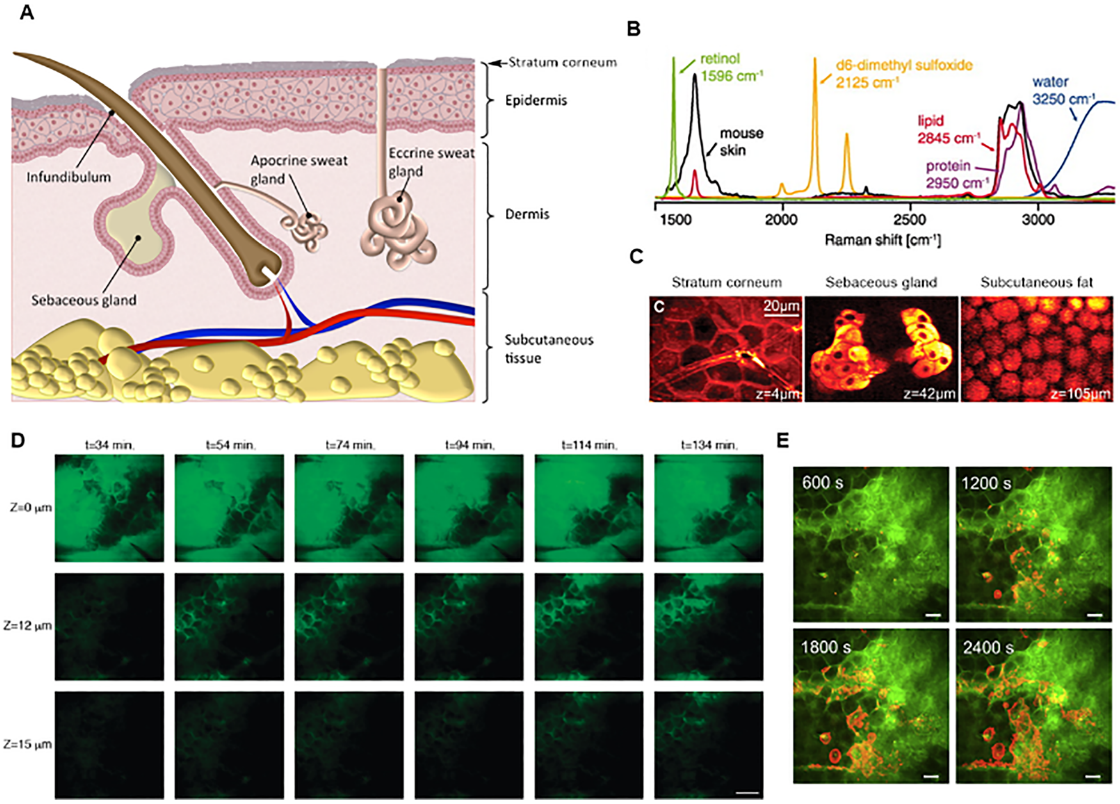

Fig. 9 Visualisation of drug uptake into tissue using SRS. (A) Schematic of skin tissue structure. Image reproduced from ref. 148 with permission from SPIE Digital Library.[148] Copyright 2017. (B) Raman spectrum showing characteristic bands of some of the species visualised in this section. Image reproduced from ref. 15 with permission from American Association for the Advancement of Science (AAAS).[15] Copyright 2010. (C) Visualisation of stratum corneum, sebaceous gland and subcutaneous fat within mouse tissue at depths of 4 μm, 42 μm and 105 μm, respectively, through detection of lipids at 2845 cm^{-1}. Images reproduced from ref. 14 with permission from AAAS.[14] Copyright 2008. (D) Time course study of ketoprofen concentration at different depths within mouse skin tissue at time intervals following treatment with the drug. Ketoprofen imaged at depths indicated down the left-hand side at time intervals indicated along the top. SRS images taken at 1599 cm^{-1}. Images reproduced from ref. 147 with permission from American Chemical Society.[147] Copyright 2011. (E) Visualisation of ruxolitinib uptake at the stratum corneum layer over time. z-Stacked SRS imaging of ruxolitinib (red) and endogenous lipids (green). SRS images taken at 2250 cm^{-1} (ruxolitinib) and 2845 cm^{-1} (lipids). Images reproduced from ref. 149 with permission from Elsevier.[149] Copyright 2021.

The distribution of vitamin E on the surface of mouse skin was demonstrated by Liao *et al.*, who used an enhanced SRS system which exploited spatial frequency multiplexing and single photodiode detection to enhance photon collection efficiency.[146] The authors used a narrow-band Stokes beam, a spectrally dispersed broadband pump beam and a large-area detector to generate SRS spectra. Their setup enabled the visualisation of vitamin E, olive oil and bovine serum albumin at depths of 20 μm and 50 μm within mouse skin in a multiplex manner.

In another study, Saar *et al.* used SRS to monitor the topical application of ketoprofen, and deuterated analogues of ibuprofen and propylene glycol (PG), which is a commonly employed pharmaceutical excipient.[147] A solution of ketoprofen in deuterated PG was applied to the surface of excised mice ears and diffusion of the compounds across the stratum corneum was monitored. Imaging at 2120 cm^{-1} enabled detection of deuterated PG, whilst imaging at 1599 cm^{-1} allowed for the detection of the strong aromatic bond stretch of ketoprofen. The authors monitored the diffusion of the two compounds at regular time intervals at depths of 12 μm and 15 μm and saw an increase in signal at these depths in both channels across the course of the experiment (Fig. 9D). Integration of the total signal of each of the two compounds as a function of depth enabled the generation of concentration profiles for deuterated PG and ketoprofen relative to their concentrations at the surface. The diffusion of deuterated PG into the stratum corneum was found to be faster than that of ketoprofen, as expected, and demonstrated the use of SRS to study the dynamics of API uptake, as well as excipients that may be present in their formulations. Finally, mouse skin samples were treated with a close to saturated solution of deuterated ibuprofen in non-deuterated PG. Shortly after application, the formation of drug crystals on the skin surface was observed. The authors postulated that this was due to the drug concentration in solution reaching saturation point because of the rapid diffusion of PG into the skin or the evaporation of solvent.

These findings were later built on by Belsey *et al.* who imaged the uptake of ketoprofen in a solution of deuterated PG into porcine skin.[150] A linear dependence of observed SRS signal intensity on concentration facilitated the semi-quantitative assessment of the levels of ketoprofen detected at 1599 cm^{-1} (aromatic ring C–C stretch) and deuterated PG at 2120 cm^{-1} (CD_2 stretch) present at different depths within the skin sample. Both compounds were seen to permeate at slower rates than in mouse skin, as was expected due to the thicker layer of corneocytes present.

Wei *et al.* used SRS to visualise the uptake of terbinafine hydrochloride, an antifungal skin treatment that possesses an intrinsic alkyne bond, by mouse ear tissue in a label-free manner.[151] Lipid imaging at different depths allowed mapping of the stratum corneum, viable epidermis and sebaceous gland within the tissue, whilst scanning at 2230 cm^{-1} revealed the distribution of the drug at each of these subdermal levels. It was observed that the compound was present primarily in lipid-rich channels, suggesting that the drug penetrated tissue *via* the lipid phase rather than through protein carriers, showing the power of SRS for investigating the mechanism of drug uptake into tissue samples.

The use of SRS for studying the distribution of antifungal agents within tissues was demonstrated by Garrett *et al.*, who sought to visualise the distribution of two APIs within a topical dandruff treatment in porcine skin and to compare their permeation.[148] The uptake of climbazole (CBZ), an imidazole containing antifungal agent, and zinc pyrithione (ZnPT), a pyridine containing inhibitor of fungal cell division, were visualised using SRS. The imidazole ring vibration of CBZ was detected through imaging at 1580 cm^{-1} whilst the C═N pyridine stretch of ZnPT was detected at 1540 cm^{-1}. Porcine skin was treated with a formulation containing both APIs, which showed that ZnPT predominantly formed microcrystals on the surface of the skin, whereas CBZ accumulated in lipid-rich crevasses on the surface. Further, the authors used SRS to compare the depth of permeation of the two compounds. Through detection of CBZ and ZnPT at different depths from the pig skin surface, they observed that CBZ penetrates to depths of 50–60 μM, whilst ZnPT penetrates to depths of only 10–20 μM. To that end, this study revealed novel insight into the biodistribution profile of these drugs in skin.

In addition to studying drug uptake by skin, SRS has also been applied to investigate the permeation of drugs through human nails. Chiu *et al.* visualised the diffusion of a lipophilic drug mimic, octyl methoxycinnamate (OMC), into human nail samples in a label-free manner using SRS.[152] Nail samples were first porated using a titanium needled derma roller and then treated with polymeric nanoparticles (NPs) functionalised with a fluorescent probe, Nile Red, and loaded with OMC. Multi-modal two photon fluorescence (TPF) and SRS imaging enabled the visualisation of the Nile Red fluorophore affixed to the NPs, and the diffusion of OMC into the nail following delivery using the NPs. SRS imaging at 1600 cm^{-1} enabled detection of the aromatic C═C stetch of OMC within the nail at intervals of 4 μM ranging from 0 μM to 32 μM. The authors found that after 3 h, the SRS signal of OMC correlated almost exactly to the TPF signal of the Nile Red-tagged nanoparticles, indicating little diffusion of the drug from the NP carriers. However, after 7 days, it was observed that OMC had diffused into the nail away from the nanoparticles, demonstrating the applicability of SRS to study the kinetics of drug diffusion into nail.

Whilst SRS has been applied extensively for visualising the permeation of drugs into tissue samples, the technique has also been used to assess phenotypic outcomes of drug treatment within 3D structures. Lu *et al.* sought to visualise drug-induced changes to the cell cycle within tissue in a label-free manner using SRS microscopy.[153] To do so, they treated mouse skin with 12-*O*-tetradecanoylphorbol (TPA), a tumour promoter that is known to induce epidermal hyperplasia through increasing the mitotic rate of cells. The authors imaged the DNA of cells by scanning at 2956 cm^{-1} and this channel was used to determine the phase of the cell cycle. An increased number of mitotic cells were observed following treatment with TPA when compared to an untreated control, as determined by an increased DNA signal. With SRS being a powerful tool for both 3D imaging and the visualisation of endogenous DNA, protein and lipid content in a label-free manner, the technique holds great promise for the assessment of phenotypic outcomes in tissue following drug treatment.

SRS has also found application in the determination of pharmacokinetic properties of drugs within 3D samples. Feizpour *et al.* used SRS and a deep learning approach to assess the pharmacokinetic properties of ruxolitinib.[149] Convolutional neural networks (CNNs) were first trained to identify hydrophilic and hydrophobic regions of the skin, and samples were then imaged following treatment with ruxolitinib in transcutol, a solvent with structural similarities to polyethylene glycol (PEG). The drug was found to localise within the lipid-rich junctions between the corneocytes found in the stratum corneum, as determined by the CNNs. Further the authors visualised the gradual accumulation of the drug within the SC layer over a one-hour period using the Raman band at 2250 cm^{-1} (C≡N stretch) (Fig. 9E). The effect of stratum corneum disruption on the pharmacokinetics of ruxolitinib was also investigated. Separate formulations of the drug in transcutol and a low pH gel were applied to mouse skin, and the penetration of the drug were compared. The gel formulation was seen to cause major alterations to the skin morphology, and this was reflected in a fast permeation rate into the skin tissue, demonstrating the ability of SRS to delineate the dependency of drug uptake by tissue on the drug-vehicle formulation used.

Although conventional SRS methods allow for the successful detection of drug molecules from within tissue, technological enhancement of SRS setups can facilitate faster image acquisition times and more sensitive detection of analytes. Ito *et al.* used phase-modulated SRS (PM-SRS) to decrease the background SRS signal arising from tissues.[154] In PM-SRS, the background signal is removed through phase modulation and time-resolved detection, which resulted in enhanced signal contrast when compared to conventional amplitude-modulated SRS (AM-SRS). The authors used PM-SRS to detect a variety of topical skin agents in an *in vitro* skin model. First, the effectiveness of PM-SRS was demonstrated by visualising ectoine, a skin moisturising agent, within tissue using both

PM-SRS and AM-SRS. A 10% ectoine solution was applied to skin tissue and was visualised as XZ depth images using both imaging techniques. PM-SRS provided a signal contrast 40 times higher than conventional AM-SRS and showed the preferential properties of the enhanced imaging technique. Next, the authors assessed the permeation of lidocaine hydrochloride (LID), an anaesthetic, and loxoprofen sodium (LOX), a non-steroidal anti-inflammatory drug. Tissue samples were treated separately with solutions of LID and LOX followed by PM-SRS imaging at 1092 cm^{-1} and 1184 cm^{-1}. Concentration depth profiles of the two drugs within the tissue showed that LOX was better able to permeate through the stratum corneum layer.

Pence *et al*. utilised multi-window sparse spectral sampling SRS (S^4RS) for imaging a drug and excipient within mouse ear skin.[155] S^4RS involves a tuneable dual-output optical parametric oscillator which facilitates the rapid tuning of SRS lasers between different Raman vibrational windows.[154] This allows the rapid generation of Raman spectra for the detection of preselected target frequencies. The authors used S^4RS to visualise the uptake of tazarotene (Taz), a retinoid drug used to treat psoriasis, into mouse ear skin. A solution of Taz in PEG was applied to *ex vivo* mouse ear skin and S^4RS enabled rapid imaging of the drug at 1592 cm^{-1} and PEG200 at 1470–1480 cm^{-1}. The subsequent generation of depth-encoded sum intensity projections revealed that Taz primarily remained in the stratum corneum and did not penetrate the skin to access deeper tissues, whilst PEG penetrates quickly into the sebaceous glands.

Finally, Kuzma *et al*. developed a microfluidic applicator for coupling to a microscope and optic laser setup that enabled the rapid determination of drug pharmacokinetics on mouse ear skin samples at early time points following drug treatment.[156] The authors trialled numerous iterations of drug applicator, before reaching a design that allowed for the controlled delivery of an API formulation to a skin surface, which could be imaged using coherent Raman imaging. To demonstrate the ability of the applicator for the assessment of drug permeation, samples were treated with solutions of ruxolitinib in the permeation enhancers PG and diethylene glycol monoethyl ether (DGME) and then imaged using S^4RS. The applicator enabled the generation of concentration-time profiles of the drug in tissue following treatment with each formulation, and it holds vast potential for monitoring the permeation of APIs into tissue immediately following drug treatment.

In addition to the visualisation of uptake of therapeutic agents, SRS has been extensively applied to the study of the morphology of tissue samples and the permeation of other pharmaceutically relevant molecules, such as solvents and excipients. The characteristic Raman bands associated with endogenous proteins and lipids at around 2930 cm^{-1} and 2850 cm^{-1} have facilitated the reliable and accurate imaging of the morphology of *ex vivo* skin samples.[157–162] Moreover, the permeation of water, DMSO, PG and glucose, or their deuterated analogues, into skin or nail samples has been achieved through detection of Raman bands associated with each compound.[163–166]

In summary, SRS has been used extensively for the investigation of transdermal drug uptake. The ability to reliably quantify analytes at different permeation depths, in a label-free manner, presents the technique as a powerful analytical tool for the study of drug pharmacokinetics in skin. Further, advanced Raman methods, such as S^4RS, enable faster acquisition times and enhanced sensitivity demonstrating the power and potential of SRS microscopy technologies.

6. Pharmaceutical formulation analysis using Raman and SRS microscopy

Whilst the focus of this review is on the development of SRS microscopy application in the drug discovery landscape, at this point it is important to highlight the contribution of spontaneous Raman scattering in the analysis of pharmaceutical dosage forms to contextualise the advances that SRS imaging has brought to this area. Spontaneous Raman spectroscopy has found extensive use within the field of formulation analysis. The technique has been applied to visualising the spatial distribution of tablet components,[167] the quantification of APIs,[168] and the kinetics of salt disproportionation reactions that occur within tablet formulations.[169] More recently, SRS has been applied to the high-resolution visualisation of components,[170] the assessment of polymorph distribution,[171] and monitoring of drug release from implant formulations.[172]

Slipchenko *et al*. first used SRS for the imaging of APIs within formulations when they visualised amlodipine besylate (AB), a hypertension treatment, and various excipients within tablets.[170] SRS facilitated the high resolution visualisation of the API through the detection of the C=C stretching band of the drug at 1650 cm^{-1}, whilst the detection of the P–O stretching band of an excipient, dibasic calcium phosphate anhydrous (DCPA), was possible at 985 cm^{-1}. To image the other excipients: microcrystalline cellulose (MCC), sodium starch glycolate (SSG) and magnesium stearate (MgSt), SRS images were taken at 2930 cm^{-1} and 2850 cm^{-1} and deconvoluted to account for the intrinsic Raman intensities of each analyte. Using this approach, the authors were able to observe the API and each excipient within a tablet manufactured by Pfizer. Further, through SRS mapping of the API and excipients within tablets from Apotex, Greenstone, Ethex, TEVA and Upsher-Smith, the authors were able to compare the different chemical compositions and component particle sizes present (Fig. 10A). The ability of SRS to map the components of the tablets was compared to confocal spontaneous Raman spectroscopy and coherent anti-Stokes Raman scattering (CARS), where it was observed that SRS was superior to spontaneous Raman approaches in terms of spatial resolution and image acquisition times but had a diminished signal-to-noise ratio when compared to CARS. However, the CARS imaging of the tablets was hindered by autofluorescence of the formulation components, revealing SRS to be a useful alternative technique for the study of drug formulations.

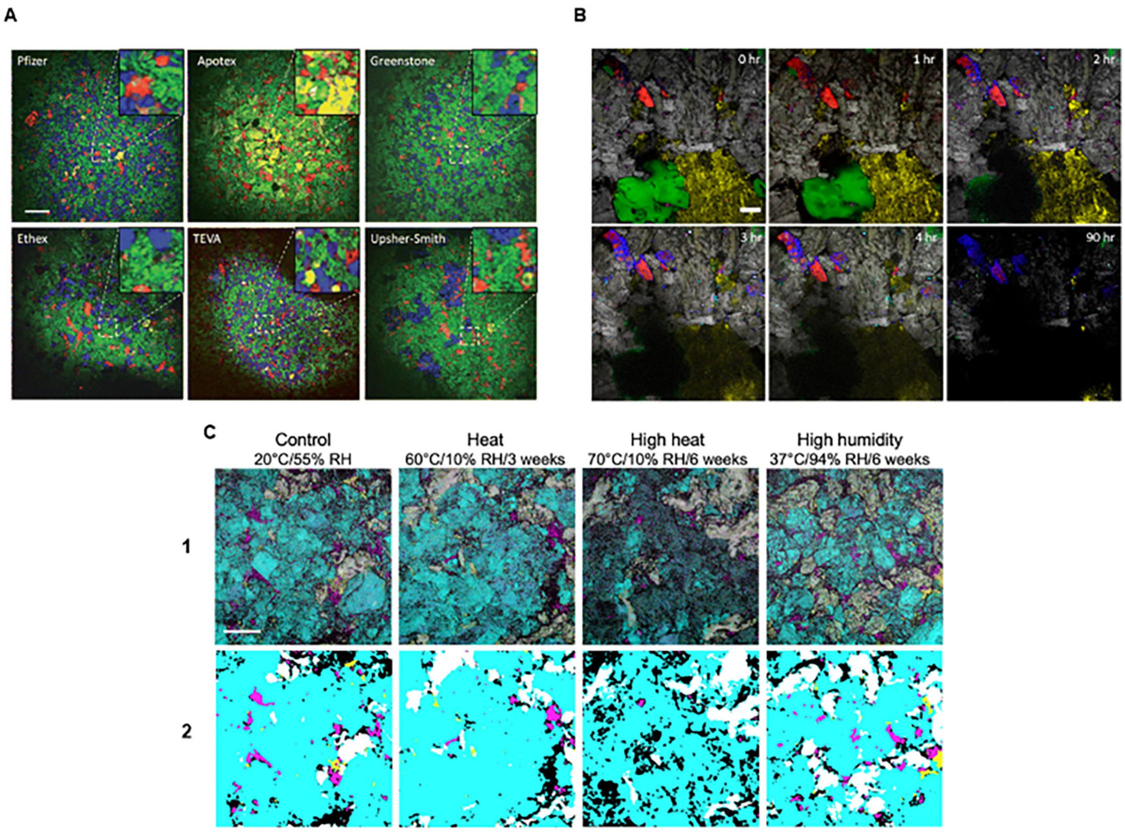

Fig. 10 Examples of drug formulation surface analysis using SRS. (A) SRS visualisation of the components of AB tablet formulations. AB, DCPA, MCC, SSG, MgSt displayed as red, blue, green, yellow, and magenta, respectively. In the Apotex formulation, yellow represents lactose. Images reproduced from ref. 170 with permission from Royal Society of Chemistry.[170] Copyright 2010. (B) SRS time course study of PIO-HCl tablet aging. PIO-HCl, PIO-FB, MgSt, stearic acid, crospovidone, mannitol, and Avicel displayed as red, blue, magenta, cyan, green, yellow, and grey, respectively. Images reproduced from ref. 173 with permission from American Chemical Society.[173] Copyright 2019. (C) S^{4}RS imaging of tablet composition following different storage conditions. Row 1: S^{4}RS composite abundance maps. Row 2: Thresholding images. Naproxen, lactose, HPMC and MgSt displayed as magenta, cyan, white and yellow, respectively. Images reproduced from ref. 174 with permission from Royal Society of Chemistry.[174] Copyright 2024.

Since the pioneering use of SRS for imaging tablet components by Slipchenko *et al.*, the technique has been applied to studying numerous aspects of formulations. Francis *et al.* sought to visualise the release of APIs from localised implant drug delivery systems (DDS) using SRS.[172] DDS are a powerful method of formulation that enable the controlled release of a therapeutic dosage of drug molecules at the target site, reducing off-target side effects linked to the systemic application of drugs. In DDS, drug molecules are typically delivered in a biodegradable matrix, such as poly(D,L-lactic acid) (PDLLA), which is hydrolysed over time at the target site to release the API. The authors first visualised entecavir, an antiviral agent, suspended in a PDLLA matrix using SRS. The drug and matrix were imaged within implant formulations of 20% and 60% drug loading through scanning a longitudinal cross section at 1582 cm^{-1} and 1770 cm^{-1}, respectively. It was observed that the drug was distributed heterogeneously in small pockets through the cross section in both loadings. The high resolution of SRS enabled the assessment of the API particle size distribution, which revealed that in both formulations at least 75% of the API particles were below 10 μm^2 in area. Further, after visualising the drug within the formulation, the authors sought to investigate the dissolution of the API from the matrix upon the implant entering solution. Entecavir dissolution was visualised using a custom-made flow cell, in which warm (40 °C) deionised water was flowed over a cross section of 20% drug loading implant formulation and imaged *in situ* using SRS. Particle dissolution was quantified by monitoring the volume of entecavir particles within the field of view at numerous timepoints during the experiment, which correlated well with an analogous study performed using UV/vis spectroscopy. As the rate of API dissolution represents an important factor on the overall bioavailability of drug molecules, the ability to monitor the dissolution in real-time in high resolution makes SRS a powerful methodology for assessing biologically relevant properties of different formulation types.

The disproportionation of the salt form of APIs to their uncharged state, through interaction with acidic or basic excipients within a formulation, is a major consideration for the pharmaceutical industry.[175] Neutral free base (or acid) drugs are typically less soluble than their charged analogues, possess reduced bioavailability, and have a lower degree of chemical stability. Therefore, the investigation of the mechanism of the disproportionation reactions occurring within formulations is vital to the successful delivery and absorption of drug molecules. Building on the findings of Nie *et al.*,[169] Figueroa *et al.* applied SRS to the visualisation of the disproportionation of pioglitazone hydrochloride (PIO-HCl) to its free base (PIO-FB) within a drug formulation.[173] Detection of the Raman peaks at 1640 cm^{-1} and 1610 cm^{-1} enabled the visualisation of PIO-HCl and PIO-FB, respectively, within a mixture of the two forms of the drug. The authors then sought to investigate the effects of stressing conditions (40 °C, 75% relative humidity) on the extent of salt disproportionation occurring within a tablet. Tablets of 1% DL were exposed to standard storage conditions and stressed storage conditions then imaged using SRS. In tablets stored under normal conditions, less than 10% of PIO-HCl underwent disproportionation, whereas, for tablets exposed to stressed conditions, over 20% of the drug was converted to the free base. As such, a timelapse study over a period of 90 hours enabled the visualisation of the gradual conversion of PIO-HCl to PIO-FB (Fig. 10B). To probe the mechanism of the reaction, the authors visualised a deuterated analogue of one of the excipients within the formulation, magnesium stearate (d-MgSt). MgSt was postulated to act as a proton acceptor and facilitate the disproportionation of PIO-HCl to afford the free base of the drug, stearic acid and $MgCl_2$. However, it was observed that under the stressed storage conditions, the conversion of PIO-HCl to PIO-FB occurred in a heterogenic manner across the tablet, independent of stearic acid-*d* distribution. The authors observed that the reaction proceeded in areas that also possessed a water signal (3400 cm^{-1}), indicating that water may act as a medium for the proton exchange, rather than the process occurring through direct contact of solid PIO-HCl and MgSt as previously thought. With salt disproportionation posing a major issue in formulation development, the ability to investigate the mechanism of such reactions renders SRS a useful technique that may inform the development of strategies to prolong formulation stability.

Solid compounds of the same ionisation state can exist as a number of polymorphs with different packing or conformational properties. These polymorphs may exhibit different physiochemical properties, such as solubility, bioavailability, and thermodynamic stability, and therefore the assessment of polymorph distribution within tablet formulations is important for assessing therapeutic behaviour. Sarri *et al.* used SRS to assess the polymorph distribution of two APIs present within tablets.[171] Clopidogrel is known to exist as one of two polymorphs, A-F1 and A-F2, which possess unique Raman spectral profiles, and the authors detected SRS signals at 3098 cm^{-1} and 3109 cm^{-1} in compact tablets to visualise A-F1 and A-F2, respectively. SRS imaging revealed the distribution of the API as large A-F1 crystal patches distributed within areas of A-F2 granules. Further, the authors used hyperspectral SRS imaging and a decision tree algorithm to visualise the distribution of both clopidogrel polymorphs and the excipients present within a tablet formulation. Through selection of appropriate imaging wavenumbers, the decision tree algorithm reliably assigned each pixel within a field of view to a specific tablet component. The authors were able to observe the presence of A-F1, A-F2, starch, mannitol and PEG6000 within their formulation. The relative abundance of each excipient as determined by SRS and the decision tree algorithm agreed well with the expected ratios. Using a similar approach with revised wavenumbers for SRS imaging, the authors were able to apply the decision tree algorithm to the visualisation of two polymorphs of amibegron and various excipients within a formulation. Once again, the relative abundance of each component as determined by SRS agreed well with the expected values.

Finally, Wei *et al.* used SRS for the quantitative analysis of tablet aging and define its effect on the components of naproxen tablets.[174] In order to visualise naproxen and various excipients within a tablet formulation, the authors employed S^4RS which enabled the rapid epi-detection of SRS signals from distinct wavenumber regions. Before imaging the effect of aging on tablet composition, it was necessary to identify spectroscopic markers for the visualisation of naproxen and three excipients: lactose monohydrate, hydroxypropyl methyl cellulose (HMPC) and MgSt. With the selection of 20 distinct Raman bands that would facilitate the detection of the API and the three excipients, the authors applied S^4RS to the imaging of each component within a tablet formulation. Non-negative least squares (NNLS) spectral unmixing of the resultant data enabled the generation of a composite abundance map which underwent thresholding to reveal the distribution of the API and excipients within a naproxen tablet cross section. Next, the authors sought to assess the effect of aging conditions on tablet integrity. Naproxen tablets were subject to four different storage conditions (Fig. 10C): control, heat, high heat and high humidity. Under high humidity conditions, the tablets possessed increased surface area contributions from naproxen and HMPC, owing to the physical instability of the formulation under these conditions. After storage under high heat, the authors observed a negligible MgSt surface area contribution which was postulated to be due to the chemical degradation of MgSt at 70 °C. Further, a cross section of tablets stored under high heat conditions revealed the heterogenic degradation of lactose, which occurred primarily on the peripheries of the formulation, despite pure lactose powder being stable under the same conditions. Within the formulation, areas of decreased lactose signal correlated well with areas of decreased MgSt signal, suggesting the consumption of MgSt during a reaction that results in the degradation of lactose. The data gathered during this study demonstrated the power of SRS for the high-resolution monitoring of the compositional makeup of formulations after exposure to different storage conditions. This may inform subsequent formulation design or provide insight into optimal storage conditions for drug tablet formulations.

7. Summary and future perspectives

In the fifteen years since the first demonstration of SRS imaging in cellular samples, the technique has developed rapidly to enable a wide variety of imaging applications pertinent to drug discovery. When considering the need for innovative methods to study drug-cell interactions to characterise the biological activity of new chemical entities from a therapeutic perspective, the label-free imaging capability and high-content data acquired using hyperspectral SRS imaging are key features of the technique that have driven its uptake. As the era of precision therapeutics edges closer, the need for clear understanding of drug-cell interactions at the cellular and molecular level becomes increasingly important. Considering the sheer breadth of studies outlined within this review, we have created a summary of the molecules, vibrational assignments and application in SRS imaging that have been covered throughout as a summary (Table 1).

In this review we have highlighted the technical advances that have been realised in the realm of SRS imaging for biological applications, with relevance to drug discovery. We have given much focus to the chemometric methods which have been developed to understand and interpret hyperspectral SRS imaging data. We foresee a bright future for these techniques in the rapid identification of key spectral features of disease, and potentially towards identifying markers of successful treatment and therapy. In particular, hyperspectral SRS imaging has been demonstrated for the imaging of several drugs and small molecules to reveal their intracellular distribution. Whilst selected drugs have inherent alkyne and nitrile functionalities that can be used as spectroscopic markers to enable drug localisation studies in the cell-silent region, the vast majority of approved therapeutics do not contain these groups. Aside from labelling techniques to incorporate a small Raman-active tag, the use of hyperspectral SRS imaging has been put to good effect when visualising tyrosine kinase inhibitors based on the fingerprint Raman spectrum. Current limitations on the detection sensitivity of SRS imaging are typically in the mM region and therefore, precise localisation and identification of mechanism of action remains a challenge for molecules which are not significantly enriched within the cell. The development of greater detection sensitivity when applied to hyperspectral SRS imaging is clearly required to push this limit. Furthermore, the use of refined and sophisticated machine learning techniques to identify spectral features with poor signal-to-noise may also be of benefit to addressing this challenge. It is clear SRS imaging has played an important role in visualising single-cell drug response which has the potential for detailed studies of drug resistance and understanding mechanism of action.

Isotopic labelling has also played a significant role in multiplex SRS imaging, especially when considering the impact of cellular metabolism in response to treatment. As outlined here, a variety of methods have been developed to specifically label lipid, protein and nucleic acids using metabolically incorporated precursors. In doing so, an iterative approach to measuring the impact of drug treatment upon these important biomolecular classes has been achieved. The creation of new precursors to target specific molecular pathways could facilitate the development of image-guided therapeutic targeting. In addition, the application of isotopic labelling has played an important role in the rapid analysis of antimicrobial susceptibility testing. The clear advantage of SRS imaging approaches in this area is that the detection of successful antimicrobial susceptibility can be achieved in a single growth cycle which drastically improves sample throughput when compared to conventional culture-based methods. In turn, imaging-based methods such as those reviewed here could have a transformative impact in combatting AMR under time-critical scenarios.

A unifying theme throughout the review is the application of hyperspectral SRS imaging for understanding drug and cellular metabolism, localisation and distribution. With the development of commercial SRS imaging systems, the technique is beginning to show use in imaging in complex biological models and across scales. For example, several key studies have demonstrated drug imaging in spheroid models which are beginning to address fundamental questions around drug penetration and localisation. Since the first reports of biological SRS imaging, the application of the technique has been consistently applied to studying dermal architecture and drug penetration. During this period, multiple groups have demonstrated the visualisation of dermal formulations and topically applied drugs into the complex skin architecture. Furthermore, SRS has been applied to imaging across a variety of biological models form *ex vivo* tissues, to intraoperative detection, to animal models. With improved spectral resolution and biocompatible optical components for imaging in complex organisms, the technique has a bright future for revealing key features of disease in a native environment. In recent years, the development of imaging setups compatible with cell culture medium and live animal studies have been developed. Further refinement of these techniques is likely to focus on improving the stability of imaging over extended periods for longitudinal imaging of drug activity in the target organism. Whilst endoscopic systems for SRS imaging have been reported,[176,177] the technology developed in these instances could find potential for imaging drug uptake and biodistribution in a live animal model. This ambitious target has yet to be fully realised, but it holds significant potential to understanding drug activity in a holistic manner.

Although the focus of this review is on the application of label-free SRS imaging, a variety of colour palettes have been developed for highly multiplexed SRS imaging. The integration of metabolic precursors based on SRS palettes, including MARS[178,179] and Carbow,[18] could ameliorate the information garnered from a single imaging experiment. Very recently, the development of ratiometric, activity-based sensing has been demonstrated for imaging labile copper pools in live cells using epr-SRS.[180] The expansion of Raman sensors for biological species is also likely to be an area of important development with potential impact for the identification of druggable targets through a combined imaging and proteomics approach. Furthermore, the development of super-resolution SRS imaging is also beginning to shed new insight on the structure-function relation of biological networks. As an example, SRS microscopy could be used to better understand druggable targets and identify drugs that reach their intended intracellular target,

Table 1 A summary of the first applications of SRS microscopy for the compounds provided in this review

Compound	Vibration used for SRS imaging (cm^{-1})	First application	Ref.
Imatinib (**1**)	1305 (C–C stretching)	Intracellular localisation detected at 1305 cm^{-1} in BAF/BCR-ABL1 cells	66
Nilotinib (**2**)	1305 (C–C stretching)	Intracellular localisation detected at 1305 cm^{-1} in BAF/BCR-ABL1 cells	66
Lapatinib (**3**)	1368	Lysosomal accumulation detected at 1368 cm^{-1} in A549 cells	67 and 68
Afatinib (**4**)	1390	Lysosomal accumulation detected at 1390 cm^{-1} in A549 cells	67
Amphoterocin B (AmB, **5**)	1556 (C═C)	Intracellular localisation detected at 1556 cm^{-1} in *candida albicans*.	71
Ponatinib (**6**)	2221 (C≡C)	Intracellular localisation detected at 2221 cm^{-1} in KCL22 cells	69
7RH (**7**)	2217 (C≡C)	Intracellular localisation detected at 2217 cm^{-1} in MCF-7 cells	70
Ethinylestradiol (EE2, **8**)	2093 (C≡C)	Detection in a cetyltrimethylammonium bromide (CTAB)-coated gold nanorod suspension at 2093 cm^{-1}	74
Disodium BSH cholesterol (**9**)	2505 (B–H)	Intracellular localisation detected at 2505 cm^{-1} in HeLa cells	76
Propofol-d_{17} (**14**)	2055 (C–D)	Intracellular localisation in hippocampal neurons	77
BADY-ANS (**15**)	2219 (C≡C)	Alkyne-tagged derivative of anisomycin used to determine intracellular localisation in SK-Br-3 cells	78
Ferrostatin (**16**)	2262 (C≡C)	Alkyne-tagged ferrostatin-1 analogue used to determine intracellular localisation in HT-1080 cells	79
PhDY-Ant (**17**)	2251 (C≡C)	Alkyne-tagged antimycin analogue used to determine intracellular localisation in HeLa cells	80
Diyne-girder stapled p53 peptide	2255 (C≡C)	Bis-alkyne stapled p53 peptidomimetic visualised in live ES-2 cells	84
S-MGB-528 (**18**)	2106 (C≡C, terminal)	Visualisation of minor groove binders in live HeLa cells	81
JQ1-MDPY (**19**)	2223 (C≡C)	Alkyne-tagged JQ1 (BET inhibitor) analogues used for intracellular visualisation in live HeLa cells	82
Van-PEPEA	2218 (C≡C)	Alkyne-tagged vancomycin analogue visualised in *S. aureus* biofilm	134
Trans-retinol (vitamin A)	1596 (C═C polyene stretching)	Label-free visualisation of *trans*-retinol on the skin of live mice	15
DMSO-d$_6$	2120 (C–D)	Topical application of DMSO-d6 and visualisation of this solvent into skin	15
Vitamin E	2800–3000 (C–H)	SRS imaging in mouse skin and localisation based on MCR analysis	146
Propylene glycol-d$_8$	2120 (C–D)	Imaging the penetration of deuterated PG and ketoprofen across the stratum corneum	147 and 150
Ketoprofen	1599 (C–H, aromatic)		
Terbinafine hydrochloride	2230 (C≡C)	Label-free imaging of drug distribution through skin	151
Climbazole (CBZ)	1580 (imidazole ring vibration)	Visualisation of antifungal agents in porcine skin following topical application	148
Zinc pyrithione (ZnPT)	1540 (C═N)		
Octyl methoxycinnamate (OMC)	1600 (C–C aromatic)	Visualising the diffusion of OMC into human nail samples	152
Ruxolitinib	2250 (C≡N)	Visualisation of drug penetration into skin	149
		Concentration-time profiles drug formulations measured in mouse skin following microfluidic drug delivery	156
Ectoine	848 (C–COO^{-})	Label-free skin penetration measurement of topically applied drugs	154
Lidocaine hydrochloride	1092 (methyl rock, CH$_2$ twist)		
Loxoprofen sodium	1184 (C–C stretching)		
Tazarotene	1592 (C═C)	S^{4}RS image of nude mouse ear skin following topical application of API solution	155
Amlodipine besylate	1650 (C–C stretch)	SRS images of API together with excipients within tablets	170
Entecavir	1582 (C═C)	Visualising the spatial distribution of the drug in a sustained release implant formulation (polymer matrix)	172
Pioglitazone•HCl	1640 (pyridine ring mode)	Visualising disproportionation reactions in formulated tablets under normal and stressed storage conditions	173
Pioglitazone free base	1610 (pyridine ring mode)		
Clopidogrel	3098 3109	Visualising polymorphic forms of the drug in formulated tablets	171
Naproxen	1394 (CH$_3$ symmetric deformation)	Visualising drug content in tablet formulations under different storage conditions	174

stimulating research into how drugs can be modified to enhance drug-target engagement and therapeutic activity. In addition to the development of multiplex imaging with molecular reporters, SRS imaging has also been integrated with complementary techniques including fluorescence and photothermal imaging. Hybrid imaging techniques such as those described in this review offer high-content imaging for detailed assessment of drug-cell interactions, including those combining mass spectrometry and fluorescence microscopy with SRS imaging.

The launch of commercially available SRS imaging systems is beginning to support the adoption of the technique in non-specialist laboratories and in adjacent fields. In doing so, the diversity of applications of SRS is ever expanding, and with it, the standardisation of the technique will likely follow. At present, the calibration, acquisition and reporting standards for SRS imaging data are variable, which may restrict the reproducibility of results from lab-to-lab. We anticipate further developments in the standardisation of the technique towards a unified reporting standard for SRS imaging, particularly in the development of signal quantification. From the advances outlined in this review, significant developments in SRS imaging have been realised which are facilitating the routine adoption of the technique in biological and pharmaceutical imaging applications.

Author contributions

HJB: conceptualisation; writing – original draft; writing – review and editing; visualisation. WJT: conceptualisation; writing – original draft; writing – review and editing; visualisation. EKG: funding acquisition. NCOT: conceptualisation; project administration; writing – review and editing. KF: conceptualisation; project administration; writing – review and editing. DG: conceptualisation; project administration; writing – original draft. Visualisation; funding acquisition. Supervision. HJB and WJT contributed equally to this work.

Conflicts of interest

The authors declare no conflicts of interest.

Data availability

No primary research results, software or code have been included, and no new data were generated or analysed as part of this review.

Acknowledgements

We thank the University of Strathclyde, the EPSRC (EP/TR512114/1; EP/V519777/1), and GlaxoSmithKline for financial support.

References

1 M. J. Waring, J. Arrowsmith, A. R. Leach, P. D. Leeson, S. Mandrell, R. M. Owen, G. Pairaudeau, W. D. Pennie, S. D. Pickett and J. Wang, *et al.*, An analysis of the attrition of drug candidates from four major pharmaceutical companies, *Nat. Rev. Drug Discov.*, 2015, **14**, 475.

2 V. Jentzsch, L. Osipenko, J. W. Scannell and J. A. Hickman, Costs and Causes of Oncology Drug Attrition With the Example of Insulin-Like Growth Factor-1 Receptor Inhibitors, *JAMA Netw. Open*, 2023, **6**, e2324977.

3 I. Kola and J. Landis, Can the pharmaceutical industry reduce attrition rates?, *Nat. Rev. Drug Discov.*, 2004, **3**(8), 711.

4 J. Arrowsmith and P. Miller, Phase II and Phase III attrition rates 2011–2012, *Nat. Rev. Drug Discov.*, 2013, **12**(8), 569.

5 A. Honkala, S. V. Malhotra, S. Kummar and M. R. Junttila, Harnessing the predictive power of preclinical models for oncology drug development, *Nat. Rev. Drug Discov.*, 2022, **21**(2), 99.

6 Z. Zhao, X. Chen, A. M. Dowbaj, A. Sljukic, K. Bratlie, L. Lin, E. L. S. Fong, G. M. Balachander, Z. Chen and A. Soragni, *et al.*, Organoids, *Nat. Rev. Methods Primers*, 2022, **2**(1), 94.

7 N. Carragher, F. Piccinini, A. Tesei, O. J. T. Jr, M. Bickle and P. Horvath, Concerns, challenges and promises of high-content analysis of 3D cellular models, *Nat. Rev. Drug Discov.*, 2018, **17**(8), 606.

8 J. R. W. Conway, N. O. Carragher and P. Timpson, Developments in preclinical cancer imaging: innovating the discovery of therapeutics, *Nat. Rev. Cancer*, 2014, **14**(5), 314.

9 S. N. Chandrasekaran, H. Ceulemans, J. D. Boyd and A. E. Carpenter, Image-based profiling for drug discovery: due for a machine-learning upgrade?, *Nat. Rev. Drug Discov.*, 2021, **20**(2), 145.

10 M.-A. Bray, S. Singh, H. Han, C. T. Davis, B. Borgeson, C. Hartland, M. Kost-Alimova, S. M. Gustafsdottir, C. C. Gibson and A. E. Carpenter, Cell Painting, a high-content image-based assay for morphological profiling using multiplexed fluorescent dyes, *Nat. Protocols*, 2016, **11**(9), 1757.

11 X. Fang, Y. Zheng, Y. Duan, Y. Liu and W. Zhong, Recent Advances in Design of Fluorescence-Based Assays for High-Throughput Screening, *Anal. Chem.*, 2019, **91**(1), 482.

12 C. Zhang, D. Zhang and J.-X. Cheng, Coherent Raman Scattering Microscopy in Biology and Medicine, *Ann. Rev. Biomed. Eng.*, 2015, **17**(1), 415.

13 Y. Li, B. Shen, S. Li, Y. Zhao, J. Qu and L. Liu, Review of Stimulated Raman Scattering Microscopy Techniques and Applications in the Biosciences, *Adv. Biol.*, 2021, **5**(1), 2000184.

14 C. W. Freudiger, W. Min, B. G. Saar, S. Lu, G. R. Holtom, C. He, J. C. Tsai, J. X. Kang and X. S. Xie, Label-Free Biomedical Imaging with High Sensitivity by Stimulated Raman Scattering Microscopy, *Science*, 2008, **322**(5909), 1857.

15 B. G. Saar, C. W. Freudiger, J. Reichman, C. M. Stanley, G. R. Holtom and X. S. Xie, Video-Rate Molecular Imaging in Vivo with Stimulated Raman Scattering, *Science*, 2010, **330**(6009), 1368.

16 Z. Movasaghi, S. Rehman and I. U. Rehman, Raman Spectroscopy of Biological Tissues, *Appl. Spectrosc. Rev.*, 2007, **42**(5), 493.

17 K. Dodo, W. J. Tipping, H. Yamakoshi, S. Egoshi, T. Kubo, Y. Kumamoto, K. Faulds, D. Graham, K. Fujita and M. Sodeoka, Alkyne-tag Raman imaging and sensing of bioactive compounds, *Nat. Rev. Methods Primers*, 2025, **5**(1), 20.

18 F. Hu, C. Zeng, R. Long, Y. Miao, L. Wei, Q. Xu and W. Min, Supermultiplexed optical imaging and barcoding with engineered polyynes, *Nat. Methods*, 2018, **15**, 194.

19 H. Yamakoshi, K. Dodo, A. Palonpon, J. Ando, K. Fujita, S. Kawata and M. Sodeoka, Alkyne-Tag Raman Imaging for Visualization of Mobile Small Molecules in Live Cells, *J. Am. Chem. Soc.*, 2012, **134**(51), 20681.

20 N. Murphy, W. J. Tipping, H. J. Braddick, L. T. Wilson, N. C. O. Tomkinson, K. Faulds, D. Graham and P. Farràs, Expanding the Range of Bioorthogonal Tags for Multiplex Stimulated Raman Scattering Microscopy, *Angew. Chem., Int. Ed.*, 2023, **62**(48), e202311530.

21 Z. Chen, D. W. Paley, L. Wei, A. L. Weisman, R. A. Friesner, C. Nuckolls and W. Min, Multicolor Live-Cell Chemical Imaging by Isotopically Edited Alkyne Vibrational Palette, *J. Am. Chem. Soc.*, 2014, **136**(22), 8027.

22 S. Bakthavatsalam, K. Dodo and M. Sodeoka, A decade of alkyne-tag Raman imaging (ATRI): applications in biological systems, *RSC Chem. Biol.*, 2021, **2**, 1415.

23 W. R. Silva, C. T. Graefe and R. R. Frontiera, Toward Label-Free Super-Resolution Microscopy, *ACS Photonics*, 2016, **3**(1), 79.

24 Y. Bi, C. Yang, Y. Chen, S. Yan, G. Yang, Y. Wu, G. Zhang and P. Wang, Near-resonance enhanced label-free stimulated Raman scattering microscopy with spatial resolution near 130 nm, *Light: Sci. Appl.*, 2018, **7**(1), 81.

25 H. Yamakoshi, K. Dodo, M. Okada, J. Ando, A. Palonpon, K. Fujita, S. Kawata and M. Sodeoka, Imaging of EdU, an Alkyne-Tagged Cell Proliferation Probe, by Raman Microscopy, *J. Am. Chem. Soc.*, 2011, **133**(16), 6102.

26 S. Stolik, J. A. Delgado, A. Pérez and L. Anasagasti, Measurement of the penetration depths of red and near infrared light in human ''ex vivo'' tissues, *J. Photochem. Photobiol., B*, 2000, **57**(2), 90.

27 J. Li, P. Lin, Y. Tan and J. X. Cheng, Volumetric stimulated Raman scattering imaging of cleared tissues towards three-dimensional chemical histopathology, *Biomed. Opt. Express*, 2019, **10**(8), 4329.

28 D. A. Orringer, B. Pandian, Y. S. Niknafs, T. C. Hollon, J. Boyle, S. Lewis, M. Garrard, S. L. Hervey-Jumper, H. J. L. Garton and C. O. Maher, *et al.*, Rapid intraoperative histology of unprocessed surgical specimens *via* fibre-laser-based stimulated Raman scattering microscopy, *Nat. Biomed. Eng.*, 2017, **1**(2), 0027.

29 M. Wei, L. Shi, Y. Shen, Z. Zhao, A. Guzman, L. J. Kaufman, L. Wei and W. Min, Volumetric chemical imaging by clearing-enhanced stimulated Raman scattering microscopy, *Proc. Natl. Acad. Sci. U. S. A.*, 2019, **116**(14), 6608.

30 L. Wei, F. Hu, Z. Chen, Y. Shen, L. Zhang and W. Min, Live-Cell Bioorthogonal Chemical Imaging: Stimulated Raman Scattering Microscopy of Vibrational Probes, *Acc. Chem. Res.*, 2016, **49**(8), 1494.

31 Y. Wakisaka, Y. Suzuki, O. Iwata, A. Nakashima, T. Ito, M. Hirose, R. Domon, M. Sugawara, N. Tsumura and H. Watarai, *et al.*, Probing the metabolic heterogeneity of live Euglena gracilis with stimulated Raman scattering microscopy, *Nat. Microbiol.*, 2016, **1**, 16124.

32 P. Wang, B. Liu, D. Zhang, M. Y. Belew, H. A. Tissenbaum and J.-X. Cheng, Imaging Lipid Metabolism in Live Caenorhabditis elegans Using Fingerprint Vibrations, *Angew. Chem., Int. Ed.*, 2014, **53**(44), 11787.

33 Z. Yu, T. Chen, X. Zhang, D. Fu, X. Liao, J. Shen, X. Liu, B. Zhang, X. S. Xie and X.-D. Su, *et al.*, Label-free chemical imaging in vivo: three-dimensional non-invasive microscopic observation of amphioxus notochord through stimulated Raman scattering (SRS), *Chem. Sci.*, 2012, **3**(8), 2646.

34 F. Tian, W. Yang, D. A. Mordes, J.-Y. Wang, J. S. Salameh, J. Mok, J. Chew, A. Sharma, E. Leno-Duran and S. Suzuki-Uematsu, *et al.*, Monitoring peripheral nerve degeneration in ALS by label-free stimulated Raman scattering imaging, *Nat. Commun.*, 2016, **7**, 13283.

35 A. T. Francis, B. Manifold, E. C. Carlson, R. Hu, A. H. Hill, S. Men and D. Fu, In vivo simultaneous nonlinear absorption Raman and fluorescence (SNARF) imaging of mouse brain cortical structures, *Commun. Biol.*, 2022, **5**(1), 222.

36 B. Sarri, R. Canonge, X. Audier, E. Simon, J. Wojak, F. Caillol, C. Cador, D. Marguet, F. Poizat and M. Giovannini, *et al.*, Fast stimulated Raman and second harmonic generation imaging for intraoperative gastro-intestinal cancer detection, *Sci. Rep.*, 2019, **9**(1), 10052.

37 V. V. Yakovlev, H. F. Zhang, G. D. Noojin, M. L. Denton, R. J. Thomas and M. O. Scully, Stimulated Raman photoacoustic imaging, *Proc. Natl. Acad. Sci. U. S. A.*, 2010, **107**(47), 20335.

38 Y. Zhu, X. Ge, H. Ni, J. Yin, H. Lin, L. Wang, Y. Tan, C. V. Prabhu Dessai, Y. Li and X. Teng, *et al.*, Stimulated Raman photothermal microscopy toward ultrasensitive chemical imaging, *Sci. Adv.*, 2023, **9**(43), eadi2181.

39 R. S. Chadha, J. A. Guerrero, L. Wei and L. M. Sanchez, Seeing is Believing: Developing Multimodal Metabolic Insights at the Molecular Level, *ACS Cent. Sci.*, 2024, **10**(4), 758.

40 D. Fu and X. S. Xie, Reliable Cell Segmentation Based on Spectral Phasor Analysis of Hyperspectral Stimulated Raman Scattering Imaging Data, *Anal. Chem.*, 2014, **86**(9), 4115.

41 P. Swiatlowska, W. Tipping, E. Marhuenda, P. Severi, V. Fomin, Z. Yang, Q. Xiao, D. Graham, C. Shanahan and

T. Iskratsch, Hypertensive Pressure Mechanosensing Alone Triggers Lipid Droplet Accumulation and Transdifferentiation of Vascular Smooth Muscle Cells to Foam Cells, *Adv. Sci.*, 2024, **9**, 2308686.

42 W. J. Tipping, L. T. Wilson, C. An, A. A. Leventi, A. W. Wark, C. Wetherill, N. C. O. Tomkinson, K. Faulds and D. Graham, Stimulated Raman scattering microscopy with spectral phasor analysis: applications in assessing drug–cell interactions, *Chem. Sci.*, 2022, **13**(12), 3468.

43 K.-C. Huang, J. Li, C. Zhang, Y. Tan and J.-X. Cheng, Multiplex Stimulated Raman Scattering Imaging Cytometry Reveals Lipid-Rich Protrusions in Cancer Cells under Stress Condition, *iScience*, 2020, **23**(3), 100953.

44 E. W. Hislop, W. J. Tipping, K. Faulds and D. Graham, Label-Free Cytometric Evaluation of Mitosis *via* Stimulated Raman Scattering Microscopy and Spectral Phasor Analysis, *Anal. Chem.*, 2023, **95**(18), 7244.

45 W. J. Tipping, G. W. Gould, K. Faulds and D. Graham, Unmixing Hyperspectral SRS Images in the Cell-Silent Region of the Raman Spectrum Using Phasor Analysis, *Chem. Biomed. Imaging*, 2025, **3**(9), 630–635.

46 H. J. Braddick, W. J. Tipping, L. T. Wilson, H. S. Jaconelli, E. K. Grant, K. Faulds, D. Graham and N. C. O. Tomkinson, Determination of Intracellular Esterase Activity Using Ratiometric Raman Sensing and Spectral Phasor Analysis, *Anal. Chem.*, 2023, **95**(12), 5369.

47 J. Liu, M. Osadchy, L. Ashton, M. Foster, C. J. Solomon and S. J. Gibson, Deep convolutional neural networks for Raman spectrum recognition: a unified solution, *Analyst*, 2017, **142**(21), 4067.

48 C. Qian, K. Miao, L.-E. Lin, X. Chen, J. Du and L. Wei, Super-resolution label-free volumetric vibrational imaging, *Nat. Commun.*, 2021, **12**(1), 3648.

49 W. J. Tipping, K. Faulds and D. Graham, Advances in Super-resolution Stimulated Raman Scattering Microscopy, *Chem. Biomed. Imaging*, 2024, **2**(11), 733.

50 J. Shou, A. Komazawa, Y. Wachi, M. Kawatani, H. Fujioka, S. J. Spratt, T. Mizuguchi, K. Oguchi, H. Akaboshi and F. Obata, *et al.*, Super-resolution vibrational imaging based on photoswitchable Raman probe, *Sci. Adv.*, 2023, **9**(24), eade9118.

51 H. Jang, Y. Li, A. A. Fung, P. Bagheri, K. Hoang, D. Skowronska-Krawczyk, X. Chen, J. Y. Wu, B. Bintu and L. Shi, Super-resolution SRS microscopy with A-PoD, *Nat. Methods*, 2023, **20**(3), 448.

52 D. Zhang, P. Wang, M. N. Slipchenko, D. Ben-Amotz, A. M. Weiner and J.-X. Cheng, Quantitative Vibrational Imaging by Hyperspectral Stimulated Raman Scattering Microscopy and Multivariate Curve Resolution Analysis, *Anal. Chem.*, 2013, **85**(1), 98.

53 T. Bocklitz, T. Meyer, M. Schmitt, I. Rimke, F. Hoffmann, F. von Eggeling, G. Ernst, O. Guntinas-Lichius and J. Popp, Invited Article: Comparison of hyperspectral coherent Raman scattering microscopies for biomedical applications, *APL Photonics*, 2018, **3**, 9.

54 A. Rensonnet, W. J. Tipping, C. Malherbe, K. Faulds, G. Eppe and D. Graham, Spectral fingerprinting of cellular lipid droplets using stimulated Raman scattering microscopy and chemometric analysis, *Analyst*, 2024, **149**(2), 553.

55 Z. Huang, S. Yan, Y. Li, W. Ju and P. Wang, Direct Counting and Imaging Chain Lengths of Lipids by Stimulated Raman Scattering Microscopy, *Anal. Chem.*, 2023, **95**(13), 5815.

56 S. Heuke, I. Rimke, B. Sarri, P. Gasecka, R. Appay, L. Legoff, P. Volz, E. Büttner and H. Rigneault, Shot-noise limited tunable dual-vibrational frequency stimulated Raman scattering microscopy, *Biomed. Opt. Express*, 2021, **12**(12), 7780.

57 G. Batignani, C. Ferrante, G. Fumero, M. Martinati and T. Scopigno, Femtosecond stimulated Raman spectroscopy, *Nat. Rev. Methods Primers*, 2024, **4**(1), 34.

58 B. Figueroa, W. Fu, T. Nguyen, K. Shin, B. Manifold, F. Wise and D. Fu, Broadband hyperspectral stimulated Raman scattering microscopy with a parabolic fiber amplifier source, *Biomed. Opt. Express*, 2018, **9**(12), 6116.

59 B. Manifold, B. Figueroa and D. Fu, in *Stimulated Raman Scattering Microscopy*, ed. J.-X. Cheng, W. Min, Y. Ozeki, D. Polli, Elsevier, 2022, DOI: **10.1016/B978-0-323-85158-9.00035-X**.

60 D. Fu, G. Holtom, C. Freudiger, X. Zhang and X. S. Xie, Hyperspectral Imaging with Stimulated Raman Scattering by Chirped Femtosecond Lasers, *J. Phys. Chem. B*, 2012, **117**(16), 4634.

61 B. Figueroa, Y. Chen, K. Berry, A. Francis and D. Fu, Label-Free Chemical Imaging of Latent Fingerprints with Stimulated Raman Scattering Microscopy, *Anal. Chem.*, 2017, **89**(8), 4468.

62 K. Koike, N. I. Smith and K. Fujita, Spectral focusing in picosecond pulsed stimulated Raman scattering microscopy, *Biomed. Opt. Express*, 2022, **13**(2), 995.

63 J.-P. Renaud, A. Chari, C. Ciferri, W.-T. Liu, H.-W. Rémigy, H. Stark and C. Wiesmann, Cryo-EM in drug discovery: achievements, limitations and prospects, *Nat. Rev. Drug Discov.*, 2018, **17**(7), 471.

64 B. Manifold and D. Fu, Quantitative Stimulated Raman Scattering Microscopy: Promises and Pitfalls, *Ann. Rev. Anal. Chem.*, 2022, **15**(1), 269.

65 D. Tsikritsis, E. J. Legge and N. A. Belsey, Practical considerations for quantitative and reproducible measurements with stimulated Raman scattering microscopy, *Analyst*, 2022, **147**(21), 4642.

66 D. Fu, J. Zhou, W. S. Zhu, P. W. Manley, Y. K. Wang, T. Hood, A. Wylie and X. S. Xie, Imaging the intracellular distribution of tyrosine kinase inhibitors in living cells with quantitative hyperspectral stimulated Raman scattering, *Nat. Chem.*, 2014, **6**(7), 614.

67 B. S. Wong, E. L. Dunnington, R. Wu, J. I. Kim, K. Hu, T. H. Ro and D. Fu, Facilitated Transport of EGFR Inhibitors Plays an Important Role in Their Cellular Uptake, *Anal. Chem.*, 2024, **96**(4), 1547.

68 F. X. Xu, E. G. Rathbone and D. Fu, Simultaneous Dual-Band Hyperspectral Stimulated Raman Scattering

Microscopy with Femtosecond Optical Parametric Oscillators, *J. Phys. Chem. B*, 2023, **127**(10), 2187.

69 K. Sepp, M. Lee, M. T. J. Bluntzer, G. V. Helgason, A. N. Hulme and V. G. Brunton, Utilizing Stimulated Raman Scattering Microscopy To Study Intracellular Distribution of Label-Free Ponatinib in Live Cells, *J. Med. Chem.*, 2020, **63**(5), 2028.

70 W. J. Tipping, A. S. Merchant, R. Fearon, N. C. O. Tomkinson, K. Faulds and D. Graham, Temporal imaging of drug dynamics in live cells using stimulated Raman scattering microscopy and a perfusion cell culture system, *RSC Chem. Biol.*, 2022, **3**(9), 1154.

71 P.-T. Dong, C. Zong, Z. Dagher, J. Hui, J. Li, Y. Zhan, M. Zhang, M. K. Mansour and J.-X. Cheng, Polarization-sensitive stimulated Raman scattering imaging resolves amphotericin B orientation in Candida membrane, *Sci. Adv.*, 2021, **7**(2), eabd5230.

72 W. Grudzinski, J. Sagan, R. Welc, R. Luchowski and W. I. Gruszecki, Molecular organization, localization and orientation of antifungal antibiotic amphotericin B in a single lipid bilayer, *Sci. Rep.*, 2016, **6**(1), 32780.

73 T. T. Talele, Acetylene Group, Friend or Foe in Medicinal Chemistry, *J. Med. Chem.*, 2020, **63**(11), 5625.

74 T. Mizuguchi, M. Nuriya, M. Yasui, T. Iino, Y. Ozeki and T. Saiki, Sensitive detection of alkyne-terminated hydrophobic drug by surface-enhanced stimulated Raman scattering in cetyltrimethylammonium bromide-coated gold nanorod suspensions, *Appl. Phys. Express*, 2021, **14**(3), 032003.

75 R. F. Barth, J. A. Coderre, M. G. A. H. Vicente and T. E. Blue, Boron Neutron Capture Therapy of Cancer: Current Status and Future Prospects, *Clin. Cancer Res.*, 2005, **11**(11), 3987.

76 T. Asai, H. Liu, Y. Ozeki, S. Sato, T. Hayashi and H. Nakamura, Imaging of cellular uptake of boron cluster compound by stimulated Raman scattering microscopy, *Appl. Phys. Express*, 2019, **12**(11), 112004.

77 R. Oda, J. Shou, W. Zhong, Y. Ozeki, M. Yasui and M. Nuriya, Direct visualization of general anesthetic propofol on neurons by stimulated Raman scattering microscopy, *iSci.*, 2022, **25**(3), 103936.

78 W. J. Tipping, M. Lee, A. Serrels, V. G. Brunton and A. N. Hulme, Imaging drug uptake by bioorthogonal stimulated Raman scattering microscopy, *Chem. Sci.*, 2017, **8**(8), 5606.

79 M. M. Gaschler, F. Hu, H. Feng, A. Linkermann, W. Min and B. R. Stockwell, Determination of the Subcellular Localization and Mechanism of Action of Ferrostatins in Suppressing Ferroptosis, *ACS Chem. Biol.*, 2018, **13**(4), 1013.

80 J. Seidel, Y. Miao, W. Porterfield, W. Cai, X. Zhu, S.-J. Kim, F. Hu, S. Bhattarai-Kline, W. Min and W. Zhang, Structure–activity–distribution relationship study of anti-cancer antimycin-type depsipeptides, *Chem. Commun.*, 2019, **55**(63), 9379.

81 C. Tentellino, W. J. Tipping, L. M. C. McGee, L. M. Bain, C. Wetherill, S. Laing, I. Tyson-Hirst, C. J. Suckling, R. Beveridge and F. J. Scott, *et al.*, Ratiometric imaging of minor groove binders in mammalian cells using Raman microscopy, *RSC Chem. Biol.*, 2022, **3**(12), 1403.

82 M. Kawaguchi, Y. Yonetani, T. Mizuguchi, S. J. Spratt, M. Asanuma, H. Shimizu, M. Sasaki and Y. Ozeki, Visualization of Modified Bisarylbutadiyne-Tagged Small Molecules in Live-Cell Nuclei by Stimulated Raman Scattering Microscopy, *Anal. Chem.*, 2024, **96**(17), 6643.

83 D. C. Morgan, L. McDougall, A. Knuhtsen and A. G. Jamieson, Development of Bifunctional, Raman Active Diyne-Girder Stapled α-Helical Peptides, *Chem. – Eur. J.*, 2023, **29**(41), e202300855.

84 D. C. Morgan, L. McDougall, A. Knuhtsen, L. Buetow, C. F. Steven, O. A. Shepperson, D. T. Huang, A. N. Hulme and A. G. Jamieson, Raman active diyne-girder conformationally constrained p53 stapled peptides bind to MDM2 for visualisation without fluorophores, *RSC Chem. Biol.*, 2025, **6**(3), 394.

85 M. P. Ravindra, M. Lee, S. Dimova, C. F. Steven, M. T. J. Bluntzer, V. G. Brunton and A. N. Hulme, Stretching the Bisalkyne Raman Spectral Palette Reveals a New Electrophilic Covalent Motif, *Chem. – Eur. J.*, 2023, **29**(38), e202300953.

86 C. F. Steven, M. Lee, G. S. Nichol, P. R. J. Davey, E. Chiarparin, V. G. Brunton and A. N. Hulme, Design, Synthesis, and Analytical Evaluation of Fsp3-Inspired Raman Probes for Cellular Imaging, *Eur. J. Org. Chem.*, 2022, (30), e202200393.

87 L. E. Jamieson and H. J. Byrne, Vibrational spectroscopy as a tool for studying drug-cell interaction: Could high throughput vibrational spectroscopic screening improve drug development?, *Vib. Spectrosc.*, 2017, **91**, 16–30.

88 R. J. DeBerardinis and C. B. Thompson, Cellular Metabolism and Disease: What Do Metabolic Outliers Teach Us?, *Cell*, 2012, **148**(6), 1132.

89 A. Schulze and A. L. Harris, How cancer metabolism is tuned for proliferation and vulnerable to disruption, *Nature*, 2012, **491**(7424), 364.

90 T. Laval and M. Ouimet, A role for lipophagy in atherosclerosis, *Nat. Rev. Cardiol.*, 2023, **20**(7), 431.

91 D. M. Wilson, M. R. Cookson, L. Van Den Bosch, H. Zetterberg, D. M. Holtzman and I. Dewachter, Hallmarks of neurodegenerative diseases, *Cell*, 2023, **186**(4), 693.

92 A. Ali, S. Davidson, E. Fraenkel, I. Gilmore, T. Hankemeier, J. A. Kirwan, A. N. Lane, I. Lanekoff, M. Larion and L. I. McCall, *et al.*, Single cell metabolism: current and future trends, *Metabolomics*, 2022, **18**(10), 77.

93 S. Benson, F. de Moliner, W. Tipping and M. Vendrell, Miniaturized Chemical Tags for Optical Imaging, *Angew. Chem., Int. Ed.*, 2022, **61**(34), e202204788.

94 M. T. Snaebjornsson, S. Janaki-Raman and A. Schulze, Greasing the Wheels of the Cancer Machine: The Role of Lipid Metabolism in Cancer, *Cell Metab*, 2020, **31**(1), 62.

95 S. Yue, J. Li, S. Y. Lee, H. J. Lee, T. Shao, B. Song, L. Cheng, T. A. Masterson, X. Liu, T. L. Ratliff and J. X. Cheng, Cholesteryl Ester Accumulation Induced by PTEN Loss

and PI3K/AKT Activation Underlies Human Prostate Cancer Aggressiveness, *Cell Metab*, 2014, **19**(3), 393.

96 H. J. Lee, J. Li, R. E. Vickman, J. Li, R. Liu, A. C. Durkes, B. D. Elzey, S. Yue, X. Liu and T. L. Ratliff, *et al.*, Cholesterol Esterification Inhibition Suppresses Prostate Cancer Metastasis by Impairing the Wnt/β-catenin Pathway, *Mol. Cancer Res*, 2018, **16**(6), 974.

97 J. Li, D. Gu, S. S. Y. Lee, B. Song, S. Bandyopadhyay, S. Chen, S. F. Konieczny, T. L. Ratliff, X. Liu and J. Xie, *et al.*, Abrogating cholesterol esterification suppresses growth and metastasis of pancreatic cancer, *Oncogene*, 2016, **35**(50), 6378.

98 J. Li, X. Qu, J. Tian, J.-T. Zhang and J.-X. Cheng, Cholesterol esterification inhibition and gemcitabine synergistically suppress pancreatic ductal adenocarcinoma proliferation, *PLOS ONE*, 2018, **13**(2), e0193318.

99 S. Bandyopadhyay, J. Li, E. Traer, J. W. Tyner, A. Zhou, S. T. Oh and J.-X. Cheng, Cholesterol esterification inhibition and imatinib treatment synergistically inhibit growth of BCR-ABL mutation-independent resistant chronic myelogenous leukemia, *PLOS ONE*, 2017, **12**(7), e0179558.

100 S. Zhang, T. Fang, Y. He, W. Feng, Z. Yu, Y. Zheng, C. Zhang, S. Hu, Z. Liu and J. Liu, *et al.*, VHL mutation drives human clear cell renal cell carcinoma progression through PI3K/AKT-dependent cholesteryl ester accumulation, *eBioMedicine*, 2024, **103**, 105070.

101 S. S.-Y. Lee, J. Li, J. N. Tai, T. L. Ratliff, K. Park and J.-X. Cheng, Avasimibe Encapsulated in Human Serum Albumin Blocks Cholesterol Esterification for Selective Cancer Treatment, *ACS Nano*, 2015, **9**(3), 2420.

102 J. Li, S. Condello, J. Thomes-Pepin, X. Ma, Y. Xia, T. D. Hurley, D. Matei and J.-X. Cheng, Lipid Desaturation Is a Metabolic Marker and Therapeutic Target of Ovarian Cancer Stem Cells, *Cell Stem Cell*, 2017, **20**(3), 303.

103 N. Wang, J. Wang, P. Wang, N. Ji and S. Yue, Label-Free Raman Spectromicroscopy Unravels the Relationship between MGMT Methylation and Intracellular Lipid Accumulation in Glioblastoma, *Anal. Chem.*, 2023, **95**(31), 11567.

104 W. J. Tipping, L. T. Wilson, N. C. O. Tomkinson, K. Faulds and D. Graham, Label-Free Screening of Drug-Induced Liver Injury Using Stimulated Raman Scattering Microscopy and Spectral Phasor Analysis, *Anal. Chem.*, 2024, **96**(26), 10639.

105 Y. Urasaki, C. Zhang, J. X. Cheng and T. T. Le, Quantitative Assessment of Liver Steatosis and Affected Pathways with Molecular Imaging and Proteomic Profiling, *Sci. Rep.*, 2018, **8**(1), 3606.

106 H. Jia, J. Liu, T. Fang, Z. Zhou, R. Li, W. Yin, Y. Qian, Q. Wang, W. Zhou and C. Liu, *et al.*, The role of altered lipid composition and distribution in liver fibrosis revealed by multimodal nonlinear optical microscopy, *Sci. Adv.*, 2023, **9**(2), eabq2937.

107 M. Zhuge, K.-C. Huang, H. J. Lee, Y. Jiang, Y. Tan, H. Lin, P.-T. Dong, G. Zhao, D. Matei and Q. Yang, *et al.*, Ultrasensitive Vibrational Imaging of Retinoids by Visible Preresonance Stimulated Raman Scattering Microscopy, *Adv. Sci.*, 2021, **8**(9), 2003136.

108 L. Wei and W. Min, Electronic Preresonance Stimulated Raman Scattering Microscopy, *J. Phys. Chem. Lett.*, 2018, **9**(15), 4294.

109 S. Yan, S. Cui, K. Ke, B. Zhao, X. Liu, S. Yue and P. Wang, Hyperspectral Stimulated Raman Scattering Microscopy Unravels Aberrant Accumulation of Saturated Fat in Human Liver Cancer, *Anal. Chem.*, 2018, **90**(11), 6362.

110 Y. Yuan, N. Shah, M. I. Almohaisin, S. Saha and F. Lu, Assessing fatty acid-induced lipotoxicity and its therapeutic potential in glioblastoma using stimulated Raman microscopy, *Sci. Rep.*, 2021, **11**(1), 7422.

111 C. H. Allen, R. Skillings, D. Ahmed, S. C. Sanchez, K. Altwasser, G. Hilan, W. Willmore, V. Chauhan, E. Cassol and S. Murugkar, Investigating ionizing radiation-induced changes in breast cancer cells using stimulated Raman scattering microscopy, *J. Biomed. Opt.*, 2023, **28**(7), 076501.

112 Y. Tan, J. Li, G. Zhao, K.-C. Huang, H. Cardenas, Y. Wang, D. Matei and J.-X. Cheng, Metabolic reprogramming from glycolysis to fatty acid uptake and beta-oxidation in platinum-resistant cancer cells, *Nat. Commun.*, 2022, **13**(1), 4554.

113 J. Du, Y. Su, C. Qian, D. Yuan, K. Miao, D. Lee, A. H. C. Ng, R. S. Wijker, A. Ribas and R. D. Levine, *et al.*, Raman-guided subcellular pharmaco-metabolomics for metastatic melanoma cells, *Nat. Commun.*, 2020, **11**(1), 4830.

114 X. G. Zhu, S. Nicholson Puthenveedu, Y. Shen, K. La, C. Ozlu, T. Wang, D. Klompstra, Y. Gultekin, J. Chi and J. Fidelin, *et al.*, CHP1 Regulates Compartmentalized Glycerolipid Synthesis by Activating GPAT4, *Mol. Cell*, 2019, **74**(1), 45.

115 L. Wei, Y. Yu, Y. Shen, M. C. Wang and W. Min, Vibrational imaging of newly synthesized proteins in live cells by stimulated Raman scattering microscopy, *Proc. Natl. Acad. Sci.*, 2013, **110**(28), 11226.

116 L. Wei, Y. Shen, F. Xu, F. Hu, J. K. Harrington, K. L. Targoff and W. Min, Imaging Complex Protein Metabolism in Live Organisms by Stimulated Raman Scattering Microscopy with Isotope Labeling, *ACS Chem. Biol.*, 2015, **10**(3), 901.

117 F. X. Xu, R. Sun, R. Owens, K. Hu and D. Fu, Assessing Drug Uptake and Response Differences in 2D and 3D Cellular Environments Using Stimulated Raman Scattering Microscopy, *Anal. Chem.*, 2024, **96**(36), 14480.

118 F. X. Xu, R. Wu, K. Hu and D. Fu, Measuring Drug Response with Single-Cell Growth Rate Quantification, *Anal. Chem.*, 2023, **95**(49), 18114.

119 Y. Shen, F. Xu, L. Wei, F. Hu and W. Min, Live-Cell Quantitative Imaging of Proteome Degradation by Stimulated Raman Scattering, *Angew. Chem., Int. Ed.*, 2014, **53**(22), 5596.

120 Z. Liu, J. Liu, T. Zhang, L. Li, S. Zhang, H. Jia, Y. Xia, M. Shi, J. Zhang and S. Yue, *et al.*, Distinct BTK inhibitors differentially induce apoptosis but similarly suppress chemotaxis and lipid accumulation in mantle cell lymphoma, *BMC Cancer*, 2021, **21**(1), 732.

121 A. van Belkum, C.-A. D. Burnham, J. W. A. Rossen, F. Mallard, O. Rochas and W. M. Dunne, Innovative and rapid antimicrobial susceptibility testing systems, *Nat. Rev. Microbiol.*, 2020, **18**(5), 299.

122 A. van Belkum, T. T. Bachmann, G. Lüdke, J. G. Lisby, G. Kahlmeter, A. Mohess, K. Becker, J. P. Hays, N. Woodford and K. Mitsakakis, *et al.*, Developmental roadmap for antimicrobial susceptibility testing systems, *Nat. Rev. Microbiol.*, 2019, **17**(1), 51.

123 M. M. Jansson, M. Kögler, S. Hörkkö, T. Ala-Kokko and L. Rieppo, Vibrational spectroscopy and its future applications in microbiology, *Appl. Spectrosc. Rev.*, 2023, **58**(2), 132.

124 W. Hong, C. W. Karanja, N. S. Abutaleb, W. Younis, X. Zhang, M. N. Seleem and J.-X. Cheng, Antibiotic Susceptibility Determination within One Cell Cycle at Single-Bacterium Level by Stimulated Raman Metabolic Imaging, *Anal. Chem.*, 2018, **90**(6), 3737.

125 B. Görke and J. Stülke, Carbon catabolite repression in bacteria: many ways to make the most out of nutrients, *Nat. Rev. Microbiol.*, 2008, **6**(8), 613.

126 M. Zhang, W. Hong, N. S. Abutaleb, J. Li, P.-T. Dong, C. Zong, P. Wang, M. N. Seleem and J.-X. Cheng, Rapid Determination of Antimicrobial Susceptibility by Stimulated Raman Scattering Imaging of D2O Metabolic Incorporation in a Single Bacterium, *Adv. Sci.*, 2020, **7**(19), 2001452.

127 L. Shi, C. Zheng, Y. Shen, Z. Chen, E. S. Silveira, L. Zhang, M. Wei, C. Liu, C. de Sena-Tomas and K. Targoff, *et al.*, Optical imaging of metabolic dynamics in animals, *Nat. Commun.*, 2018, **9**(1), 2995.

128 M. Zhang, M. N. Seleem and J.-X. Cheng, Rapid Antimicrobial Susceptibility Testing by Stimulated Raman Scattering Imaging of Deuterium Incorporation in a Single Bacterium, *J. Vis. Exp.*, 2022, e62398.

129 B. Sun, X. Kang, S. Yue, L. Lan, R. Li, C. Chen, W. Zhang, S. He, C. Zhang and Y. Fan, *et al.*, A rapid procedure for bacterial identification and antimicrobial susceptibility testing directly from positive blood cultures, *Analyst*, 2022, **147**(1), 147.

130 W. Zhang, Y. Li, L. Yao, F. Wu, C. Chen, L. Zhou, B. Zheng, P. Wang and W. Hong, Rapid antimicrobial susceptibility testing by stimulated Raman scattering metabolic imaging and morphological deformation of bacteria, *Anal. Chim. Acta*, 2021, **1168**, 338622.

131 B. Sun, Z. Wang, J. Lin, C. Chen, G. Zheng, S. Yue, H. Wang, X. Kang, X. Chen and W. Hong, *et al.*, Automatic quantitative analysis of metabolism inactivation concentration in single bacterium using stimulated Raman scattering microscopy with deep learning image segmentation, *Med. Nov. Technol. Devices*, 2022, **14**, 100114.

132 S. W. G. van Hoogstraten, C. Kuik, J. J. C. Arts and B. Cillero-Pastor, Molecular imaging of bacterial biofilms-a systematic review, *Crit. Rev. Microbiol.*, 2024, **50**(6), 971.

133 K. T. Schiessl, F. Hu, J. Jo, S. Z. Nazia, B. Wang, A. Price-Whelan, W. Min and L. E. P. Dietrich, Phenazine production promotes antibiotic tolerance and metabolic heterogeneity in Pseudomonas aeruginosa biofilms, *Nat. Commun.*, 2019, **10**(1), 762.

134 K. Bae, W. Zheng, Y. Ma and Z. Huang, Real-Time Monitoring of Pharmacokinetics of Antibiotics in Biofilms with Raman-Tagged Hyperspectral Stimulated Raman Scattering Microscopy, *Theranostics*, 2019, **9**(5), 1348.

135 M. C. Fisher, A. Alastruey-Izquierdo, J. Berman, T. Bicanic, E. M. Bignell, P. Bowyer, M. Bromley, R. Brüggemann, G. Garber and O. A. Cornely, *et al.*, Tackling the emerging threat of antifungal resistance to human health, *Nat. Rev. Microbiol.*, 2022, **20**(9), 557.

136 E. L. Berkow, S. R. Lockhart and L. Ostrosky-Zeichner, Antifungal Susceptibility Testing: Current Approaches, *Clin. Microbol. Rev.*, 2020, **33**(3), e00069.

137 C. W. Karanja, W. Hong, W. Younis, H. E. Eldesouky, M. N. Seleem and J.-X. Cheng, Stimulated Raman Imaging Reveals Aberrant Lipogenesis as a Metabolic Marker for Azole-Resistant Candida albicans, *Anal. Chem.*, 2017, **89**(18), 9822.

138 J. Li and J.-X. Cheng, Direct Visualization of De novo Lipogenesis in Single Living Cells, *Sci. Rep.*, 2014, **4**, 6807.

139 C. Chen, Y. Wang, F. Wu and W. Hong, Rapid Antifungal Susceptibility Testing Based on Single-Cell Metabolism Analysis Using Stimulated Raman Scattering Imaging, *Anal. Chem.*, 2023, **95**(42), 15556.

140 M. Zhang, P.-T. Dong, H. E. Eldesouky, Y. Zhan, H. Lin, Z. Wang, E. A. Salama, S. Jusuf, C. Zong and Z. Chen, *et al.*, Fingerprint Stimulated Raman Scattering Imaging Unveils Ergosteryl Ester as a Metabolic Signature of Azole-Resistant Candida albicans, *Anal. Chem.*, 2023, **95**(26), 9901.

141 Y. Zhang, Y. Zhou, W. Fang, H. Zhu, C. Ye, D. Zhang and H. J. Lee, Spatial sterol metabolism unveiled by stimulated Raman imaging, *Front. Chem.*, 2023, **11**, 1166313.

142 H. Lin, C.-S. Liao, P. Wang, N. Kong and J.-X. Cheng, Spectroscopic stimulated Raman scattering imaging of highly dynamic specimens through matrix completion, *Light Sci. Appl.*, 2018, **7**(5), 17179.

143 C. Lima, C. W. Theron, H. Muhamadali, D. B. Kell and R. Goodacre, Spectral artefacts induced by moving targets in live hyperspectral stimulated Raman spectroscopy: The case of lipid droplets in yeast cells, *Clin. Spectrosc.*, 2021, **3**, 100014.

144 H. Ni, P. Lin, Y. Zhu, M. Zhang, Y. Tan, Y. Zhan, Z. Wang and J.-X. Cheng, Multiwindow SRS Imaging Using a Rapid Widely Tunable Fiber Laser, *Anal. Chem.*, 2021, **93**(47), 15703.

145 A. J. Hughes, S. S. Tawfik, K. P. Baruah, E. A. O'Toole and R. F. L. O'Shaughnessy, Tape strips in dermatology research, *Br. J. Dermatol.*, 2021, **185**(1), 26.

146 C.-S. Liao, P. Wang, P. Wang, J. Li, H. J. Lee, G. Eakins and J.-X. Cheng, Spectrometer-free vibrational imaging by retrieving stimulated Raman signal from highly scattered photons, *Sci. Adv.*, 2015, **1**, 9.

147 B. G. Saar, L. R. Contreras-Rojas, X. S. Xie and R. H. Guy, Imaging Drug Delivery to Skin with Stimulated Raman Scattering Microscopy, *Mol. Pharm.*, 2011, **8**(3), 969.

148 N. Garrett, B. Singh, A. Jones and J. Moger, Imaging microscopic distribution of antifungal agents in dandruff treatments with stimulated Raman scattering microscopy, *J. Biomed. Opt.*, 2017, **22**(6), 066003.

149 A. Feizpour, T. Marstrand, L. Bastholm, S. Eirefelt and C. L. Evans, Label-Free Quantification of Pharmacokinetics in Skin with Stimulated Raman Scattering Microscopy and Deep Learning, *J. Invest. Dermatol.*, 2021, **141**(2), 395.

150 N. A. Belsey, N. L. Garrett, L. R. Contreras-Rojas, A. J. Pickup-Gerlaugh, G. J. Price, J. Moger and R. H. Guy, Evaluation of drug delivery to intact and porated skin by coherent Raman scattering and fluorescence microscopies, *J. Controlled Release*, 2014, **174**(0), 37.

151 L. Wei, F. Hu, Y. Shen, Z. Chen, Y. Yu, C.-C. Lin, M. C. Wang and W. Min, Live-cell imaging of alkyne-tagged small biomolecules by stimulated Raman scattering, *Nat. Methods*, 2014, **11**(4), 410.

152 W. S. Chiu, N. A. Belsey, N. L. Garrett, J. Moger, G. J. Price, M. B. Delgado-Charro and R. H. Guy, Drug delivery into microneedle-porated nails from nanoparticle reservoirs, *J. Controlled Release*, 2015, **220**, 98.

153 F.-K. Lu, S. Basu, V. Igras, M. P. Hoang, M. Ji, D. Fu, G. R. Holtom, V. A. Néel, C. W. Freudiger and D. E. Fisher, *et al.*, Label-free DNA imaging in vivo with stimulated Raman scattering microscopy, *Proc. Natl. Acad. Sci. U. S. A.*, 2015, **112**(37), 11624.

154 T. Ito, R. Iguchi, F. Matsuoka, Y. Nishi, T. Ogihara and K. Misawa, Label-free skin penetration analysis using time-resolved, phase-modulated stimulated Raman scattering microscopy, *Biomed. Opt. Express*, 2021, **12**(10), 6545.

155 I. J. Pence, B. A. Kuzma, M. Brinkmann, T. Hellwig and C. L. Evans, Multi-window sparse spectral sampling stimulated Raman scattering microscopy, *Biomed. Opt. Express*, 2021, **12**(10), 6095.

156 B. A. Kuzma, D. Tu, A. Goss, F. Iliopoulos, J. B. Slade, A. Wiatrowski, A. Feizpour and C. L. Evans, Instantaneous topical drug quantification using a 3D printed microfluidic device and coherent Raman imaging, *OpenNano*, 2023, **12**, 100151.

157 S. Iwanaga, M. Egawa, K. Tokunaga, J. Hosoi and Y. Ozeki, Non-staining imaging of keratinocyte differentiation with stimulated Raman scattering microscopy, *J. Dermatol. Sci.*, 2016, **84**(1), e134.

158 M. Egawa, K. Tokunaga, J. Hosoi, S. Iwanaga and Y. Ozeki, In situ visualization of intracellular morphology of epidermal cells using stimulated Raman scattering microscopy, *J. Biomed. Opt.*, 2016, **21**(8), 086017.

159 S. Osseiran, J. D. Cruz, S. Jeong, H. Wang, C. Fthenakis and C. L. Evans, Characterizing stratum corneum structure, barrier function, and chemical content of human skin with coherent Raman scattering imaging, *Biomed. Opt. Express*, 2018, **9**(12), 6425.

160 M. Egawa, S. Iwanaga, J. Hosoi, M. Goto, H. Yamanishi, M. Miyai, C. Katagiri, K. Tokunaga, T. Asai and Y. Ozeki, Label-free stimulated Raman scattering microscopy visualizes changes in intracellular morphology during human epidermal keratinocyte differentiation, *Sci. Rep.*, 2019, **9**(1), 12601.

161 M. Goto, M. Egawa, T. Asai and Y. Ozeki, Imaging-based evaluation of lipids in the stratum corneum by label-free stimulated Raman scattering microscopy, *Skin Res. Technol.*, 2023, **29**(6), e13355.

162 T. Mizuguchi, C. T. Knight, M. Asanuma, M. Goto, M. Ninomiya, S. Takahashi, H. Akaboshi, M. Egawa and Y. Ozeki, Three-Dimensional Analysis of Water Dynamics in Human Skin by Stimulated Raman Scattering, *J. Phys. Chem. B*, 2023, **127**(22), 4952.

163 C.-S. Liao, M. N. Slipchenko, P. Wang, J. Li, S.-Y. Lee, R. A. Oglesbee and J.-X. Cheng, Microsecond scale vibrational spectroscopic imaging by multiplex stimulated Raman scattering microscopy, *Light Sci. Appl.*, 2015, **4**, e265.

164 W. S. Chiu, N. A. Belsey, N. L. Garrett, J. Moger, M. B. Delgado-Charro and R. H. Guy, Molecular diffusion in the human nail measured by stimulated Raman scattering microscopy, *Proc. Natl. Acad. Sci. U. S. A.*, 2015, **112**(25), 7725.

165 P. Lin, H. Ni, H. Li, N. A. Vickers, Y. Tan, R. Gong, T. Bifano and J.-X. Cheng, Volumetric chemical imaging in vivo by a remote-focusing stimulated Raman scattering microscope, *Opt. Express*, 2020, **28**(20), 30210.

166 H. Cui, A. Glidle and J. M. Cooper, Tracking Molecular Diffusion across Biomaterials' Interfaces Using Stimulated Raman Scattering, *ACS Appl. Mater. Int.*, 2022, **14**(28), 31586.

167 M. Boiret, D. N. Rutledge, N. Gorretta, Y.-M. Ginot and J.-M. Roger, Application of independent component analysis on Raman images of a pharmaceutical drug product: Pure spectra determination and spatial distribution of constituents, *J. Pharm. Biomed. Anal.*, 2014, **90**, 78.

168 H. Eksi-Kocak, S. Ilbasmis Tamer, S. Yilmaz, M. Eryilmaz, I. H. Boyaci and U. Tamer, Quantification and spatial distribution of salicylic acid in film tablets using FT-Raman mapping with multivariate curve resolution, *Asian J. Pharm. Sci.*, 2018, **13**(2), 155.

169 H. Nie, Z. Liu, B. C. Marks, L. S. Taylor, S. R. Byrn and P. J. Marsac, Analytical approaches to investigate salt disproportionation in tablet matrices by Raman spectroscopy and Raman mapping, *J. Pharm. Biomed. Anal.*, 2016, **118**, 328.

170 M. N. Slipchenko, H. Chen, D. R. Ely, Y. Jung, M. T. Carvajal and J.-X. Cheng, Vibrational imaging of tablets by epi-detected stimulated Raman scattering microscopy, *Analyst*, 2010, **135**(10), 2613.

171 B. Sarri, R. Canonge, X. Audier, V. Lavastre, G. Pénarier, J. Alie and H. Rigneault, Discriminating polymorph distributions in pharmaceutical tablets using stimulated Raman scattering microscopy, *J. Raman Spectrosc.*, 2019, **50**(12), 1896.

172 A. T. Francis, T. T. Nguyen, M. S. Lamm, R. Teller, S. P. Förster, W. Xu, T. Rhodes, R. L. Smith, J. Kuiper and Y. Su, *et al.*, In Situ Stimulated Raman Scattering (SRS) Microscopy Study of the Dissolution of Sustained-Release Implant Formulation, *Mol. Pharm.*, 2018, **15**(12), 5793.

173 B. Figueroa, T. Nguyen, S. Sotthivirat, W. Xu, T. Rhodes, M. S. Lamm, R. L. Smith, C. T. John, Y. Su and D. Fu, Detecting and Quantifying Microscale Chemical Reactions in Pharmaceutical Tablets by Stimulated Raman Scattering Microscopy, *Anal. Chem.*, 2019, **91**(10), 6894.

174 Y. Wei, I. J. Pence, A. Wiatrowski, J. B. Slade and C. L. Evans, Quantitative analysis of drug tablet aging by fast hyper-spectral stimulated Raman scattering microscopy, *Analyst*, 2024, **149**(5), 1436.

175 G. A. Stephenson, A. Aburub and T. A. Woods, Physical Stability of Salts of Weak Bases in the Solid-State, *J. Pharm. Sci.*, 2011, **100**(5), 1607.

176 B. G. Saar, R. S. Johnston, C. W. Freudiger, X. S. Xie and E. J. Seibel, Coherent Raman scanning fiber endoscopy, *Opt. Lett.*, 2011, **36**(13), 2396.

177 I. J. Pence and C. L. Evans, Translational biophotonics with Raman imaging: clinical applications and beyond, *Analyst*, 2021, **146**(21), 6379.

178 L. Wei, Z. Chen, L. Shi, R. Long, A. V. Anzalone, L. Zhang, F. Hu, R. Yuste, V. W. Cornish and W. Min, Super-multiplex vibrational imaging, *Nature*, 2017, **544**, 465.

179 Y. Miao, N. Qian, L. Shi, F. Hu and W. Min, 9-Cyanopyronin probe palette for super-multiplexed vibrational imaging, *Nat. Commun.*, 2021, **12**(1), 4518.

180 Y. Jiang, E. El Khoury, A. T. Pezacki, N. Qian, M. Oi, L. Torrente, S. G. Miller, M. Ralle, G. M. DeNicola and W. Min, *et al.*, An Activity-Based Sensing Approach to Multiplex Mapping of Labile Copper Pools by Stimulated Raman Scattering, *J. Am. Chem. Soc.*, 2024, **146**(49), 33324.